This is to certify that the

dissertation entitled

Zwitterionic Excited States of the Delta-Manifold of Quadruply Bonded Metal Dimers

presented by

Daniel Scott Engebretson

has been accepted towards fulfillment
of the requirements for

PhD degree in Chemistry

David Cleveland, George Leroi
Major professor

Date 16 May 1990

ZWITTERIONIC EXCITED STATES OF THE DELTA-MANIFOLD OF QUADRUPLY BONDED METAL DIMERS

By

Daniel Scott Engebretson

A Dissertation

Submitted to
Michigan State University
in partial fulfillment of the requirements
for the degree of

DOCTOR OF PHILOSOPHY

Department of Chemistry

1998

ABSTRACT

ZWITTERIONIC EXCITED STATES OF THE DELTA-MANIFOLD OF QUADRUPLY BONDED METAL DIMERS

By

Daniel Scott Engebretson

Photoinitiated multielectron chemistry is one of the fundamental processes of life; without it, carbon dioxide could not be converted to simple sugars and water could not be split to provide oxygen. While photoinitiated multielectron chemistry is ubiquitous in natural systems, it is rarely observed in man-made systems. Zwitterionic excited states, by virtue of having a pair of electrons associated with one nucleus, are a promising intermediate to photoinitiated multielectron chemistry.

Two electrons in two weakly coupled orbitals give rise to two states (diradical) with electrons residing in separate orbitals and two states (zwitterionic) with both electrons paired in one orbital or the other. This two-center, two-electron state manifold has eluded experimental confirmation because the zwitterionic states have been difficult to locate. Two-photon excitation of fluorescence of quadruply bonded metal dimers has been utilized to reveal the zwitterionic nature of the singlet excited states of the δ-manifold of quadruply bonded metal dimers. The assignment of the band observed in the two-photon fluorescence excitation spectra to the hidden zwitterionic state (2^1A_{1g}) has been aided by measuring the quadratic dependence of the fluorescence on the incident laser intensity and measuring the relative intensity when two circularly polarized photons are used as compared to two linearly polarized photons.

Based on these two-photon fluorescence excitation measurements for a number of different quadruply bonded dimers it has been possible to assess the zwitterionic character of the excited states. It is observed that when the δ-bond is fully formed in the $M_2X_4L_4$ series of compounds, the excited states are approximately 80% ionic. However, when the δ-bond is partially broken in the $Mo_2Cl_4(\overset{\frown}{P\,P})_2$ series of compounds, the ionic character approaches 85%. Furthermore, with this latter series of compounds, the entire manifold of states can be spectroscopically measured. This is the first case where all of the electronic states of a two-center, two-electron bond have been observed.

Dedicated to my family, past, present, and future

ACKNOWLEDGMENTS

The work reported here would not have been possible without the excellent facilities provided at Michigan State University. In particular I would like to thank the faculty of the LASER laboratory for providing such a wonderfully equipped facility in which to play. Also, I would like to thank Dr. Tom Carter, the manager of the LASER laboratory, for his help over the years.

I have had the opportunity to work with a number of great people during my graduate career; all have helped me grow both scientifically and personally. The members of the Leroi and Nocera groups could always be counted on to discuss problems and thoughts on my project – usually while drinking a beer or catching a fish (actually, not too many were ever caught). While everyone I worked with was greatly appreciated, I would like to single out Jeff Zaleski. He was my mentor when I first began and he taught me a great deal about how to approach and deal with problems in experimental physical chemistry.

I would also like to thank the support staff in the Chemistry Department. Without Manfred, Scott and Keki in the glass shop my fingers would eternally blistered since I always forget hot glass looks just like cold glass. Russ, Dick and Sam were always willing to build strange little doo-hickeys to hold sample cells, optics, and contain my experiments. I would also like to thank Ron and Scott in the electronic shop for doing their best at keeping me from getting electrocuted when I did not have everything properly grounded.

My advisors, Dan and George, will always be fondly remembered. I cannot thank them enough for the guidance they have given me. Dan could always be counted on to share his zeal for science. Usually that went hand in hand with late nights trying to get data or figures for a talk – tomorrow, but he showed me how much fun science can be. George was a great stabilizing force. His love for science and discovery was more muted

than Dan's (isn't everyone's?), but his passion was clear. I would also like to thank George for his willingness to accept me into the graduate program here at Michigan State, and also helping me leave.

Amy, Ariel and my son (we'll name him when he gets here) have to be thanked for their unending love and emotional support. Without Amy, I probably would not have gone to graduate school and despite a few bad days I have really enjoyed the decision. She was also very understanding when I would call and say "I'm working with Nocera..". I would also like to thank my parents and Amy's parents. Though I don't think they really understand what a zwitterionic excited state is they always provided a great deal of encouragement. I would also like to thank Lowell McCann. While he was not part of the chemistry department, the friendship we developed over the years will never be forgotten.

TABLE OF CONTENTS

LIST OF TABLES ix
LIST OF FIGURES x
Chapter I 1
Introduction 1
I.A Zwitterionic Excited States 5
I.A.1. History of the Delta Bond 16
1.A.2. Electronic States of the δ-Manifold 17
I.B. Nonlinear Spectroscopy 19
I.B.1 Phenomenological Aspects of Spectroscopy 19
1.B.2. Mathematical Aspects of Spectroscopy 23
I.B.2.a. Selection Rules 28
I.B.2.b. Power Dependence 31
I.B.2.c. Polarization Dependence 32
Chapter II 37
Experimental Methods 37
II.A. Materials and Standard Instrumentation 38
II.A.1. Synthesis of $Mo_2Cl_4(\overset{\frown}{P\,P})_2$ compounds 39
II.A.1.a. Synthesis of Mo_2Cl_4(S,S-dppb)$_2$ 39
II.A.1.b. Synthesis of Mo_2Cl_4(depe)$_2$ 40
II.A.1.c. Synthesis of Mo_2Cl_4(dppe)$_2$ 40
II.A.2. Spectroscopic Solvents and Materials 41
II.A.3. Standard Instrumentation. 42
II.B. Two-Photon Fluorescence Excitation (TPE) 42
II.B.1. TPE Instrumentation 42
II.B.1.a. TPE Measurment 51
II.B.1.b. Power Dependence Measurement 53
II.B.2.c. Polarization Dependence Measurement 53
Chapter III 55
Two-Photon Spectroscopy of $Mo_2Cl_4(\overset{\frown}{P\,P})_2$ Complexes 55
III.A. Experimental Background of $M_2X_4(\overset{\frown}{P\,P})_2$ 55
III.B. Two-Photon Spectroscopic Results for $Mo_2Cl_4(\overset{\frown}{P\,P})_2$ Compounds. 58
III.B.1. Mo_2Cl_4(S,S,-dppb)$_2$ 61
III.B.2. Mo_2Cl_4(depe)$_2$ 67
III.B.3. Mo_2Cl_4(dppe)$_2$. 70
III.B.4. Mo_2Cl_4(dmpm)$_2$. 70
III.C. Discussion 74
Chapter IV 77
Two-Photon Spectroscopy of $M_2X_4L_4$ Complexes 77
IV.A. Spectroscopic Background for $M_2X_4L_4$ Compounds[40,54] 77

IV.B. Theoretical Observations on $M_2X_4L_4$ Compounds. 81
IV.C. Two-Photon Spectroscopic Results of $M_2X_4L_4$ complexes. 82
IV.C.1. $Mo_2Cl_4(PMe_3)_4$ 82
IV.C.2. $Mo_2Br_4(PMe_3)_4$ 88
IV.C.3. $Mo_2I_4(PMe_3)_4$ 88
IV.C.4. $Mo_2Cl_4(PEt_3)_4$ 93
IV.C.5. $Mo_2Cl_4(AsMe_3)_4$ 93
IV.C.6. $W_2Cl_4(PMe_3)_4$ 98
IV.C.7. $MoWCl_4(PMe_3)_4$ 98
IV.C.8. *cis*-$Mo_2Cl_2(mhp)_2(PMe_2Ph)_2$ 103
IV.D. Discussion 107
IV.D.1. Effect of Halogen Substitution on the δ-manifold. 107
IV.D.2. Effect of σ-donating ligand on the δ-manifold. 112
IV.D.3. Effect of Metal Substitution on the δ-manifold. 113
IV.D.4. *cis*-$Mo_2Cl_2(mhp)_2(PMe_2Ph)_2$ 113
IV.E. Zwitterionic Character of the δδ* and δ^{*2} States. 114
Appendix I 116
Appendix II 123
References 126

LIST OF TABLES

Table I.1. Values for the polarization functions F, G, and H, depending on the eight polarization cases. From References 34 and 36. 34

Table I.2. Two-photon tensor patterns and the polarization ratio expected for each transition in the D_{2d} point group. From References 34, 36, and 38. 35

Table II.1. The twist angle (χ) for each of the compounds studied. The ligand abbreviations are given in the text. $Mo_2Cl_4(PMe_3)_4$ corresponds to a 90° twist. Values taken from Reference 26b. 38

Table III.1. Spectroscopic and structural data for $Mo_2Cl_4(\overset{\frown}{P\,P})_2$ compounds. $^1(\delta \rightarrow \delta^*)$ is the transition energy in cm^{-1}, ε is the extinction coefficient for the $^1(\delta \rightarrow \delta^*)$ transition at the maximum in $M^{-1}cm^{-1}$, $^3(\delta \rightarrow \delta^*)$ is the transition energy in cm^{-1} and χ is the twist angle in degrees. NM not measurable. Except as noted, the data was taken from Reference 26. 59

Table IV.1. The entries are in the form of nm ($M^{-1}cm^{-1}$). [a] reference 54a, [b] reference 40, and [c] reference 54b [d] reference 54c. [†]This band was only reported in the fluorescence spectrum and the extinction coefficient was not measured. 80

Table IV.2. Summary of data for the $^1(\delta \rightarrow \delta^*)$ and $^1(\delta^2 \rightarrow \delta^{*2})$ transition energies and the energy gap (ΔE) separating the $\delta\delta^*$ and δ^{*2} states as determined from the band maxima. The energies are in cm^{-1}. 108

Table IV.3. The metal-metal bond distance (in Å), overlap (S) of parent d_{xy} orbitals and one- (ΔW) and two-electron (K) energies in cm^{-1}. * S was determined from the oscillator strengths using Mulliken's relationship (Equation I.1), the references are for the oscillator strengths. NM not measured. ** This value is for *cis*-$Mo_2Cl_2(mhp)_2(PEt_3)_2$ 109

Table IV.4. The $^2(\delta \rightarrow \delta^*)$ transition energies for the $Mo_2X_4(PMe_3)_4^{+/-}$ series of compounds. From Reference 61 111

Table IV.5. Results of calculation to determine the percentage of zwitterionic character of the excited state. 114

LIST OF FIGURES

Figure I.1 A general scheme for photoinitiated multielectron chemistry in natural systems. A photon is absorbed at the receptor and the excited state which is produced initiates a chain of electron transfer reactions where the electron is moved further and further away from the receptor. Ultimately, the requisite number of electrons are stored at the multielectron site where the chemical reaction occurs..... 2

Figure I.2. Diagram of the thylakoid membrane of chloroplast showing the components of the electron-transfer scheme in green plants. P_{680} and P_{700} are the chlorophyll molecules that initiate the photoinduced electron transfer processes. Q represents the plastoquinone molecules. Cyt are the cytochrome molecules. FeS are the iron-sulfur proteins. A are the electron accepting chlorophyll molecules. Fd is ferrodoxin. FAD is ferrodoxin $NADP^+$ reductase and PC denotes the blue copper protein plastocyanin. 3

Figure I.3. The proposed simplified scheme of photoinduced multielectron chemistry. As in Figure I.1, the photon is absorbed by the receptor and multielectron chemistry occurs at the multielectron site. 6

Figure I.4. (top) The molecular orbital diagram for H_2^+ that results when one electron is placed in the molecular orbitals formed by the overlap of hydrogens' atomic 1s orbitals. ΔW is the one-electron energy. (bottom) The four electronic states that arise when two electrons are placed in the molecular orbitals of hydrogen. On the left side of the diagram, the 1s orbital of the hydrogen atom represents 0 on the energy scale. ΔW is the one electron energy, and K is the two-electron exchange energy. Since σ^2 and σ^{*2} are the same symmetry they mix together and gain some two-electron character. The energy separating the state then becomes $2\sqrt{\Delta W^2 + K^2}$ 7

Figure I.5. The potential energy diagram for the hydrogen molecule, showing the behavior of the states as the bond is stretched. In the strongly coupled limit ΔW (which is much greater than K) dominates the energy of the electronic states. In the weakly coupled limit, $\Delta W \sim 0$ and K determines the energy of the states..... 9

Figure I.6. The electronics states of ethylene as it is twisted about the C—C internuclear axis..... 12

Figure I.7. Molecular orbital diagram (D_{4h} symmetry) showing the metal-metal bonding in quadruply bonded dimers when two ML_4 (D_{4h}) fragments are brought together. 13

Figure I.8. The δ-manifold of electronic states that results when two electrons are placed in the δ orbitals. 15

Figure I.9. The dependence of the electronic states of the δ-manifold on internuclear twist angle (χ). The δ-bond is broken at $\chi = 45°$. There is a mirror image of the manifold from 45° – 90° that is not shown here..... 18

Figure I.10. The toroidal shaped electric field that is generated by an oscillating dipole. 21

Figure I.11. View down the axes of three oscillating dipoles, along with the cross-section of their emanating electric fields are shown. Constructive interference of the electric fields only occurs in "forward" direction where the three electric fields overlap..... 21

Figure I.12. The primary wave (•••) is at the frequency of the incident light. The secondary wave (- - -) that is generated when the oscillating dipoles are accelerating (at their turning points) is 90° out of phase with the primary wave. The refracted wave (—) is the superposition of the primary and secondary waves. Its phase relationship is determined by the 90° phase lag due to the secondary wave, plus a component related to the intensities of the primary and secondary waves. 22

Figure I.13. When a dipole is exposed to a very high electric field, the dipole becomes overdriven and can oscillate at multiples of the driving frequency. Here, the dipole oscillates also at twice the driving frequency..... 24

Figure I.14. a.) Second harmonic generation is an example where two frequencies ($h\nu_1$) are mixed through the second order susceptibility tensor, $\chi^{(2)}$, to yield a new frequency ($h\nu_2$), that is the sum of the incident frequencies. b.) In sum frequency generation, three frequencies ($h\nu_1$) are mixed through $\chi^{(2)}$ to yield a new frequency ($h\nu_3$) that is the sum of the three incident frequencies..... 29

Figure I.15. Two examples of nonlinear spectroscopy where a total of four frequencies are mixed through $\chi^{(3)}$. a.) Two-photon absorption (TPA), where two photons (ν_1) populate the excited state that then relaxes to the ground state by two-photon emission. b.) Coherent anti-Stokes Raman spectroscopy (CARS) is a more complex process, where ν_1 places the system in a virtual state that is driven down to a vibrationally excited state by ν_2. This excited state interacts with a second photon ν_1 and ultimately the scattered photon at frequency ν_s is detected..... 30

Figure II.1. A schematic drawing of the instrumentation used to perform TPE measurements. L1 is the long focal length lens used to reduce divergence of the laser beam. GL (Glan-Laser polarizer) DFR (Double Fresnel Rhomb), and SFR (Single Fresnel Rhomb) are the optics used to adjust the polarization state of the laser beam. S is the sample that is housed in a cryostat and PD is the pyroelectric photodetector. L2 and L3 are F/4 collection optics to couple the sample fluorescence to the detector after passing through an appropriate filter (F). The detector used depended on the molecule being studied as indicated in the text. The (·····) box represents the sample chamber. 43

Figure II.2. The dependence of idler and signal wavelengths on the BBO crystal angle. When the pump beam is normal to the crystal, the angle is 0°. The line is drawn at 710 nm which represents the degeneracy point, where the signal and idler wavelengths are the same. 45

Figure II.3. The variation of bandwidth with idler wavelength. Only the range from 800 – 2300 nm is shown. The bandwidth continues to rise to the blue, maximizing at ~1000 cm^{-1} at 710 nm. 47

Figure II.4. Comparison of the TPE spectrum taken with a (—)constant bandwidth (~0.3cm^{-1}) source and the (•••) Type I XPO. 48

Figure II.5. The polarization state of the laser beam is experimentally determined as shown here. Determination of circularly polarized light is shown in a.). The horizontally polarized laser beam (H) passes through the Glan-laser polarizer (GL) and its polarization is rotated by 90° to be vertically polarized (V) by the double Fresnel rhomb (DFR). The vertically polarized light is converted to be circularly polarized (C) by the single Fresnel rhomb (SFR). The laser beam is reflected by a mirror (M), where the handedness of the circular polarization is changed (C'). The polarization is ultimately changed to vertical after passing through the SFR and DFR a second time. The vertically polarized light does not pass through the GL. Vertically polarized light is determined by b.). The mirror is replaced by a Glan-Thompson polarizer (GT) arranged to block vertically polarized light and the DFR is rotated until no laser light is seen to pass through the GT. 50

Figure III.1. The effect of the twist angle (χ) and overlap (S) on the electronic states of the δ-manifold. 56

Figure III.2. a.) The energy of the $^1\delta\delta^*$ (hollow) and $^3\delta\delta^*$ (filled) states for $Mo_2Cl_4(\overset{\frown}{P\,P})_2$ compounds. b.) The energy difference between the $^1\delta\delta^*$ and $^3\delta\delta^*$ states (solid) is essentially constant at 10500 cm^{-1}. This corresponds to 2K, where K is the two-electron exchange energy. The extinction coefficient (hollow) for the $^1(\delta \rightarrow \delta^*)$ transition is also shown. The data was taken from Reference 26. 60

Figure III.3. Absorption (—) and low temperature emission (•••) spectra of $Mo_2Cl_4(S,S\text{-dppb})_2$ in 3-methylpentane. The band in the absorption spectrum at 734 nm has been assigned as the $^1(\delta \rightarrow \delta^*)$ transition and the emission (925 nm) is assigned as $^1(\delta^* \rightarrow \delta)$. The emission spectrum was not corrected for the instrument response. 62

Figure III.4. The absorption spectrum of 3-methylpentane (•••) and two-photon fluorescence excitation spectrum of $Mo_2Cl_4(S,S\text{-dppb})_2$ (—). The bands in the solvent absorption spectrum at 1180 nm and 1380 – 1500 nm are manifested in the two-photon excitation spectrum. 63

Figure III.5. The absorption (•••) and two-photon fluorescence excitation (—) spectra of $Mo_2Cl_4(S,S\text{-dppb})_2$. When the artifacts due to solvent absorption are ignored, the two-photon fluorescence excitation spectrum displays a maximum at 625 nm..... 65

Figure III.6. a.) The polarization ratio (Ω) is plotted versus the wavelength and has a value less than 1 across the entire band. b.) The power dependence, which is a plot of the observed fluorescence intensity (I_{fl}) versus relative laser intensity (power) has a slope of 2.02. The line represents the best fit following a linear least squares analysis. 66

Figure III.7. Absorption (—) and low temperature emission (•••) spectra of $Mo_2Cl_4(depe)_2$. The spectra were collected in 3-methylpentane solution. The emission spectrum was collected at 77K..... 68

Figure III.8. The absorption spectrum of 1:1 CH_2Cl_2/toluene (•••) and two-photon fluorescence excitation spectrum (—) of $Mo_2Cl_4(depe)_2$ in this solvent. As with $Mo_2Cl_4(S,S\text{-dppb})_2$, the most prominent bands can be attributed to artifacts due to strong solvent absorption. If the artifacts are ignored, a band may be observed at ~1495 nm..... 69

Figure III.9. The absorption spectrum (—) and the low temperature (120K) laser induced fluorescence spectrum (•••) of $Mo_2Cl_4(dppe)_2$ in 3-methylpentane..... 71

Figure III.10. Two-photon fluorescence excitation spectrum of $Mo_2Cl_4(dppe)_2$ in 1:1 CH_2Cl_2/toluene at 120 K. The only bands seen can be attributed to artifacts due to solvent absorption..... 72

Figure III.11. The absorption spectrum of $Mo_2Cl_4(dmpm)_2$ in 3-methylpentane..... 73

Figure III.12. The time dependent fluorescence of $Mo_2Cl_4(dmpm)_2$ in 3-methylpentane at 120 K when excited at 600 nm (top) and 950 nm (bottom). The one-photon induced fluorescence has a lifetime of 83 ns. The two-photon induced fluorescence was difficult to fit due to the low fluorescence but yielded a biexponential decay values of ~10 ns and ~80 ns. The short component may be due to scattered laser light. The fluorescence was detected at 675 nm. The one-photon induced fluorescence signal represents the average of 50 laser shots, while the two-photon induced fluorescence signal was collected with 5000 laser shots. Also, the slits on the monochromator were much wider (8 mm) for the two-photon induced fluorescence than for the one-photon induced fluorescence the slits were 0.1 mm..75

Figure IV.1. The absorption spectrum of $Mo_2Cl_4(PMe_3)_4$ in 3-methylpentane at room temperature. The numbering scheme for the bands was developed in the literature. As many as eleven bands can be seen in the spectra of $M_2X_4L_4$ compounds, depending on the sample conditions. 79

Figure IV.2. The effect of halogen atom substitution on the metal-based orbitals of $M_2X_4(PH_3)_4$ compounds. The left side of the figure is before the effect is "turned on" and the metal-based orbitals are independent of the halogen. The right side of the figure shows how the metal-based orbitals are affected by the halogen p orbitals. 83

Figure IV.3. Absorption spectra (in 3-methylpentane) of the $Mo_2X_4(PMe_3)_4$ series; X = Cl (—), X = Br (- - -), X = I (•••). As the halide becomes less electronegative, the $^1(\delta \rightarrow \delta^*)$ transition red-shifts due to halide p electrons encroaching into the metal-metal bonding orbitals. 84

Figure IV.4. The absorption spectrum (•••) of $Mo_2Cl_4(PMe_3)_4$ in 3-methylpentane, where the $^1(\pi \rightarrow \delta^*)$ transition has been expanded by a factor of 15 to show that it is not coincident with the $^1(\delta^2 \rightarrow \delta^{*2})$ (—) transition. The emission spectrum (- - -) is generated when the compound is excited with either one or two photons. The two-photon excitation spectrum was generated by exciting in the near-infrared (/////).... 85

Figure IV.5. Measurements from the two-photon fluorescence excitation spectrum of $Mo_2Cl_4(PMe_3)_4$ in 3-methylpentane. a.) The power dependence when excited with 860 nm vertically polarized light. The line represents a best fit to a slope of 2.00. b.) The polarization ratio is less than one across the $^1(\delta^2 \rightarrow \delta^{*2})$ transition..... 87

Figure IV.6. The absorption (- - -) and two-photon fluorescence excitation (—) spectra of Mo2Br4(PMe3)4 in 3-methylpentane at room temperature. The $^1(\delta \rightarrow \delta^*)$ transition has a maximum at 598 nm and the $^1(\delta^2 \rightarrow \delta^{*2})$ transition has a maximum at 470 nm. The region in the near-infrared (/////) corresponds to the excitation wavelength of the two-photon spectrum. 89

Figure IV.7. Measurements from the two-photon fluorescence excitation spectrum of $Mo_2Br_4(PMe_3)_4$ in 3-methylpentane. a.) The power dependence when excited with 950 nm vertically polarized light. The line represents a best fit to a slope of 1.93. b.) The polarization ratio is less than one across the $^1(\delta^2 \rightarrow \delta^{*2})$ transition. The rise on the blue edge can be attributed to one-photon excitation of the red edge of the $^1(\delta \rightarrow \delta^*)$ transition..... 90

Figure IV.8. The absorption (- - -) and two-photon fluorescence excitation (—) spectra of $Mo_2I_4(PMe_3)_4$ in 3-methylpentane at room temperature. The $^1(\delta \rightarrow \delta^*)$ transition has a maximum at 636 nm and the $^1(\delta^2 \rightarrow \delta^{*2})$ transition has a maximum at 505 nm. The region in the near-infrared (/////) corresponds to the excitation wavelength for the two-photon spectrum..... 91

Figure IV.9. Measurements from the two-photon excitation spectra of $Mo_2I_4(PMe_3)_4$ in 3-methylpentane. a.) The power dependence when excited with 990 nm vertically polarized light. The line represents a best fit to a slope of 1.92. b.) The polarization ratio is less than one across the $^1(\delta^2 \rightarrow \delta^{*2})$ transition. The rise on the blue edge can be attributed to one-photon excitation of the red edge of the $^1(\delta \rightarrow \delta^*)$ transition... 92

Figure IV.10. The absorption (- - -) and two-photon fluorescence excitation (—) spectra of $Mo_2Cl_4(PEt_3)_4$ in 3-methylpentane at room temperature. The $^1(\delta \rightarrow \delta^*)$ transition has a maximum at 591 nm and the $^1(\delta^2 \rightarrow \delta^{*2})$ transition has a maximum at 474 nm. The region in the near-infrared (/////) corresponds to the excitation wavelength for the two-photon spectrum..... 94

Figure IV.11. Measurements from the two-photon excitation spectra of $Mo_2Cl_4(PEt_3)_4$ in 3-methylpentane. a.) The power dependence when excited with 950 nm vertically polarized light. The line represents a best fit to a slope of 1.99. b.) The polarization ratio is less than one across the $^1(\delta^2 \rightarrow \delta^{*2})$ transition. The rise on the blue edge can be attributed to one-photon excitation of the red edge of the $^1(\delta \rightarrow \delta^*)$ transition. The rise on the red edge is likely due to noise..... 95

Figure IV.12. The absorption (- - -), fluorescence (···), and two-photon fluorescence excitation (—)spectra of $Mo_2Cl_4(AsMe_3)_4$ in 3-methylpentane. The $^1(\delta \rightarrow \delta^*)$ transition has a maximum at 573 nm, the $^1(\delta^* \rightarrow \delta)$ has a maximum emission at 638 nm and the $^1(\delta^2 \rightarrow \delta^{*2})$ has a maximum at 455 nm. The region in the near infrared (/////) corresponds to the two-photon excitation wavelength..... 96

Figure IV.13. Measurements from the two-photon excitation spectra of $Mo_2Cl_4(AsMe_3)_4$ in 3-methylpentane. a.) The power dependence when excited at 910 nm with vertically polarized light. The line represents a best fit to a slope of 2.09. b.) The polarization ratio is less than one across the $^1(\delta^2 \rightarrow \delta^{*2})$ band.polarization ratio is less than 1 across the observed band, again indicating that the initial and final states have the same symmetry. 97

Figure IV.14. The absorption (- - -) and two-photon fluorescence excitation (—) spectra of $W_2Cl_4(PMe_3)_4$ in 3-methylpentane. The $^1(\delta \rightarrow \delta^*)$ transition has a maximum at 660 nm and the $^1(\delta^2 \rightarrow \delta^{*2})$ transition maximizes at 520 nm. The hashed (/////) box in the near infrared corresponds to the two-photon excitation wavelength region. .. 99

Figure IV.15. Measurements from the two-photon excitation spectra of $W_2Cl_4(PMe_3)_4$ in 3-methylpentane. a.) The power dependence of the fluorescence when excited at 1050 nm. The line represents a best fit with a slope of 1.93. b.) The polarization ratio is less than across the $^1(\delta^2 \rightarrow \delta^{*2})$ transition. The rise on the blue edge can be attributed to excitation of the $^1(\delta \rightarrow \delta^*)$ transition. 100

Figure IV.16. The absorption (- - -) and two-photon fluorescence excitation (—) spectra of $MoWCl_4(PMe_3)_4$ in 3-methylpentane. The $^1(\delta \rightarrow \delta^*)$ transition has a maximum at 635 nm and the $^1(\delta^2 \rightarrow \delta^{*2})$ transition maximizes at 481 nm. The hashed (/////) box in the near infrared corresponds to the two-photon excitation wavelength region. 101

Figure IV.17. Measurements from the two-photon excitation spectra of $MoWCl_4(PMe_3)_4$ in 3-methylpentane. a.) The polarization ratio is less than across the $^1(\delta^2 \rightarrow \delta^{*2})$ transition. The rise on the blue edge can be attributed to excitation of the $^1(\delta \rightarrow \delta^*)$ transition, while the rise on the red edge is due to noise. b.) The power dependence of the fluorescence when excited at 950 nm. The line represents a best fit with a slope of 1.82 102

Figure IV.18. The absorption spectrum of *cis*-$Mo_2Cl_2(mhp)_2(PMe_2Ph)_2$ in benzene at room temperature. The spectrum is rather featureless and most of the bands do not result in population of the emissive $^1\delta\delta^*$ state. 104

Figure IV.19. The absorption (- - -), fluorescence (···) and two-photon fluorescence excitation (—) spectra of *cis*-$Mo_2Cl_2(mhp)_2(PMe_2Ph)_2$ in benzene. The $^1(\delta \rightarrow \delta^*)$ transition has a maximum at 555 nm, the $^1(\delta^* \rightarrow \delta)$ has a maximum at 615 nm and the two-photon spectrum exhibits two maxima, one at 390 nm and the other at 424 nm. The vertical black line is at 410 nm at represents the valley between the two bands. The hashed box (/////) represents the two-photon excitation region..... 105

Figure IV.20. Measurements from the two-photon excitation spectra of *cis*-$Mo_2Cl_2(mhp)_2(PMe_2Ph)_2$ in benzene. a.) The polarization ratio has a value of 1 from 360 – 410 nm and falls to be less than one from 410-460 nm. The vertical line is at 410 nm where Ω changes. b.) The power dependence of the fluorescence when excited at 860 nm. The line represents a best fit with a slope of 2.02..... 106

Figure AI.1. Two extremes of orbital overlap in bond formation The nuclei are represented by black dots. a.) The orbitals are overlapped very well and the CNDO approximation is not valid. b.) The orbitals are not overlapped very well and the CNDO approximation is valid..... 120

Chapter I

Introduction

At the heart of many natural processes is the ability to store multiple electrons in one place; thereby providing a route to multielectron chemistry. A general scheme for photoinitiated multielectron chemistry in naturally occurring systems is outlined in Figure I.1. In this scheme, light is absorbed at the photon receptor and results in a series of electron transfer reactions until the requisite number of electrons are stored at the multielectron site. While this sounds like a fairly simple and straightforward process, it is unique to natural systems.

The complexity of photoinduced multielectron chemistry in natural systems is typified by the photosynthetic production of sugar and oxygen from carbon dioxide and water. Photosynthesis in green plants occurs in the thylakoid membrane of chloroplasts and is comprised of two reaction centers, Photosystems I and II (PSI and PSII).[1] The reduction of $NADP^+$ and ultimate production of six-carbon sugars occurs in PSI. The multielectron oxidation of water occurs in PSII. While PSI and PSII are working concomitantly, it is easiest to describe the process (shown in Figure I.2) by starting with

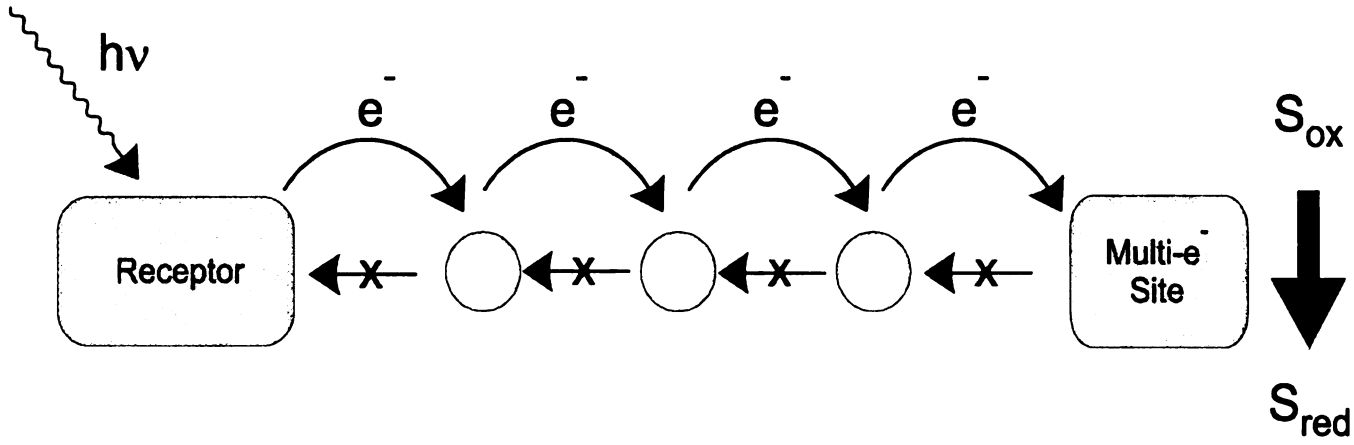

Figure I.1. A general scheme for photoinitiated multielectron chemistry in natural systems. A photon is absorbed at the receptor and the excited state which is produced initiates a chain of electron transfer reactions where the electron is moved further and further away from the receptor. Ultimately, the requisite number of electrons are stored at the multielectron site where the chemical reaction occurs.

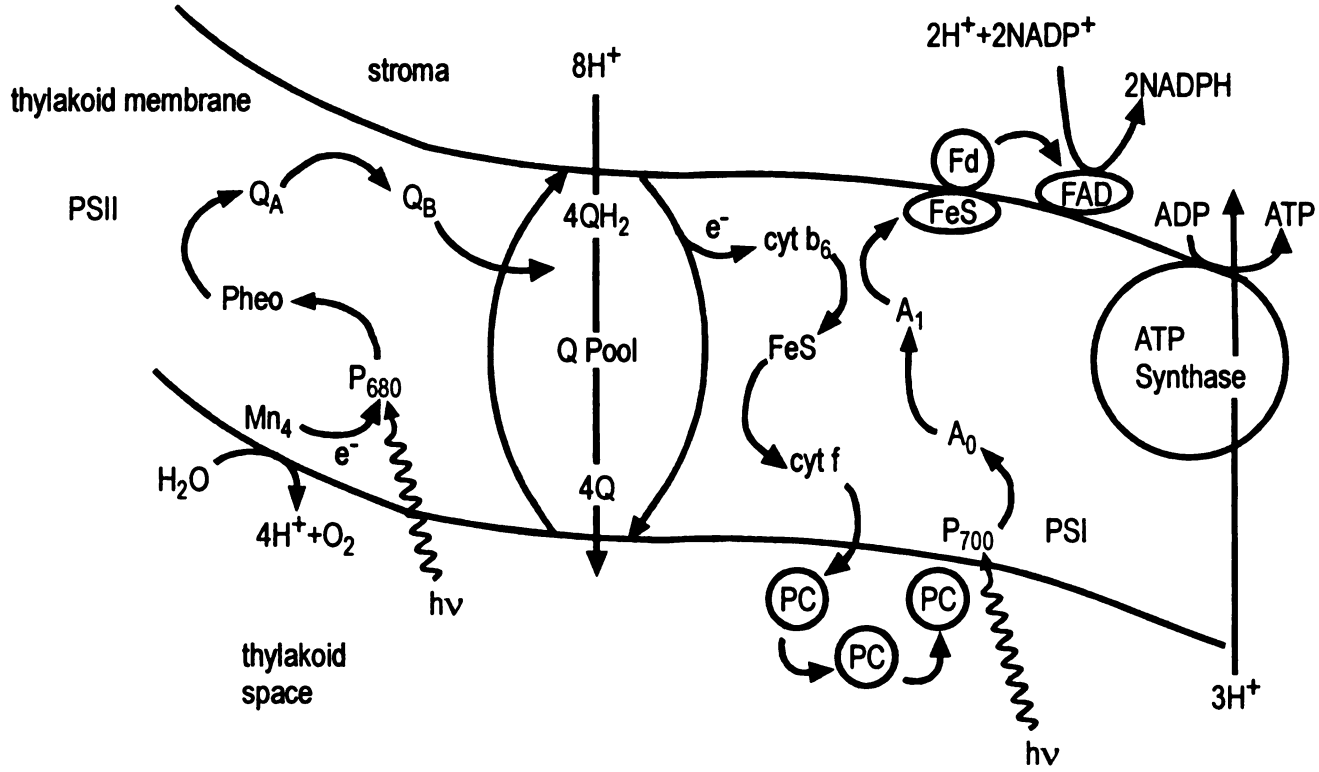

Figure I.2. Diagram of the thylakoid membrane of chloroplast showing the components of the electron-transfer scheme in green plants. P_{680} and P_{700} are the chlorophyll molecules that initiate the photoinduced electron transfer processes. Q represents the plastoquinone molecules. Cyt are the cytochrome molecules. FeS are the iron-sulfur proteins. A are the electron accepting chlorophyll molecules. Fd is ferrodoxin. FAD is ferrodoxin $NADP^+$ reductase and PC denotes the blue copper protein plastocyanin.

the absorption of a photon by chlorophyll P_{680} (680 refers to the λ_{max} in the excitation spectrum of this chlorophyll) or one of its antenna pigments in PSII. This $\pi\pi^*$ excitation produces P_{680}^* which is both a strong reductant and oxidant. P_{680}^* reduces pheophytin by rapidly transferring an electron to yield the P_{680}^+ — pheophytin$^-$ species. The pheophytin$^-$ reduces plastoquinone Q_A by an electron transfer and ultimately the electron is transferred to plastoquinone Q_B. Once two electrons have reduced Q_B, it gathers two protons and leaves the binding site as Q_BH_2. When Q_BH_2 leaves the binding site, it is replaced by another plastoquinone from the quinone pool. The cytochrome b_6/f complex ultimately oxidizes Q_BH_2 leading to transmembrane proton transfer. Through the cytochrome b_6/f complex, the electron is transferred to the blue copper protein plastocyanin and into PSI where it reduces the P_{700}^+ that was produced earlier by the absorption of a photon and electron transfer to an electron accepting chlorophyll (A_0). The electron then moves through a series of acceptors, iron sulfur proteins, ferrodoxin and ferrodoxin $NADP^+$ reductase to reduce $NADP^+$ to NADPH. The cycle is completed by the reduction of P_{680}^+ by the Y_z tyrosine residue that is itself reduced by the Mn_4 oxygen evolving complex (OEC). The OEC goes through five oxidation states $S_0 \rightarrow S_4$. Once in the S_4 oxidation state, water is oxidized to release O_2 and produce the proton necessary for the reduction of $NADP^+$ to NADPH.

The current understanding of photosynthesis, summarized above in a paragraph, is the culmination of centuries of work. While for much of that time the scientific community did not possess the tools needed to study the kinetics, thermodynamics or structure-functions relationships that are available today; they did have the insight to perform simple yet brilliant experiments. Perhaps the earliest documented scientific study of photosynthesis was reported by Joseph Priestley.[2] His experiment was simple – a piece of mint was placed in a sealed jar. After several days, the environment within the jar was able to support both flame and life and he concluded that oxygen must be the product of light driven reaction that occurred in the plant.

I.A Zwitterionic Excited States

To circumvent some of the complexities associated with studying natural systems, a different approach can be taken – use a system with no intermediates (Figure I.3). While this is a conceptually simple idea and has the merit of being relatively easy to study, the difficulty arises when trying to find such a system.

The greatest challenge in finding a new system and thus a new route to photoinduced multielectron chemistry is finding a system with the proper characteristics. The most significant characteristic is accessibility of a photoinduced excited state that possesses more than one electron that is available to do chemistry. This property is revealed in the quantum mechanical description of the hydrogen molecule (see Appendix I for a detailed derivation).[3,4,5] Figure I.4(top) shows the molecular orbital diagram for H_2^+ that results from the overlap of two atomic 1s orbitals. The σ bonding orbital is formed by the constructive overlap of the two atomic 1s orbitals, while the σ^* orbital is formed by the destructive overlap. Since the molecule possesses only one electron, the orbital energies are the same as the state energies and in the context of this dissertation, the energetic separation of the σ and σ^* molecular orbitals will be defined as ΔW, the "one electron" energy.

When a second electron is added to the molecule it can be placed in either the σ or σ^* orbital. Because of this, there are four nondegenerate states that must be considered (Figure I.4(bottom)). The lowest energy state, σ^2, results when both electrons are placed in the lowest energy (σ) molecular orbital. The highest energy state, σ^{*2}, is produced when both electrons are placed in the highest energy molecular orbital. To a simple approximation, the energy separating the σ^2 and σ^{*2} states is $2\Delta W$. It is also possible to have one electron in each of the σ and σ^* orbitals. With this configuration, the spin of the electrons must be considered. Obeying Hund's Rule, the lowest energy of

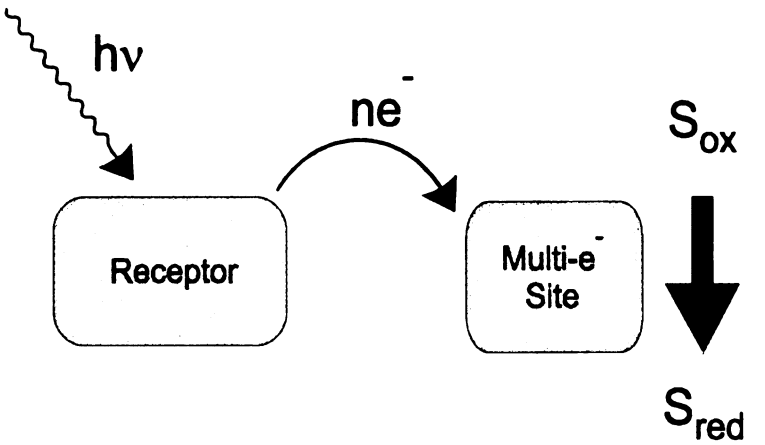

Figure I.3. The proposed simplified scheme of photoinduced multielectron chemistry. As in Figure I.1, the photon is absorbed by the receptor and multielectron chemistry occurs at the multielectron site.

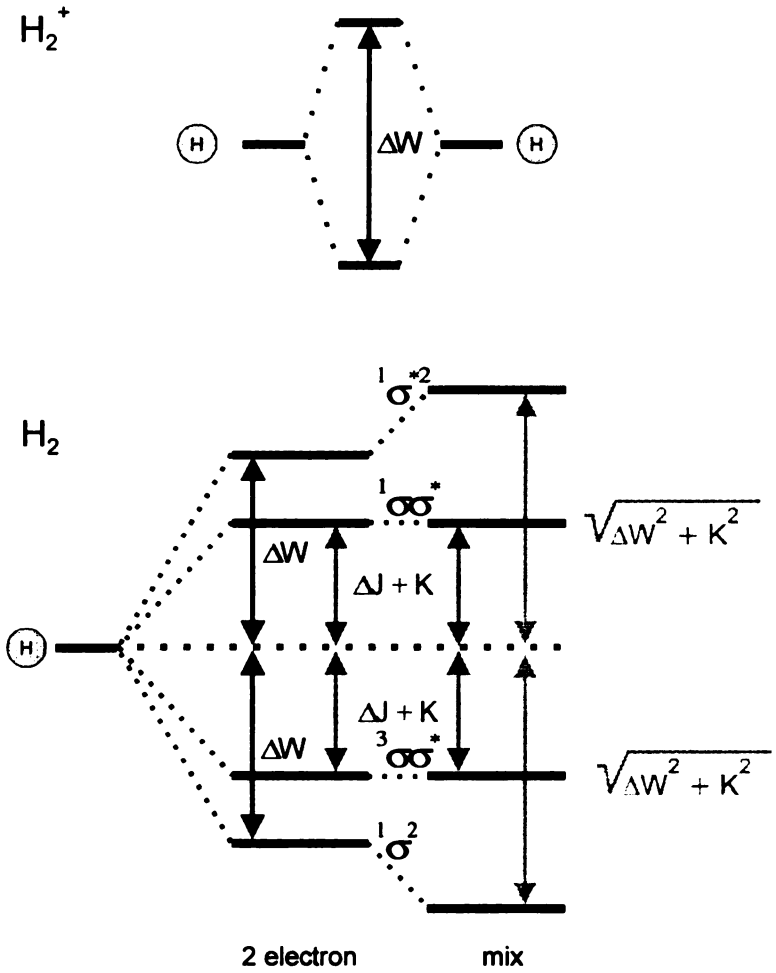

Figure I.4. (top) The molecular orbital diagram for H_2^+ that results when one electron is placed in the molecular orbitals formed by the overlap of hydrogens' atomic 1s orbitals. ΔW is the one-electron energy. (bottom) The four electronic states that arise when two electrons are placed in the molecular orbitals of hydrogen. On the left side of the diagram, the 1s orbital of the hydrogen atom represents 0 on the energy scale. ΔW is the one electron energy, and K is the two-electron exchange energy. Since σ^2 and σ^{*2} are the same symmetry they mix together and gain some two-electron character. The energy separating the state then becomes $2\sqrt{\Delta W^2 + K^2}$

these two $\sigma\sigma^*$ states is the $^3\sigma\sigma^*$ state, and the highest energy is $^1\sigma\sigma^*$. The energy separating these two states is 2K, where K is the two electron exchange energy. It is simply the energy required to move an electron from one side of the molecule to the other and in the limit of infinite separation corresponds to the electron affinity and ionization potential of atomic hydrogen. Since σ^2 and σ^{*2} both have the same symmetry, the two states mix together, giving rise to off-diagonal elements in the Hamiltonian matrix.[6] This results in a certain amount of two electron character being present, and leads to the states being repelled from one another. Their separation becomes $2\sqrt{\Delta W^2 + K^2}$ as shown in Figure I.4b.

From these definitions and the more complete potential energy diagram for the hydrogen molecule (Figure I.5) some interesting observations and conclusions can be made. The hydrogen molecule is at its equilibrium geometry at the potential energy minimum of the σ^2 ground state potential energy curve. The two 1s orbitals overlap and the strongly coupled electrons form the σ bond. As the molecule is pulled apart, however, the situation changes quite dramatically. Ultimately, the σ bond is ruptured leaving two hydrogen atoms (or radicals). Therefore, as the bond is stretched the wavefunction describing the electrons begins to acquire a great deal of diradical character. The Pauli Principle dictates that electrons with the same quantum numbers cannot occupy the same orbital. Thus, a molecule on the $^3\sigma\sigma^*$ potential curve must also dissociate to a diradical.

Consider the molecule on the σ^2 potential energy curve at a point where the bond has not fully ruptured, but is far removed from the equilibrium geometry. If a molecule at this point of the potential energy curve absorbs energy and is promoted to either $^1\sigma\sigma^*$ or $^1\sigma^{*2}$, the electron must be transferred from one side of the "molecule" to the other in order to maintain its singlet spin configuration. Therefore, these two highest energy states are described as being zwitterionic.

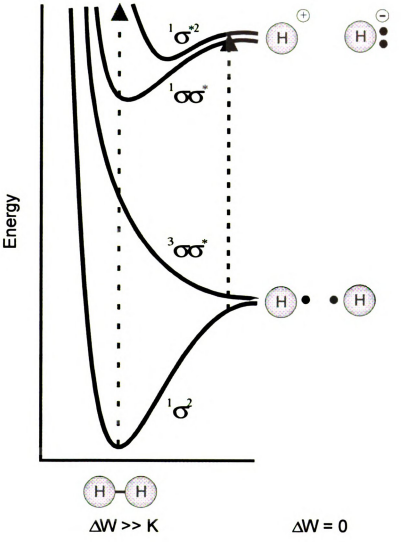

Figure I.5. The potential energy diagram for the hydrogen molecule, showing the behavior of the states as the bond is stretched. In the strongly coupled limit ΔW (which is much greater than K) dominates the energy of the electronic states. In the weakly coupled limit, $\Delta W \sim 0$ and K determines the energy of the states.

The disposition of the potential energy curves can also provide some insight about the relative characteristics of each of the electronic states. In the region where the electrons are strongly coupled there is a relatively large energy gap separating σ^2 and $^3\sigma\sigma^*$. This is followed by a small energetic separation of the $\sigma\sigma^*$ states and then another large gap separating $^1\sigma\sigma^*$ and σ^{*2}. This ordering of states is common. It stems from the fact that ΔW is the dominant term in the energies of these states and that the two electron terms, which arise largely from the effect of correlated electron motion, are relatively small.

When the electrons are weakly coupled there is very little overlap of the parent atomic orbitals and the situation is markedly different. The gap separating σ^2 and $^3\sigma\sigma^*$ is small because the only energy required is to flip the spin of an electron that is at best weakly coupled to the other electron (when the bond is fully ruptured, neither electron is influenced by the other electron). The gap between the $\sigma\sigma^*$ states is relatively large because moving from $^3\sigma\sigma^*$ to $^1\sigma\sigma^*$ requires placing two electrons into a volume that is essentially the size of a 1s atomic orbital. The gap between the $^1\sigma\sigma^*$ and $^1\sigma^{*2}$ states again is small because these states are simply the symmetric and antisymmetric linear combinations of having two electrons on one half of the molecule. Of course, the gaps separating the diradical and zwitterionic pairs of states coalesce to degeneracy when the parent atomic orbitals are completely decoupled. At this point, these "molecular" states correspond to the electron transfer reaction $2H \rightarrow H^+ + H^-$. Thus, the relative energetic displacement of the states provides a great deal of qualitative information about the character of the states.

Perhaps the most interesting aspect about the preceding description of the hydrogen molecule is that while the overall description was postulated in the earliest days of molecular quantum mechanics, and it has often been invoked in describing reaction pathways, it has never been experimentally confirmed. Other than the work being reported here, there have been some recent studies on derivatives of ethylene that have

provided experimental evidence for the character of the states of a two-center, two-electron bond. [7,8]

As ethylene is twisted about its sigma bond (Figure I.6) a scenario quite analogous to stretching molecular hydrogen develops. At the ethylene equilibrium geometry the electrons that form the π bond are very highly coupled and the bond is strong. However, as one half of the molecule is twisted with respect to the other, the bond weakens until it is ultimately annihilated at a twist angle of 90 degrees. Along this journey, the electrons became less and less coupled. Mulliken originally indicated that as twisting occurs, the manifold of four states ultimately is reduced to two states when the bond is broken, a diradical ground state and a zwitterionic excited state.[9] Ohno, in a more recent treatment, confirmed the ideas postulated by Mulliken and applied them to more complicated π systems.[10] As the twist is carried to 180 degrees, the bond is reformed and the typical four-state manifold is reestablished. This evolution of states has been invoked from both theoretical[11] and experimental[12] points of view to explain product distributions and solvent dependencies of organic photoreactions involving *cis-trans* isomerizations and photocyclizations. However, the diradical and zwitterionic states eluded detection and were named the "phantom states".[13] Recently, however, some spectroscopic studies have revealed the true nature and disposition of these states.[7,8]

The most complete picture of these states is found in quadruply bonded metal dimers ($M\overset{4}{\text{---}}M$). These dimers possess four bonds and the shortest metal-metal distance in inorganic chemistry. In the cases of hydrogen and ethylene the two electrons that form σ and π bonds respectively are strongly coupled to one another due to the good overlap of the parent σ and π atomic orbitals. Because of this, the diradical and zwitterionic character of the states only manifests itself as the electrons become weakly coupled when the bond breaks. As shown in the molecular orbital diagram (Figure I.7)

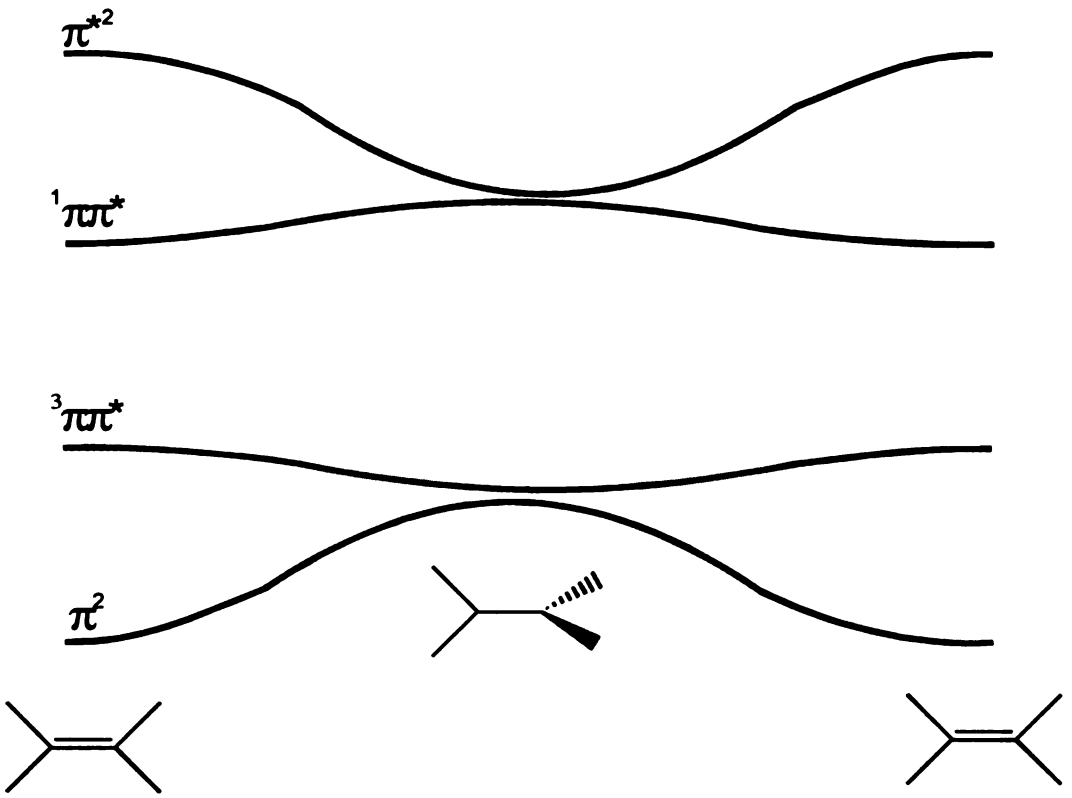

Figure I.6. The electronics states of ethylene as it is twisted about the C—C internuclear axis.

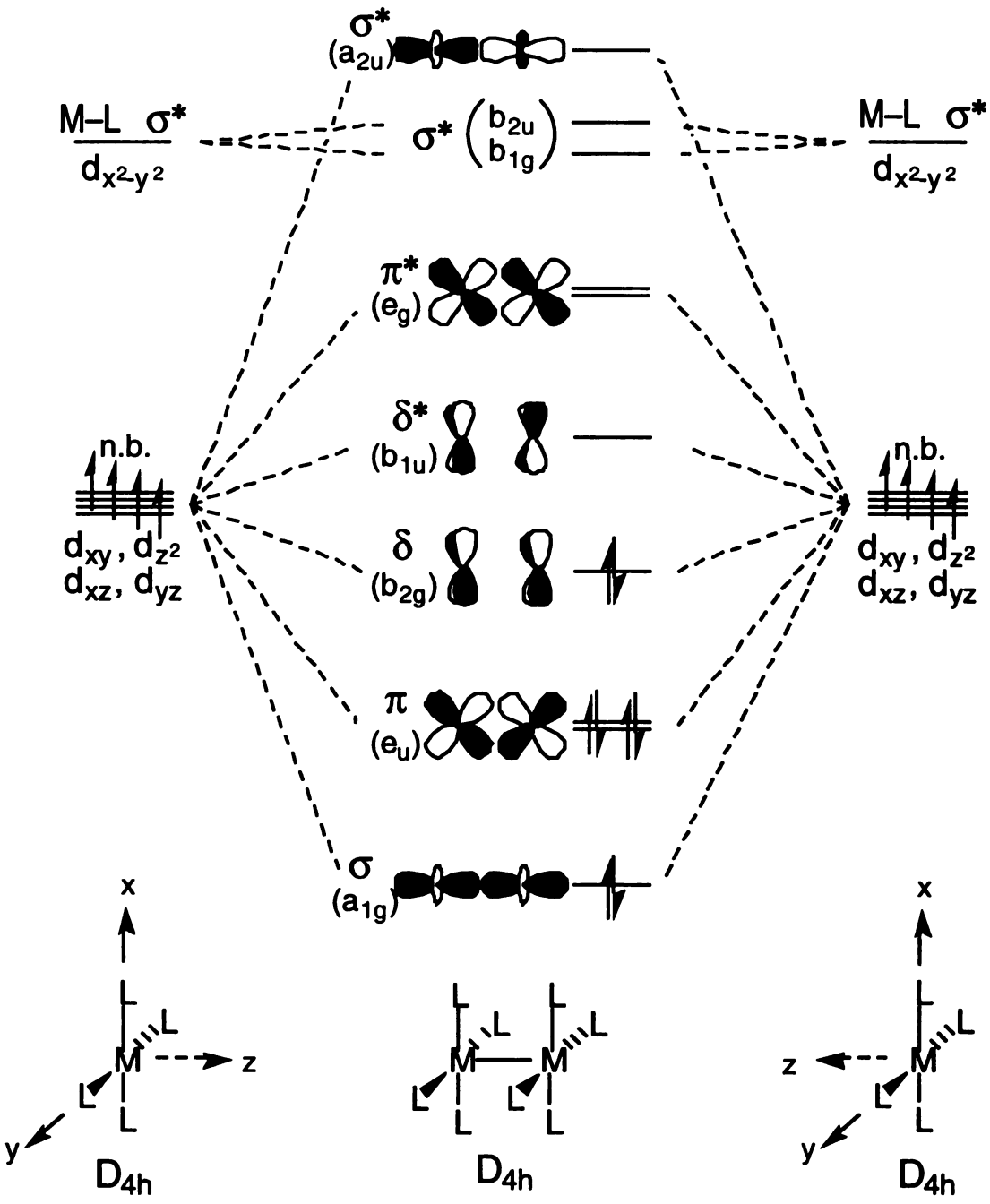

Figure I.7. Molecular orbital diagram (D_{4h} symmetry) showing the metal-metal bonding in quadruply bonded dimers when two ML_4 (D_{4h}) fragments are brought together.

for (M—^{4}— M) complexes, the six electrons that pair-wise form the σ and 2 π bonds are strongly coupled due to the good overlap of the parent d_{z^2}, and (d_{xz},d_{yz}) atomic orbitals respectively. Because of the good overlap, these bonds are expected to display the diradical and zwitterionic states only as the metals are pulled apart. The fourth bond, the δ bond, is different however. Since the δ bond is formed by the poor face-to-face overlap of two d_{xy} atomic orbitals, the electrons that reside in it are weakly coupled. Thus, the δ bond can be thought of as lying in the nether world between a strong covalent bond and two free metal fragments. The δ-bond has been cast into the theoretical form of hydrogen and ethylene.[14] The electronic states of the δ-manifold are shown Figure I.8. It can be seen from this diagram that, even in the equilibrium geometry, the energetic disposition of states is consistent with weakly coupled electrons. The energy gap that separates the low energy diradical states is small; there is a large gap between the δδ* states and then a small gap between the zwitterionic states. A significant feature of the δ-manifold is the symmetry displayed. The energy gap between the diradical states is equal to the energy gap between the zwitterionic states. Because of the weak coupling of the electrons that form the δ-bond, quadruply bonded metal dimers provide a unique opportunity to study a weak two-center, two-electron bond.

One particularly interesting feature of (M—^{4}— M) complexes is that as one half of the molecule is rotated with respect to the other, only the δ bond is broken. The σ bond, due to its cylindrical symmetry about the internuclear axis is unaffected by rotation. The lobes of the orthogonal π orbitals are rotated into each other as the molecule is twisted and there is no net change in the energy of these bonds since as they are being broken they are also being reformed. Proper choice of the ligand set then allows for series of molecules to be made with varied coupling of the parent (d_{xy}) atomic orbitals. In affect, this provides a means to "break" the δ-bond in a step-wise fashion.[15]

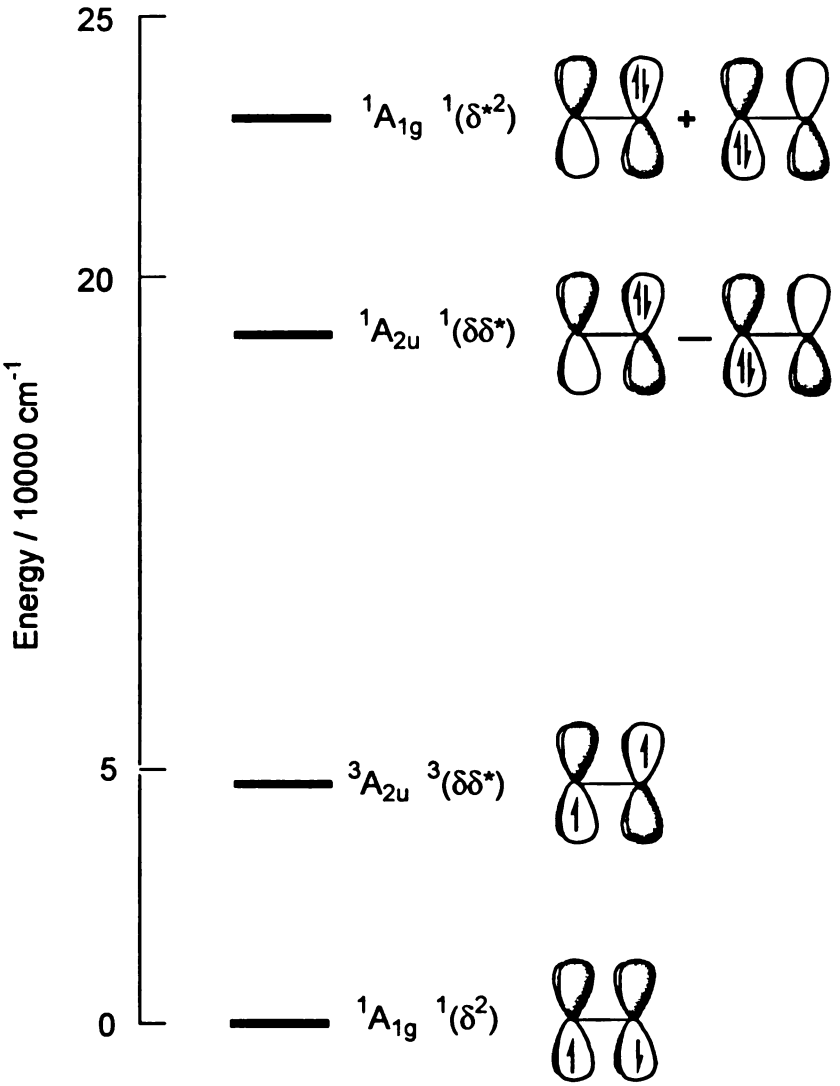

Figure I.8. The δ-manifold of electronic states that results when two electrons are placed in the δ orbitals.

I.A.1. History of the Delta Bond

When Cotton *et al* prepared $K_2Re_2Cl_8 \cdot H_2O$ in 1964, the bond between the Re centers was predicted to have the electronic configuration of $\sigma^2\pi^4\delta^2$ that implied one σ-, two π- and one δ-bond.[16] The crystal structure supported this configuration. The internuclear separation was small (~2.2Å), and implied that there could be some overlap of the d_{xy} orbitals to form a δ-type bond. Furthermore, the Cl^- ligands were eclipsed. If the molecule was only triply bonded, the cylindrical symmetry of the σ and two π bonds would allow for rotation about the internuclear axis and lead to a staggered disposition of the ligands to relieve some steric strain. Lastly, the compound was observed to be diamagnetic, which indicated that all of the electrons were paired.

Cowman and Gray undertook an exhaustive study of the spectroscopy of this compound in order to learn more about the electronic structure of quadruply bonded metal dimers.[17] From spectroscopic measurements on single crystals, they were able to unambiguously assign the lowest energy transition observed in the UV/vis spectrum as $^1\delta\delta^* \leftarrow \delta^2$ ($^1(\delta \rightarrow \delta^*)$). The transition was observed to be polarized preferentially along the internuclear (z) axis and progressed with an excited state frequency of 248 cm^{-1}. This was consistent with a ground state metal-metal stretching frequency of 274 cm^{-1} reported in an earlier Raman study.[18] The spectroscopy of this compound also served to reveal the weakness of the δ bond.[19] Although the $^1(\delta \rightarrow \delta^*)$ transition is dipole and spin allowed, it is very weak (ε_{max} = 1530 $M^{-1}cm^{-1}$). The analogous $^1(\pi \rightarrow \pi^*)$ transition in an organic compound could have an extinction that could be several orders of magnitude higher. Mulliken showed that the intensity of electronic transitions is very dependent on the coupling of the parent atomic orbitals. The oscillator strength (which is intimately related to the extinction coefficient) can be related to the orbital overlap:[20]

$$f = 1.096 \times 10^{11}\, \bar{\nu} S^2 r^2 \qquad \text{(I.1)}$$

where $\bar{\nu}$ is the transition energy in cm^{-1}, r is the internuclear separation in cm, and S is the overlap of the parent atomic orbitals. Using the observed oscillator strength of the $^1(\delta \rightarrow \delta^*)$ transition ($f = 0.023$[21]), the overlap was determined to be 0.08.

Not surprisingly, the δ bond was also of great interest to theoretical chemists. The computational techniques of the time had proven useful for σ and π bonds, and the δ bond represented a new challenge. However, the δ bond defied the techniques. Calculations carried out by Benard on $Re_2Cl_8^{2-}$ predicted a staggered geometry.[22] Also, the calculations indicated that the ground state would be a paramagnetic triplet instead of the observed diamagnetic singlet. Computational techniques advanced as computers became more powerful. This allowed for expanded basis sets to be used and thus made it possible to account for higher order effects such as electron correlation and relativity. In 1982, Hay, took advantage of the computational power of Cray computers to perform calculations on $Re_2Cl_8^{2-}$ at a level that provided qualitative agreement with experimental observations.[23]

1.A.2. Electronic States of the δ-Manifold

The electronic state diagram for the δ-manifold is shown in Figure I.8. The ground state was essentially discovered with the synthesis of $Re_2Cl_8^{2-}$. Since the molecule is diamagnetic the ground state is a singlet. The next highest energy state is $^3\delta\delta^*$. By twisting the molecule about the internuclear axis, the δ-bond can be weakened to a point that the triplet state is thermally accessible (Figure I.9).[24] Gray and coworkers took advantage of this property and performed SQUID measurements on a rotamer of $Mo_2Cl_4(PMe_3)_4$.[25] Later, Cotton and coworkers undertook a more complete study that utilized temperature the dependence of the $^{31}P\{^1H\}$ NMR spectra.[26] Their study fully revealed the character and energetic disposition of the $^3\delta\delta^*$ state. As mentioned earlier, the $^1\delta\delta^*$ state was first investigated by Cowman and Gray.[17] The remaining state, $^1\delta^{*2}$,

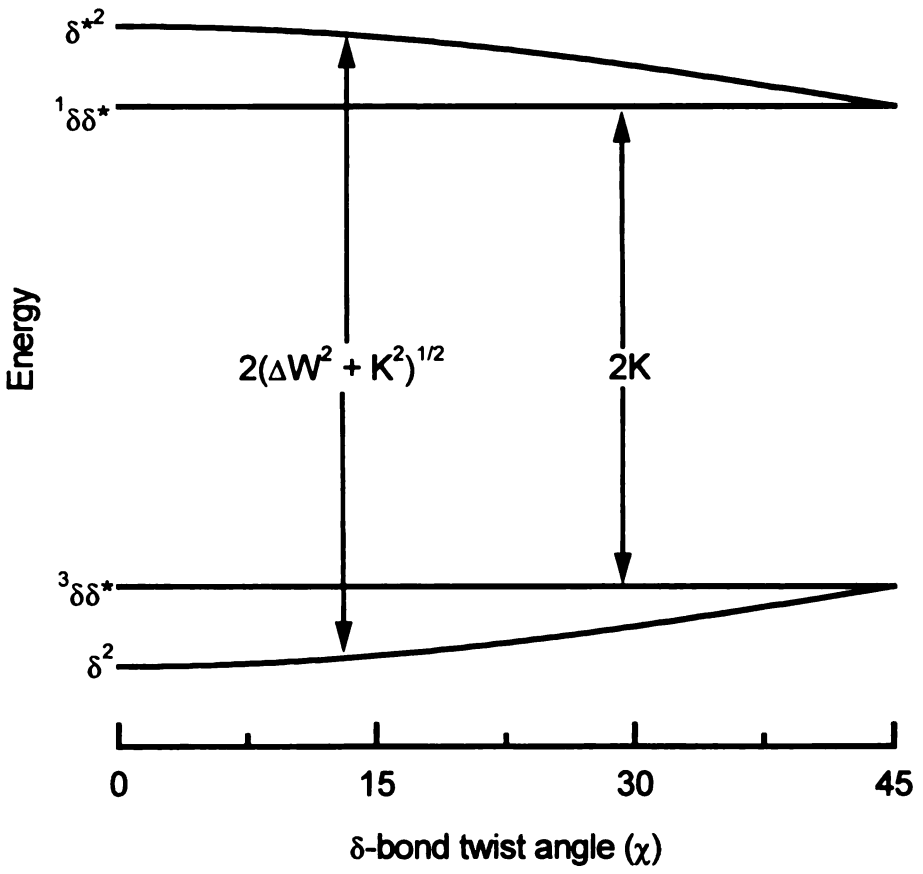

Figure I.9. The dependence of the electronic states of the δ-manifold on internuclear twist angle (χ). The δ-bond is broken at $\chi = 45°$. There is a mirror image of the manifold from 45° – 90° that is not shown here.

is the purview of this dissertation. Elucidation of this state and its properties will allow the first complete characterization of a two-center, two-electron bond.

Further inspection of the δ-manifold, however, reveals some challenges in finding the $^1\delta^{*2}$ state. First, the symmetry of the state is A_{1g}, the same as the ground state. Conventional spectroscopic selection rules dictate that g ↔ g transitions are forbidden. A second and perhaps more substantial difficulty arises due to the fact that the transition corresponds to moving two electrons from the δ bonding orbital to the δ* antibonding orbital. Two electron transitions are highly forbidden in conventional spectroscopy. Therefore, in order to access the $^1\delta^{*2}$ state then, it will be necessary to use an unconventional spectroscopic technique.

I.B. Nonlinear Spectroscopy

Nonlinear spectroscopy will be discussed by two approaches. The first will be largely phenomenological and consider the interaction of light and matter. The second will involve a more mathematical description of both linear and nonlinear spectroscopy.

I.B.1 Phenomenological Aspects of Spectroscopy[27]

A good place to begin this treatment of spectroscopy is to first consider the interplay between light and matter. If plane-polarized blue light is incident on a clear glass window, blue plane-polarized light is seen on the other side—apparently nothing has happened. However, if the window itself is considered, a great deal has happened.

The window is essentially a huge collection of nuclei and electrons where the Coulomb force holds the electrons to the nuclei. Together, the nuclei and electrons can be thought of as a collection of dipoles. The light is an oscillating electric and magnetic field that are orthogonal to one another. When the dipoles and electric field (the magnetic field is going to be ignored) are combined there is a substantial interaction. The electric field of the light causes the positively charged nuclei to move with the electric

field (though this motion is small due to the mass of the nuclei) and it causes the electrons to move against the electric field. Therefore, as the light passes through the window, it causes the dipoles to oscillate along with it. The light leaving the window therefore is significantly different than the light that was incident.

Once a dipole starts to oscillate the light that emanates from it can go in any direction. The electric field generated from a single dipole is shaped like a torus that expands at the speed of light (Figure I.10). No light, however, is seen to exit the sides of the window. This can be explained by Figure I.11, which shows a collection of three dipoles (looking along the dipole's axes). Dipole 1 (red) is the first to start oscillating, then 2 (green), and finally 3 (blue). Dipole 1's electric field will have the largest diameter by the time dipole 3 starts to oscillate. By superimposing all of the electric fields from each of the dipoles, it becomes apparent that the only constructive interference occurs in the forward (relative to the incident light) direction. When the electric fields constructively interfere, a new wavefront is produced known as the secondary wave. Since the dipoles are oscillating in phase with the primary wave (incident light), their velocity is also in phase. However, since radiation is only generated when an electron is accelerating (at the turning point of its oscillation) the secondary wavefront is 90 degrees out of phase relative to the primary wavefront. When the secondary and primary waves are superimposed, they yield the refracted wave. This is represented in Figure I.12. The cumulative phase lag (90 degrees due to the secondary wave, plus an amount linked to the intensities of primary and secondary waves) present in the refracted wave can be translated directly into a reduced velocity of the wavefront and this is observed as the refractive index of the material. If the clear window is replaced with an orange colored window, the blue light will not pass through. From the perspective of refractive index, absorption is the most extreme example of cumulative phase lag in the refracted wave; the light gets slowed down to a point where it no longer

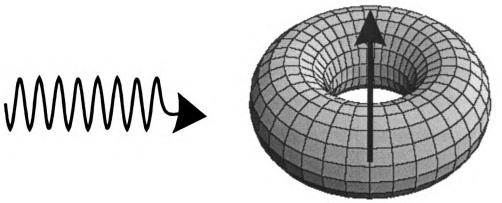

Figure I.10. The toroidal shaped electric field that is generated by an oscillating dipole.

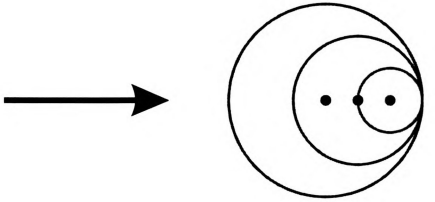

Figure I.11. View down the axes of three oscillating dipoles, along with the cross-section of their emanating electric fields are shown. Constructive interference of the electric fields only occurs in "forward" direction where the three electric fields overlap.

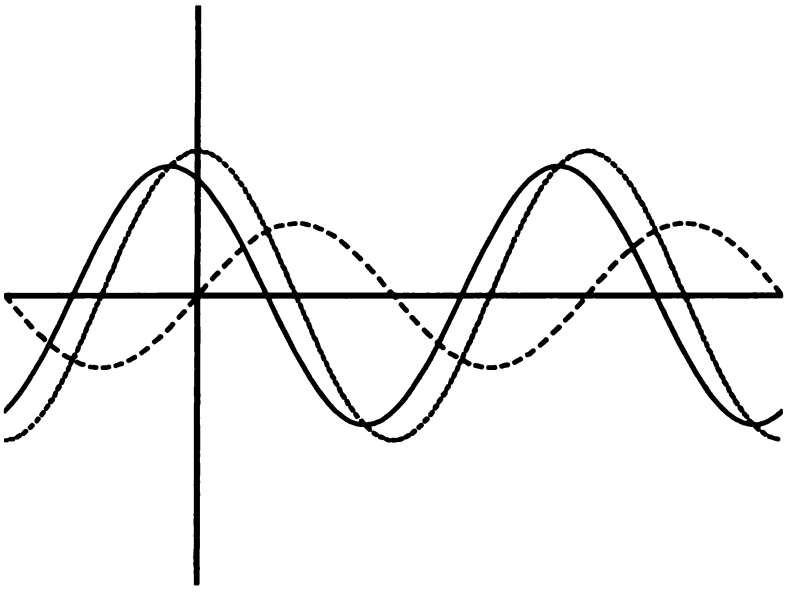

Figure I.12. The primary wave (•••) is at the frequency of the incident light. The secondary wave (- - -) that is generated when the oscillating dipoles are accelerating (at their turning points) is 90° out of phase with the primary wave. The refracted wave (—) is the superposition of the primary and secondary waves. Its phase relationship is determined by the 90° phase lag due to the secondary wave, plus a component related to the intensities of the primary and secondary waves.

moves forward at all. Quantum mechanically this corresponds to the orange glass having an allowed electronic transition that is at the same frequency as the incident blue light.

The preceding description is based largely on the classical physics description of a forced harmonic oscillator where the Coulomb force, which represents a spring, holds the electron to the nucleus. Not surprisingly, this harmonic oscillator view is somewhat flawed – it is assumed that no matter how intense the applied electric field, the electron will respond in a linear fashion. At some electric field intensity, however, the electron will be displaced far enough from the nucleus that it overcomes the Coulomb force that holds (~3×10^{10} V/m).[28] The harmonic oscillator model thus must be replaced with one that allows for anharmonic behavior. This is accomplished by allowing the dipole to become overdriven and oscillate at frequency multiples of the incident light. Therefore, in cases of very intense electric fields, two colors of light can be seen exiting the material (Figure I.13). If the material is not transparent to the new color of light, the new light will be absorbed.

1.B.2. Mathematical Aspects of Spectroscopy

The Beer-Lambert law represents a cornerstone in spectroscopy:[29]

$$I_f = I_0 e^{-\alpha bc} \qquad (I.2)$$

it relates the intensity of radiation transmitted by the sample (I_f) to the intensity incident upon the sample (I_0), where b and c are the sample thickness and concentration respectively and α is the absorption coefficient and is related to the extinction coefficient by:

$$\varepsilon = \frac{\alpha}{\ln 10} \qquad (I.3)$$

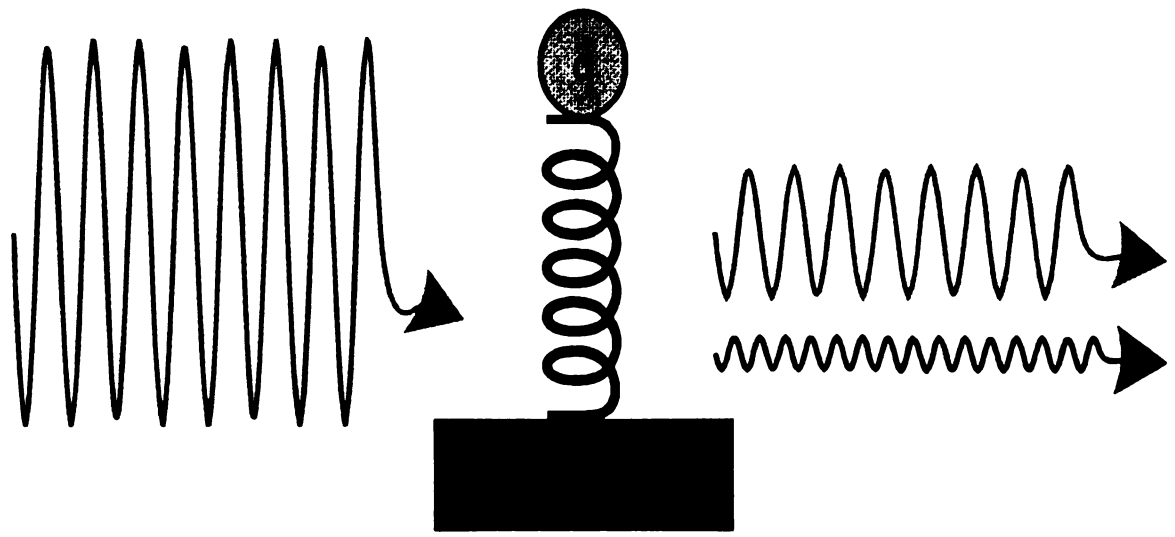

Figure I.13. When a dipole is exposed to a very high electric field, the dipole becomes overdriven and can oscillate at multiples of the driving frequency. Here, the dipole oscillates also at twice the driving frequency.

It is ε (or α) that carries the quantum mechanical information about the molecule being studied through the oscillator strength (f):

$$f = \frac{4m_e c\varepsilon_0 \ln 10}{N_A e^2}\int \varepsilon(\nu)d\nu = \frac{8\pi^2 m_e \nu}{3\ he^2}|\mu_{fi}|^2 \qquad (I.4)$$

where μ_{fi} is the transition dipole between the initial and final state (ψ_i and ψ_f):

$$\mu_{fi} = \int \psi_f^* \mu \psi_i \ ; \mu = e\mathbf{r} \qquad (I.5)$$

The preceding section demonstrated the importance of the refractive index. An expression can be derived that relates Beer's law to the refractive index.

The electric field of the radiation (E(z,t)) at a point far behind the sample (z>>b) is given by:[30]

$$E(z,t) = e^{\{i\omega(n-1)b/c\}}E_0 e^{\{-i\omega(t-z/c)\}} \qquad (I.6)$$

where z is the direction of propagation of the field, b is the sample thickness, c is the speed of light, and E_0 is the unperturbed electric field amplitude and ω is the angular frequency of the radiation ($\omega = 2\pi\nu$). The first term is often referred to as the phase factor and for n-1 < 1 is expanded to give the expression:

$$E(z,t) = [1 + i\omega(n-1)b/c + \ldots]E_0 e^{\{-i\omega(t-z/c)\}} \qquad (I.7)$$

Assuming as earlier that the material can be thought of as a collection of dipoles where the Coulomb force holds the electron to the nucleus. The oscillating electric field ($E_0 e^{-i\omega t}$) causes the dipole to behave as a forced harmonic oscillator. The equation of motion for the dipole in one dimension (x) is then:[30,31]

$$m\ddot{x} + \gamma\dot{x} + kx = E_0 e^{-i\omega t} \qquad (I.8)$$

where m is the mass of the electron, γ is the damping constant, and k is the restoring force ($k = m\omega_0^2$, ω_0 is the angular frequency of the oscillator). The trajectory of the electron x(t) is then:

$$x(t) = \frac{(q/m)E_0 e^{-i\omega t}}{\omega_0^2 - \omega^2 - i\omega c} \qquad (I.9)$$

All of the dipoles following this trajectory, then, reradiate electromagnetic energy at frequency ω and have a strong resonance (absorption) at $\omega = \omega_0$. The total field – which is the sum of unaffected electric field plus the field that is phase shifted – at some distance away from the sample is then:[30]

$$E(z,t) = E_0 e^{-i\omega(t-z/c)}\left(1 + \frac{bq^2 N\omega}{2\varepsilon_0 cm\left(\omega_0^2 - \omega^2 - i\omega\gamma\right)}\right) \qquad (I.10)$$

where N is the number of dipoles and ε_0 is the permitivity of free space. Equating this expression for the field with the one above (equation I.7) allows n to be determined:

$$n = 1 + A(\omega_0;\omega)\left(\omega_0^2 - \omega^2 + i\omega\gamma\right) \qquad (I.11)$$

where $A(\omega_0;\omega) = Nq^2/2\varepsilon_0 m[(\omega_0^2-\omega^2)^2 + \gamma^2\omega^2]$. This demonstrates that the refractive index is a complex number where the real and imaginary parts are given by:

$$Re(n) = 1 + A(\omega_0;\omega)(\omega_0^2 - \omega^2) \qquad (I.12a)$$

$$Im(n) = \gamma\omega A(\omega_0;\omega) \qquad (I.12b)$$

When this index of refraction is substituted into the phase shift term (equation I.7) and the resultant electric field is squared, the intensity at a point after the sample is given by:[32]

$$I(z) = \frac{E(z,t)^* E(z,t) c\varepsilon_0}{2} = I_f \qquad (I.13)$$

Using the same procedure, I_0 can be determined from E_0. I_f and I_0 can be combined to yield a different expression for Beer's law, that is dependent on the imaginary part of the refractive index:

$$I_f = I(z) = I_0 e^{-2\omega Im(n) b/c} \qquad (I.14)$$

Therefore, the refractive index serves two roles; the real part imparts a phase shift onto the incident beam, and the imaginary part serves to attenuate the beam.

A second way to look at refraction and absorption is through the relationship between the average dipole moment density (**P**) that is induced in the sample by the driving electromagnetic field (**E**):[33]

$$\mathbf{P}=\chi\mathbf{E} \tag{I.15}$$

The incident electric field is attenuated and phase shifted by χ, the susceptibility of the material. It has been shown that χ is related to the refractive index:

$$n^2=1+4\pi\chi \tag{I.16}$$

χ has both imaginary and real components just as the refractive index does, where the real part retards the phase of the incident electric field and the imaginary part attenuates the electric field. The real and imaginary components of χ in terms of the refractive index are:[30]

$$\mathrm{Re}(\chi)=\frac{\mathrm{Re}(n)^2-\mathrm{Im}(n)^2-1}{4\pi} \tag{I.17a}$$

$$\mathrm{Im}(\chi)=\frac{\mathrm{Re}(n)\mathrm{Im}(n)}{2\pi} \tag{I.17b}$$

This allows Beer's law to be written in terms of the susceptibility:

$$I_f = I_0 e^{-4\pi\,\mathrm{Im}(\chi)b/c\,\mathrm{Re}(n)} \tag{I.18}$$

To this point, the dipole has been assumed to behave linearly as a harmonic oscillator responding to a harmonic driving force. However, as the driving force becomes more intense, the dipole can no longer respond linearly (either the electron is ejected, or the oscillator becomes overdriven), this results in a nonlinear response as the dipole becomes anharmonic. The anharmonicity can be treated by expanding the susceptibility as a power series:

$$\mathbf{P}=\left(\chi^{(1)}+\chi^{(2)}\mathbf{E}+\chi^{(3)}\mathbf{E}^2+\ldots\right)\mathbf{E} \tag{I.19}$$

These higher order susceptibilities give rise to nonlinear responses to the driving force. These responses are well known in optics. Second harmonic generation, where two frequencies are mixed to form a third frequency that is the sum of the original two frequencies, arises from $\chi^{(2)}$ (Figure I.14a). Sum frequency generation and self-focusing are common examples where three frequencies are mixed through $\chi^{(3)}$ to generate a fourth frequency (Figure I.14b). Besides these optical effects, nonlinear responses to driving forces are also common in spectroscopy. Coherent anti-stokes Raman spectroscopy (CARS) and two-photon absorption spectroscopy are only two examples of four wave mixing through $\chi^{(3)}$ in spectroscopy (Figure I.15).

Two-photon spectroscopy has several characteristics that separate it from conventional, linear spectroscopy. The first is the difference in selection rules. With two-photon techniques it is possible to observe states that are forbidden to conventional spectroscopy.[34] The second characteristic is the quadratic dependence of the observed signal on the incident electric field.[34,35] The third characteristic, and perhaps the most useful, is the dependence of the two-photon transition probability on the polarization of the incident radiation.[36] Taking advantage of this characteristic allows for symmetry assignment of the excited states, depending on experimental arrangement.

I.B.2.a. Selection Rules

Orbital, vibronic, and spin selection rules govern the allowedness of a spectroscopic transition. The one most important to distinguish between one- and two-photon spectroscopy is the orbital or Laporte selection rule. The transition dipole, μ_{fi}, for a one-photon process is given by:[37]

$$\mu_{fi} = \langle \psi_f | \mu_j | \psi_i \rangle ; \mu = \mathbf{er} \qquad \text{(I.20)}$$

where ψ_f and ψ_i are wavefunctions representing the final and initial states respectively, and μ_j is the dipole moment in the j direction. From group theory, for a transition to have

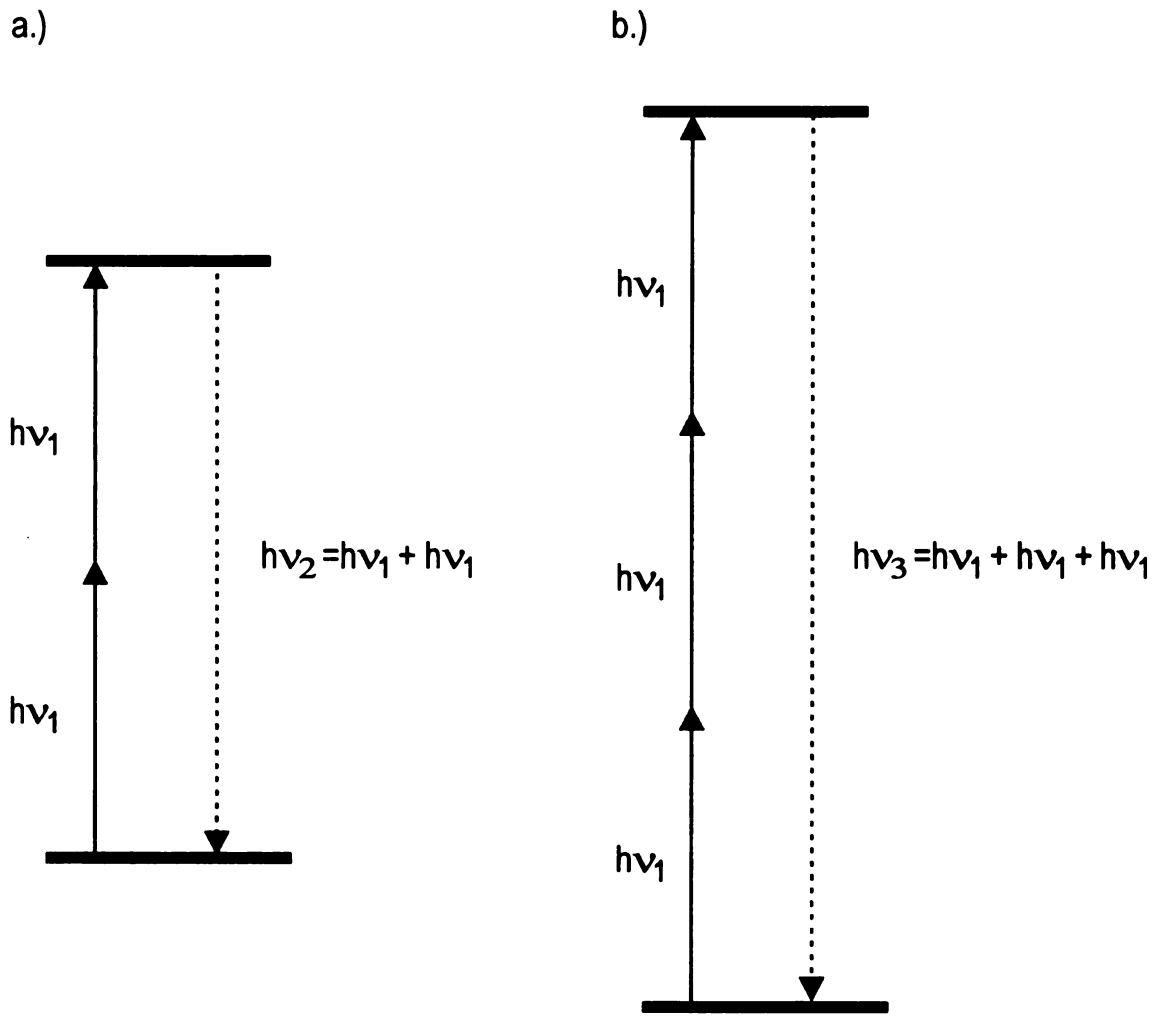

Figure I.14. a.) Second harmonic generation is an example where two frequencies ($h\nu_1$) are mixed through the second order susceptibility tensor, $\chi^{(2)}$, to yield a new frequency ($h\nu_2$), that is the sum of the incident frequencies. b.) In sum frequency generation, three frequencies ($h\nu_1$) are mixed through $\chi^{(2)}$ to yield a new frequency ($h\nu_3$) that is the sum of the three incident frequencies.

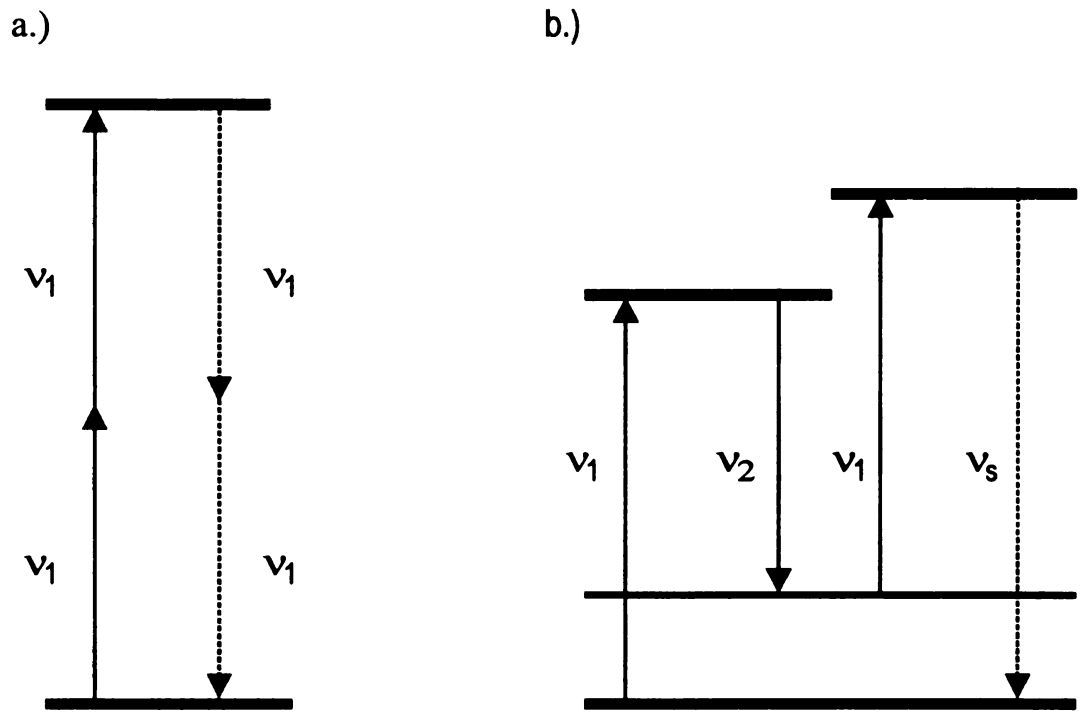

Figure I.15. Two examples of nonlinear spectroscopy where a total of four frequencies are mixed through $\chi^{(3)}$. a.) Two-photon absorption (TPA), where two photons (ν_1) populate the excited state that then relaxes to the ground state by two-photon emission. b.) Coherent anti-Stokes Raman spectroscopy (CARS) is a more complex process, where ν_1 places the system in a virtual state that is driven down to a vibrationally excited state by ν_2. This excited state interacts with a second photon ν_1 and ultimately the scattered photon at frequency ν_s is detected.

nonzero intensity, the product $\psi_f \mu_j \psi_i$ must be an even function (must include the totally symmetric irreducible representation). Since μ_j is an odd function that transforms as x, y, or z, the product of $\psi_f \psi_i$ must also be an odd function. This results in g $\leftrightarrow$ u transitions being allowed and g $\leftrightarrow$ g or u $\leftrightarrow$ u transitions being forbidden.

In two-photon spectroscopy, on the other hand, the allowedness of the transition is given by the two-photon transition tensor ,S:[35a]

$$S \propto \left\langle \psi_f \left| \mu_j^{(1)} \right| \psi_n \right\rangle \left\langle \psi_n \left| \mu_l^{(2)} \right| \psi_i \right\rangle \qquad \text{(I.21)}$$

where ψ_n is an intermediate state, and μ_j and μ_l indicate that the dipole moments involved in the transition are not necessarily the same. The effective two-photon operator is then $\mu_j \mu_l$. The product of the two dipole moment operators transforms as x^2, y^2, z^2, xy, xz, or yz, all of which are even functions. Therefore, g $\leftrightarrow$ g and u $\leftrightarrow$ u transitions are allowed in two-photon spectroscopy and g $\leftrightarrow$ u transitions are forbidden.

I.B.2.b. Power Dependence

In one-photon spectroscopy, there is a linear relationship between I_f and I_0 as stated by Beer's law. In two-photon spectroscopy, however, there is a nonlinear dependence on I_0. The probability for a two-photon transition can be determined from time-dependent perturbation theory.[35a] When both photons involved in the transition are from the same laser ($\omega_1 = \omega_2 = \omega_r$), the transition probability, $W^{(2)}$, is given by:

$$W^{(2)} \propto I_0^2 \left| \sum_n \frac{\left\langle \psi_f \left| \mu \right| \psi_n \right\rangle \left\langle \psi_n \left| \mu \right| \psi_i \right\rangle}{\Delta E_{ni} - \hbar \omega_r} \right|^2 \qquad \text{(I.22)}$$

where I_0 is the intensity of the incident laser beam, ψ_n is the virtual intermediate state and ψ_i and ψ_f are the initial and final states respectively. ΔE_{ni} is the energy of the virtual state and ω_r is the frequency of the incident radiation. This shows that the transition probability is proportional to the square of the intensity of the incident laser beam. In general, for any n-photon transition, the probability is proportional to I^n. The quadratic

dependence is a powerful tool to determine if an observed transition results from a two-photon absorption. Taking the logarithm of each side results in the more familiar expression:

$$\log W^{(2)} = 2\log I + \log C \qquad \text{(I.23)}$$

where the terms have the same meaning as before and C represents the terms in the summation above (Equation I.22) along with experimental variables.

I.B.2.c. Polarization Dependence

In one-photon spectroscopy the symmetry of an excited state can only be determined by using a rigidly oriented sample or working on a time-scale that is sufficiently fast to "freeze" molecular motion. In two-photon spectroscopy, however, the symmetry can be determined using a randomly oriented sample.[36,38] This attribute has made two-photon spectroscopy a valuable tool to spectroscopists.

In one-photon spectroscopy the absorption cross-section, σ, for randomly oriented molecules is related to the transition dipole (defined in Equation I.20):

$$\sigma \propto \left|\lambda \cdot \mu_{fi}\right|^2 \qquad \text{(I.24)}$$

where λ is the unit polarization vector of the absorbed photon. Since $\lambda \cdot \lambda^* = 1$ there is no polarization information contained in the observed transition.

In two-photon spectroscopy, however, the cross-section, $\langle\delta\rangle$ (more correctly, the absorptivity), is given by:[36]

$$\langle\delta\rangle = \left|\lambda \cdot \mathbf{S}_{fi}^{ab} \cdot \kappa\right|^2 \qquad \text{(I.25)}$$

where κ and λ are the polarization vectors of the two absorbed photons and $\mathbf{S}_{fi}^{ab}$, the two-photon transition tensor is:

$$\mathbf{S}_{fi}^{ab} = \sum_n \frac{\langle \psi_f^b | \mu | \psi_n^b \rangle \langle \psi_n^a | \mu | \psi_i^a \rangle}{\omega_{ni} - \omega_\kappa} + \frac{\langle \psi_f^a | \mu | \psi_n^a \rangle \langle \psi_n^b | \mu | \psi_i^b \rangle}{\omega_{ni} - \omega_\lambda} \qquad \text{(I.26)}$$

where ω_{ni} is the energy of the intermediate state and ω_j ($j = \kappa$ or λ) is the energy of the photon absorbed. The cross-section is most often written in terms of molecular parameters and polarization (experimental) parameters:

$$\langle\delta\rangle = \delta_F F + \delta_G G + \delta_H H \tag{I.27}$$

where, F, G, and H are functions of the polarization of the absorbed photons:

$$F = 4|\lambda\cdot\kappa|^2 - 1 - |\lambda\cdot\kappa^*|^2 \tag{I.28a}$$

$$G = -|\lambda\cdot\kappa|^2 + 4 - |\lambda\cdot\kappa^*|^2 \tag{I.28b}$$

$$H = -|\lambda\cdot\kappa|^2 - 1 + 4|\lambda\cdot\kappa^*|^2 \tag{I.28c}$$

and δ_F, δ_G and δ_H are functions of molecular parameters:

$$\delta_F \propto \sum_a \sum_b S_{fi}^{aa} S_{fi}^{bb*} \tag{I.29a}$$

$$\delta_G \propto \sum_a \sum_b S_{fi}^{ba} S_{fi}^{ba*} \tag{I.29b}$$

$$\delta_H \propto \sum_a \sum_b S_{fi}^{ba} S_{fi}^{ab*} \tag{I.29c}$$

where a and b represent the molecular axes and S_{fi}^{aa} are the two-photon transition tensors as before. If two photons of the same polarization are used then $\delta_G = \delta_H$ ($S^{ba} = S^{ab}$). Since δ_F is then the square of the trace of the tensor (which implies it is totally symmetric), it is nonzero only if the excited state is of the same symmetry as the ground state.

The values of F, G, and H have been calculated for the eight possible polarization cases (using circularly and linearly polarized light) and are shown in Table I.1. The tensor patterns have also been determined for most symmetries and the relevant patterns are shown in Table I.2 along with their polarization ratio, Ω, that is defined as:

$$\Omega = \frac{\langle\delta_{cir}\rangle}{\langle\delta_{lin}\rangle} \tag{I.30}$$

Table I.1. Values for the polarization functions F, G, and H, depending on the eight polarization cases. From References 34 and 36.

Case	1	2	3	4	5	6	7	8
	↑↑	↑→	↻↗	↻↺	↑↗	↑↺	↻↻	↻↺
F	2	-1	-1	-1/4	1/2	1/2	-2	3
G	2	4	4	7/2	3	3	3	3
H	2	-1	-1	-1/4	1/2	1/2	3	-2

Polarization Cases:

(1) Two linearly polarized photons with parallel polarization.

(2) Two linearly polarized photons with perpendicular polarization.

(3) One linear and one circular with the linear photon polarized such that it is perpendicular with the plane of the circularly polarized photon.

(4) Both circular with propagation opposite to each other.

(5) Both linear, with 45° between their polarization vectors.

(6) One linear and one circular with the linear photon polarized such that it is parallel with the plane of the circularly polarized photon.

(7) Two circularly polarized with polarization in the same sense.

(8) Two circularly polarized with polarization in the opposite sense.

Table I.2. Two-photon tensor patterns and the polarization ratio expected for each transition in the D_{2d} point group. From References 34, 36, and 38.

Tensor Pattern operator	Transition Symmetry (gs ↔ es)†	Polarization Ratio Ω
A_1: $x^2 + y^2, z^2$ $\begin{pmatrix} s_1 & 0 & 0 \\ 0 & s_1 & 0 \\ 0 & 0 & s_2 \end{pmatrix}$	$A_1 \leftrightarrow A_1$; $A_2 \leftrightarrow A_2$; $B_1 \leftrightarrow B_1$; $B_2 \leftrightarrow B_2$	$\Omega < 1$
B_1: $x^2 - y^2$ $\begin{pmatrix} s_3 & 0 & 0 \\ 0 & -s_3 & 0 \\ 0 & 0 & 0 \end{pmatrix}$	$A_1 \leftrightarrow B_1$ $A_2 \leftrightarrow B_2$	$\Omega = 3/2$
B_2: xy $\begin{pmatrix} 0 & s_4 & 0 \\ -s_4 & 0 & 0 \\ 0 & 0 & 0 \end{pmatrix}$	$A_1 \leftrightarrow B_2$ $A_2 \leftrightarrow B_1$	$\Omega = 3/2$
E: xz, yz $\begin{pmatrix} 0 & 0 & s_5 \\ 0 & 0 & -is_5 \\ s_6 & -is_6 & 0 \end{pmatrix}$ and $\begin{pmatrix} 0 & 0 & s_5^* \\ 0 & 0 & -is_5^* \\ s_6^* & -is_6^* & 0 \end{pmatrix}$	$A_1 \leftrightarrow E$ $E \leftrightarrow E$	$\Omega = 3/2$

† gs = ground state symmetry; es = excited state symmetry.

where $\langle\delta_{cir}\rangle$ and $\langle\delta_{lin}\rangle$ are the cross sections for using two circularly and two linearly polarized photons respectively and are given by:

$$\langle\delta_{cir}\rangle = F\delta_F + (G+H)\delta_G = -2\delta_F + 6\delta_G \qquad \text{(I.31a)}$$

$$\langle\delta_{lin}\rangle = F\delta_F + (G+H)\delta_G = +2\delta_F + 4\delta_G \qquad \text{(I.31b)}$$

The polarization ratio is bounded by:

$$0 \le \Omega \le \frac{3}{2} \qquad \text{(I.32)}$$

Therefore, by measuring the intensity of the transition when two circularly polarized photons are used and comparing that to the intensity when two linearly polarized photons are used, the symmetry of the states involved in the transition can be determined. As indicated in Table I.2, when two circularly and two linearly polarized photons are used $\Omega < 1$ only occurs when the symmetry of the initial and final states is the same.

Chapter II

Experimental Methods

There are two general classes of quadruply bonded compounds that have been studied. The first to be reported have the general formula $M_2X_4L_4$ (1) (where $M_2 = Mo_2$, W_2 or MoW; X = Cl, Br, or I; and L = uncharged σ donor ligand). The second class has the general formula $Mo_2Cl_4(\overset{\frown}{P}\overset{\frown}{P})_2$ (2) where $\overset{\frown}{P}\overset{\frown}{P}$ indicates a bridging diphosphine ligand that induces a twist about the internuclear axis.

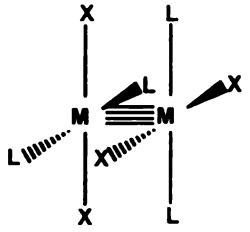

(1)

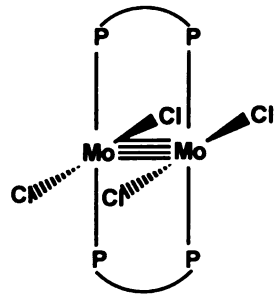

(2)

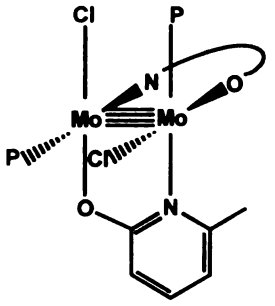

(3)

II.A. Materials and Standard Instrumentation

Compounds with the general formula $M_2X_4L_4$ were prepared by a number of colleagues using literature methods. Dr. Carolyn Hsu provided ample quantities of $Mo_2Cl_4(PMe_3)_4$[39] while Dr. Sara Helvoigt provided the Br,[40] I,[40] W_2[41] and MoW[42] derivatives that completed the series. Several unsuccessful attempts were made by Dr. Ann McIntosh to synthesize the F analogue.[43] Dr. McIntosh did, however, make available the low symmetry (C_2) compound *cis*-$Mo_2Cl_2(mhp)_2(PMe_2Ph)_2$ **(3)** (where mhp = 6-methyl-2-hydroxypyridine) that was very important in the earliest days of two-photon investigations on quadruply bonded complexes.[44]

Dr. Sara Helvoigt prepared the twisted compound $Mo_2Cl_4(dmpm)_2$ (dmpm = bis(dimethylphosphino)methane).[45] The other twisted compounds studied $Mo_2Cl_4(depe)_2$, (depe = bis(diethylphosphino)ethane), $Mo_2Cl_4(S,S\text{-}dppb)_2$ (S,S-dppb = (2S,3S)-bis(diphenylphosphino)butane), and $Mo_2Cl_4(dppe)_2$ (dppe = bis(diphenylphosphino)ethane) were prepared as outlined below. The twist angle of these compounds is listed in Table II.1

Table II.1. The twist angle (χ) for each of the compounds studied. The ligand abbreviations are given in the text. $Mo_2Cl_4(PMe_3)_4$ corresponds to a 90° twist. Values taken from Reference 26b.

Compound	Twist Angle (χ)
$Mo_2Cl_4(dmpm)_2$	0
$Mo_2Cl_4(S,S\text{-}dppb)_2$	24.7
$Mo_2Cl_4(depe)_2$	41.4
$Mo_2Cl_4(dppe)_2$	59.5
$Mo_2Cl_4(PMe_3)_4$	90

II.A.1. Synthesis of $Mo_2Cl_4(\overset{\frown}{P\,P})_2$ compounds

All manipulations were carried out under an argon atmosphere provided by a Schlenk line. The pertinent bridging phosphine ligands were purchased from Strem Chemical and used as received. The $K_4Mo_2Cl_8$ starting material had been previously prepared by other group members using the literature method.[46] The solvents used in synthesis were dried by standard techniques and freshly distilled prior to their use. No attempts were made to quantitate the yields of any of the syntheses. All NMR spectra were collected with the sample dissolved in CD_2Cl_2 and UV/visible spectra with the sample dissolved in CH_2Cl_2.

II.A.1.a. Synthesis of Mo_2Cl_4(S,S-dppb)$_2$[47]

$K_4Mo_2Cl_8$ (85 mg) and S,S-dppb (120 mg) were placed in a 50 ml three-necked round bottom flask that possessed a magnetic stirring bar. A reflux condenser was placed on the flask and the two remaining necks were capped, one with a ground glass stopper, the other with a septum. The apparatus was connected to a Schlenk line and repeatedly evacuated and filled with dry argon. Freshly distilled methanol (~10 ml) was added by syringe through the septum which was then replaced with a ground glass stopper. The apparatus was then heated in an oil bath to reflux and was allowed to reflux for eight hours. During the course of the reflux, the solution turned from red to yellow-green with a yellow-green precipitate. The methanol was removed by vacuum and the yellow-green powder left behind was washed several times with methanol. After several rinses, diethyl ether was used to thoroughly dry the compound. The NMR spectrum of this material indicated that there was no unreacted phosphine. Due to the sample's significant triplet character, the NMR spectrum was too broad to be interpreted. The UV/visible spectrum had a $^1(\delta \rightarrow \delta^*)$ transition consistent with that reported in the literature.[47]

II.A.1.b. Synthesis of $Mo_2Cl_4(depe)_2$[48]

$K_4Mo_2Cl_8$ (100 mg) was placed in a three-necked round bottom flask that contained a stirring bar and was equipped with a reflux condenser, septum, and ground glass stopper. Freshly distilled degassed methanol (~10 ml) was added by syringe through the septum which was then removed and replaced with an addition funnel. The addition funnel contained a 0.7 M solution of depe in toluene (1 ml). The depe solution was added to the reaction mixture and the addition funnel was replaced with a ground glass stopper. The solution was heated to reflux and changed from a red to red-brown color. After 6 hours of reflux, the solution was allowed to cool and the red-brown solid was removed by filtration. The product was washed first with water and then methanol. An NMR spectrum was taken, but like the dppb derivative it was too broad to reveal anything except that there was no unreacted phosphine in the mixture. The UV/vis spectrum had a $^1(\delta \rightarrow \delta^*)$ transition that was consistent with the literature.[48]

II.A.1.c. Synthesis of $Mo_2Cl_4(dppe)_2$[49]

The preparation of the dppe derivative was modified from the literature as suggested by Dr. Sara Helvoigt. Rather than starting with $Mo_2(O_2CCF_3)$ and adding Cl^- with Me_3SiCl, $K_4Mo_2Cl_8$ was used as the starting material and the same preparation procedure described for the depe compound was followed. The solution turned from red to green to muddy-orange on reflux. According to the literature, the green stage corresponds to the α-isomer of this compound.[49] The solution refluxed for 12 hours to drive it as fully as possible to the β-isomer. The light-brown product was washed with water and methanol; its UV/visible spectrum was consistent with the literature.[49]

II.A.2. Spectroscopic Solvents and Materials

All spectra, unless otherwise noted were measured for samples dissolved in Gold Label 3-methylpentane(3-MP) purchased from Aldrich Chemicals. 3-MP was first dried over activated 4Å molecular sieves, then transferred *via* a high-vacuum manifold to a high-vacuum pot containing sodium-potassium (NaK) alloy. The pot was sealed from the atmosphere by a Kontes high-vacuum stopcock. The samples were placed in a slightly modified high-vacuum cell.[50] The modification consisted of having the cell attached to manifold in such a way that it could be easily cut off in the glass shop. The cells had to be removed from their manifolds so they could be loaded in an Air Products (Air Products and Chemicals, Allentown, PA) crysostat to perform the two-photon measurements. The crysostat was used to cool the samples to 60 – 120 K, depending on the solvent and excitation wavelength. Cooling the samples resulted in a significantly increased quantum yield as compared to room temperature. The low-temperature quantum yields were not measured, but it was readily apparent to the eye that the quantum yield increased. Also, with all samples other than $Mo_2Cl_4(PMe_3)_4$, the emissive lifetime of the $\delta\delta^*$ state increased significantly when the sample was cooled. This increase in lifetime also made it easier to detect the fluorescence. To maintain good thermal contact with crysostat cell holder, the cells were wrapped in indium foil. Once the cells were in place, the indium foil was cut away from the area of the cell where the laser beam would pass through. It must be noted that all cells and optics were either Pyrex or BK7 optical glass. Quartz was originally used; however, small amounts of crystallinity remained even after the fusing process, which resulted in the optics and cells producing very small amounts of doubled laser light. This frequency doubled light often-times corresponded with allowed one-photon transitions and led to spurious data.

II.A.3. Standard Instrumentation.

The absorption spectra were recorded using either a Cary-17D spectrometer that was retrofitted by OLIS to provide computerized data collection or a Perkin Elmer 3840 Diode Array UV/visible spectrometer. Emission spectra were recorded on a spectrometer that was constructed at Michigan State University and recently modified to include digitized fluorescence detection by means of a Stanford Research Systems SR 400 photon counter.[51] $^{31}P\{^{1}H\}$ NMR spectra were recorded on a Varian Inova-300 MHz spectrometer.

II.B. Two-Photon Fluorescence Excitation (TPE)

As indicated in Chapter I, two-photon spectroscopy is a very powerful tool. However, as with most techniques, there are significant drawbacks. Perhaps the most substantial weakness of TPE is its poor sensitivity owing to the extremely low cross-sections ($\sim 10^{-50}$ $cm^4 s^{-1} molecule^{-1}$) that are encountered. The selection of a very sensitive detection scheme can improve the sensitivity. Several schemes are available that provide for detection against a so-called "dark" background. The one used in this study was fluorescence excitation.

II.B.1. TPE Instrumentation

The instrumentation used in the two-photon investigation of quadruply bonded compounds has evolved substantially over time. The first version has been reported previously in the literature.[52] The most current version of the instrument (Figure II.1) will be described here.

In order to obtain the high photon flux necessary to access two-photon states it is necessary to use a pulsed laser. The heart of the instrument is a Coherent Infinity 40-100 Nd:YAG laser (Coherent Laser Group, Santa Clara, CA). The fundamental wavelength of the laser is 1064 nm, emanated with a pulse width of approximately 3.5 ns. The pulse

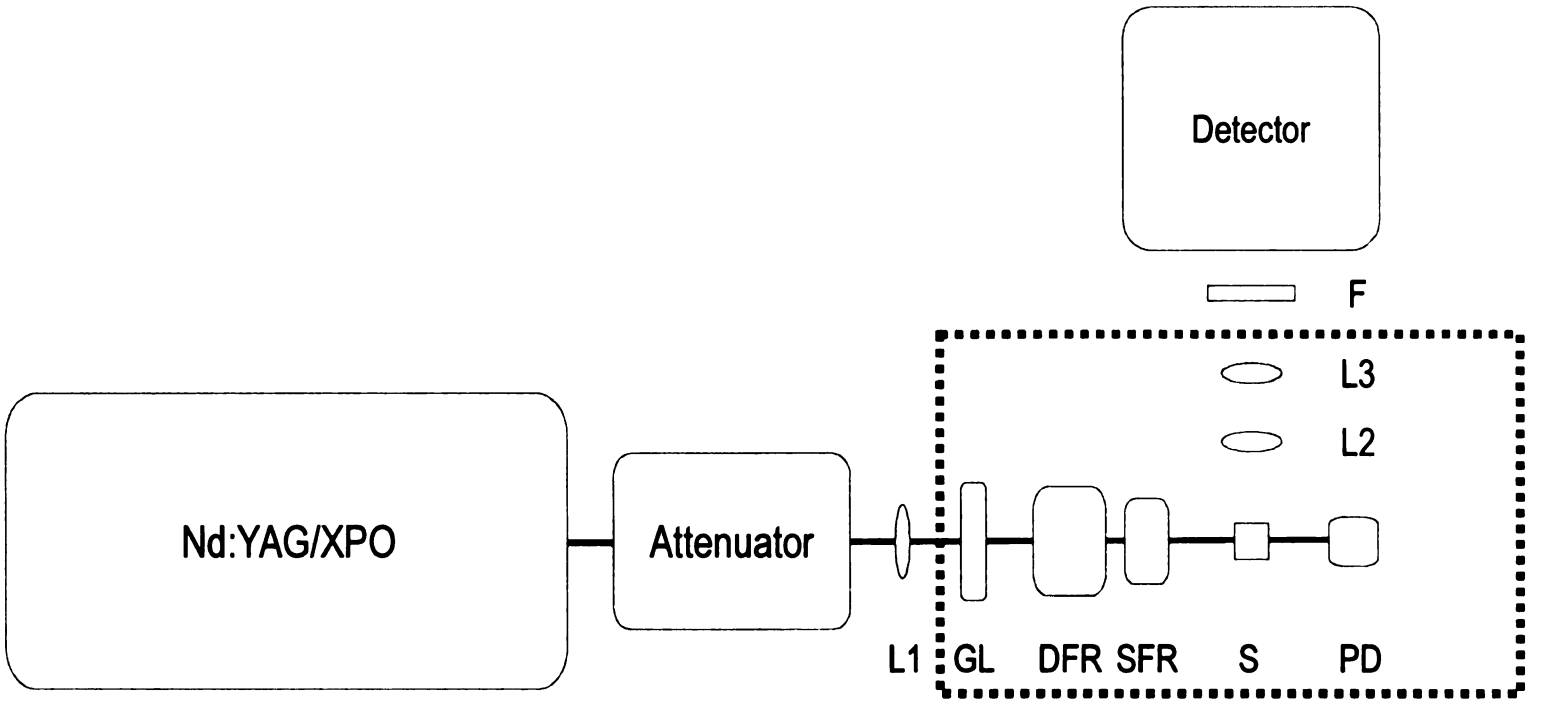

Figure II.1. A schematic drawing of the instrumentation used to perform TPE measurements. L1 is the long focal length lens used to reduce divergence of the laser beam. GL (Glan-Laser polarizer) DFR (Double Fresnel Rhomb), and SFR (Single Fresnel Rhomb) are the optics used to adjust the polarization state of the laser beam. S is the sample that is housed in a cryostat and PD is the pyroelectric photodetector. L2 and L3 are F/4 collection optics to couple the sample fluorescence to the detector after passing through an appropriate filter (F). The detector used depended on the molecule being studied as indicated in the text. The (·····) box represents the sample chamber.

energy can be varied from a few mJ/pulse up to 600 mJ/pulse and the repetition rate can be adjusted from single-shot mode up to 100 Hz. The fundamental frequency can be doubled (532 nm) and tripled (354.7 nm) using crystals supplied by Coherent. The efficiency of doubling and tripling are 50% and 40%, respectively, of the incident fundamental pulse energy. The three frequencies that are provided by the Nd:YAG laser and its harmonics do not provide the tunability that is necessary to fully study the two-photon spectroscopy of quadruply bonded dimers.

The tunability is accomplished by a Type I XPO that is also supplied by Coherent. The XPO is an optical parametric oscillator (OPO). An OPO provides broad tunability (420 – 710 nm signal frequencies, 710 nm – 2300 nm idler frequencies). The broad tunability arises from the nonlinear optical parametric process. The optical parametric process is essentially sum frequency generation (SFG) (refer to Figure 1.14b) in reverse. One high energy pump photon (354.7 nm) is split into a visible (signal frequency) and red/near-infrared (idler frequency) photon such that the energy constraint (Equation 2.1) is met:[53]

$$E_{pump} = E_{signal} + E_{idler} \qquad (2.1)$$

The optical parametric material in the XPO is β-BaB_2O_4 (β-barium borate (BBO)). The signal and idler wavelengths are tuned by adjusting the angle of the crystal as shown in Figure II.2. Since both the signal and idler wavelengths are generated at the same time it is necessary to use the appropriate optics in the XPO cavity to make the cavity resonant in either the signal or idler frequency. If both are resonant, the energy density within the cavity can get too high and lead to optical damage. For all of the experiments reported here, the XPO was operated in the idler resonant mode. Some residual signal energy is present with the idler beam and this is removed by passing the XPO output beam through a Schott RG715 long-wave pass filter (also supplied by Coherent). The XPO is not seeded; therefore, the bandwidth of the output is wavelength

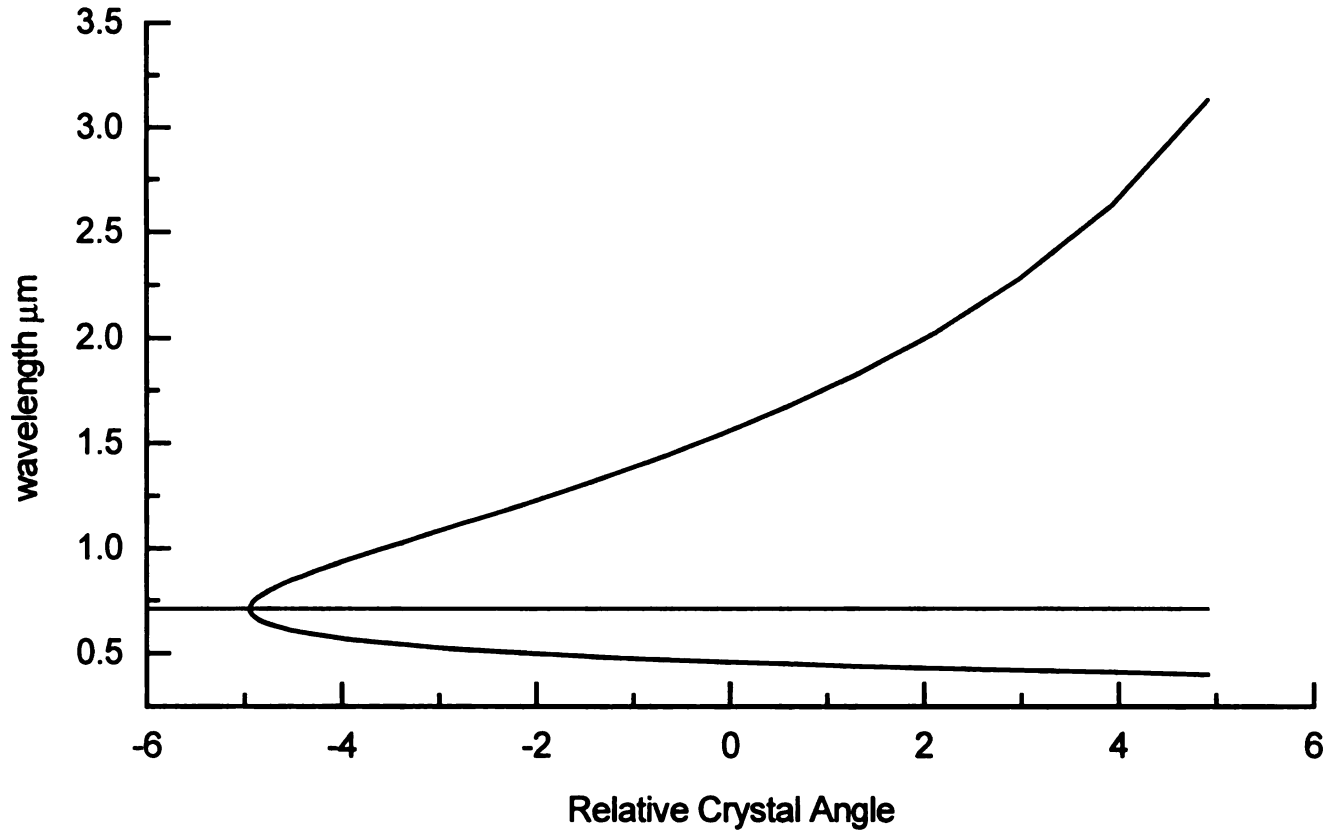

Figure II.2. The dependence of idler and signal wavelengths on the BBO crystal angle. When the pump beam is normal to the crystal, the angle is 0°. The line is drawn at 710 nm which represents the degeneracy point, where the signal and idler wavelengths are the same.

dependent as shown in Figure II.3. In terms of idler wavelengths, the bandwidth varies the most from 710-1200 nm. This was a concern, so an earlier experiment that used a constant bandwidth (~0.3 cm^{-1}) source was repeated. The result is shown in Figure II.4. There is a slight difference on the blue edge of the spectra; however the difference is inconsequential since it does not affect the maximum of the transition.

In order to maintain the most consistent operation of the XPO it was necessary to pump it at constant repetition rate and pulse energy (100 Hz and 170 mJ/pulse at 354.7 nm). While the high repetition rate was useful for shortened acquisition times and signal-to-noise ratio concerns, the constant pump energy precluded doing measurements to investigate the dependency of emission intensity on incident laser power. To circumvent this limitation, a Newport (Newport Corporation, Irvine, CA) 935-10 High Energy Laser Attenuator was used. This optic uses a series of quartz wedges to attenuate the beam. The angle of the wedges is adjusted by means of a lead screw. Changing the angle changes the amount of Fresnel reflection. The wedges are arranged so they rotate in opposite directions thus minimizing beam walk. The use of this optic made it possible to attenuate the intensity by as much as 27 dB with minimal walk.

After leaving the attenuator, the beam is passed through a long focal length (500 mm or 1000mm) lens to reduce its divergence. The polarization of the laser beam is manipulated to be either circularly or linearly polarized by three optics. These optics are a CVI (CVI Laser Corporation, Albuquerque, NM) CLPA-10.0-670-1064 Glan-Laser polarizer (GL), a Newport PR-950 double Fresnel rhomb (DFR) and a CVI FR-4-C single Fresnel rhomb (SFR). The GL is used to ensure constant horizontal polarization of the laser beam before it reaches the next two optics. The DFR is placed in a rotatable mount that can be rotated about the optical axis of the laser beam. When the DFR is rotated, the plane of polarization of the laser beam is rotated with respect to the incoming laser beam. This results in changing the plane of polarization of the laser beam with respect to the optical axis of the SFR. The SFR produces either circularly polarized or linearly

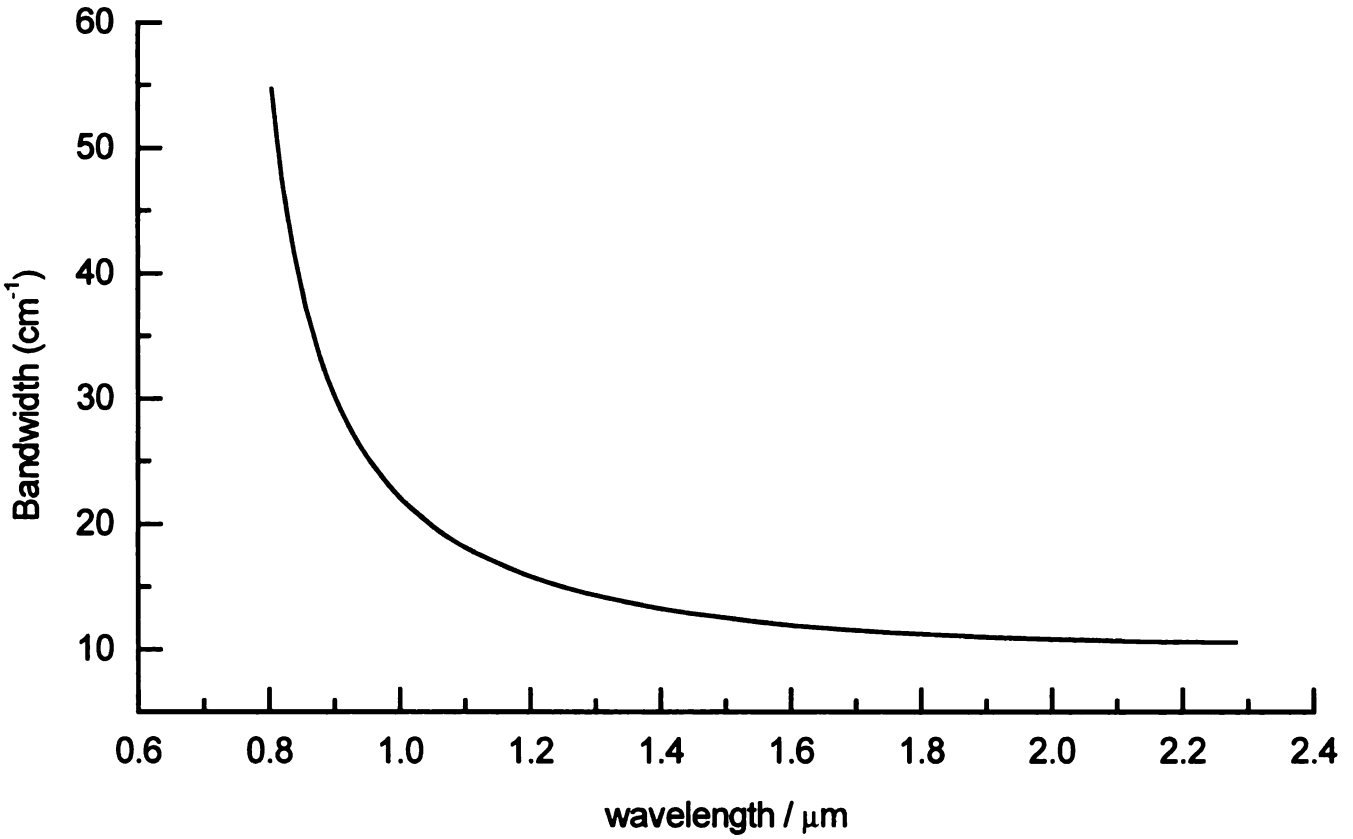

Figure II.3. The variation of bandwidth with idler wavelength. Only the range from 800 – 2300 nm is shown. The bandwidth continues to rise to the blue, maximizing at ~1000 cm^{-1} at 710 nm.

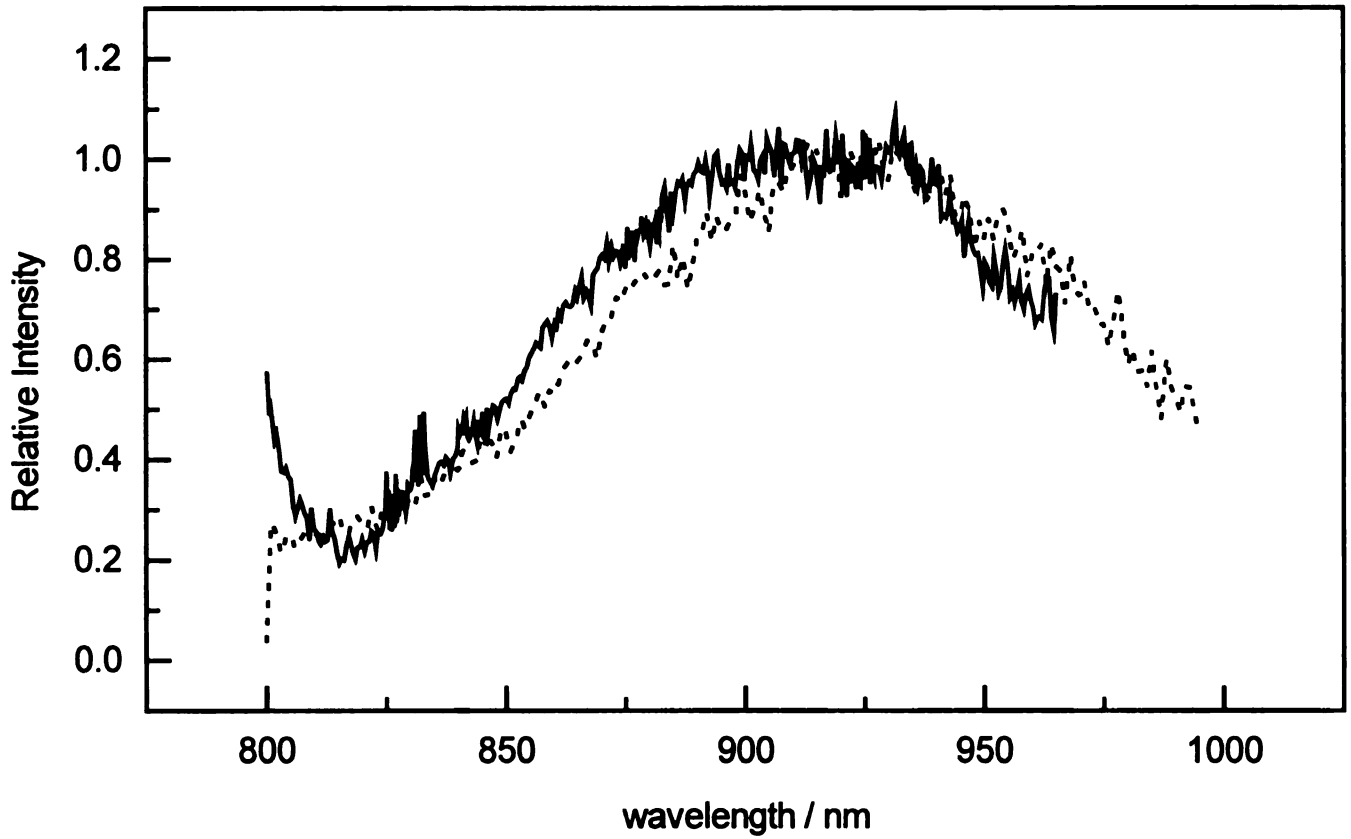

Figure II.4. Comparison of the TPE spectrum taken with a (—)constant bandwidth (~0.3cm^{-1}) source and the (•••) Type I XPO.

polarized light, depending on the plane of polarization of the incident laser beam. This is accomplished by variably retarding either the magnetic field or electric field of the laser beam. The degree of retardation is dependent upon the plane of polarization of light incident upon the SFR.

The polarization state of the laser beam is experimentally determined as shown in Figure II.5. By placing a mirror in the beam path and rotating the DFR, a minimum is observed in the reflected laser (using an IR viewer (Find-R-Scope, FJW Optical Systems, Inc., Palatine IL)) beam when the light is circularly polarized. Linearly polarized light is determined by placing a Glan-Thompson (GT) polarizer in the beam path. By rotating the DFR, a minimum is observed after the GT when the light is linearly polarized.

The laser beam then passes through the sample and onto a Molectron (Molectron, Portland, OR) J8LP photodetector. This thermopile detector has an essentially constant wavelength response from 200 nm to 10 μm (± 2%). Because of the constant response, no attempt was made to correct for slight variations. The photodetector was connected to a 1MΩ impedance signal input of a Stanford Research Systems (Stanford Research Systems, Sunnyvale, CA) SR250 Gated Integrator/Boxcar Averager Module.

The fluorescence that is generated when the sample absorbs two near infrared photons is detected in one of two ways, depending on the sample's emission wavelength. For compounds with the general formula $M_2X_4L_4$ and $Mo_2Cl_4(dmpm)_2$ the emission is centered in the red area of the spectrum. For these compounds, the emission was dispersed by a SPEX (Instruments S. A. Inc., Edison, NJ) 1681 monochromator and detected by a Hamamatsu (Hamamatsu Corporation, Bridgewater, NJ) R943-02 photomultiplier tube (PMT) that was operated at 2200 V while being cooled in a Products for Research (Products for Research, Danvers, MA) TE-104 thermoelectrically cooled PMT housing. The output current of the PMT was fed into the 50 Ω load of a Stanford Research Systems SR400 Gated Photon Counter. The photon counting technique provided a substantially improved signal-to-noise ratio over the previously used boxcar

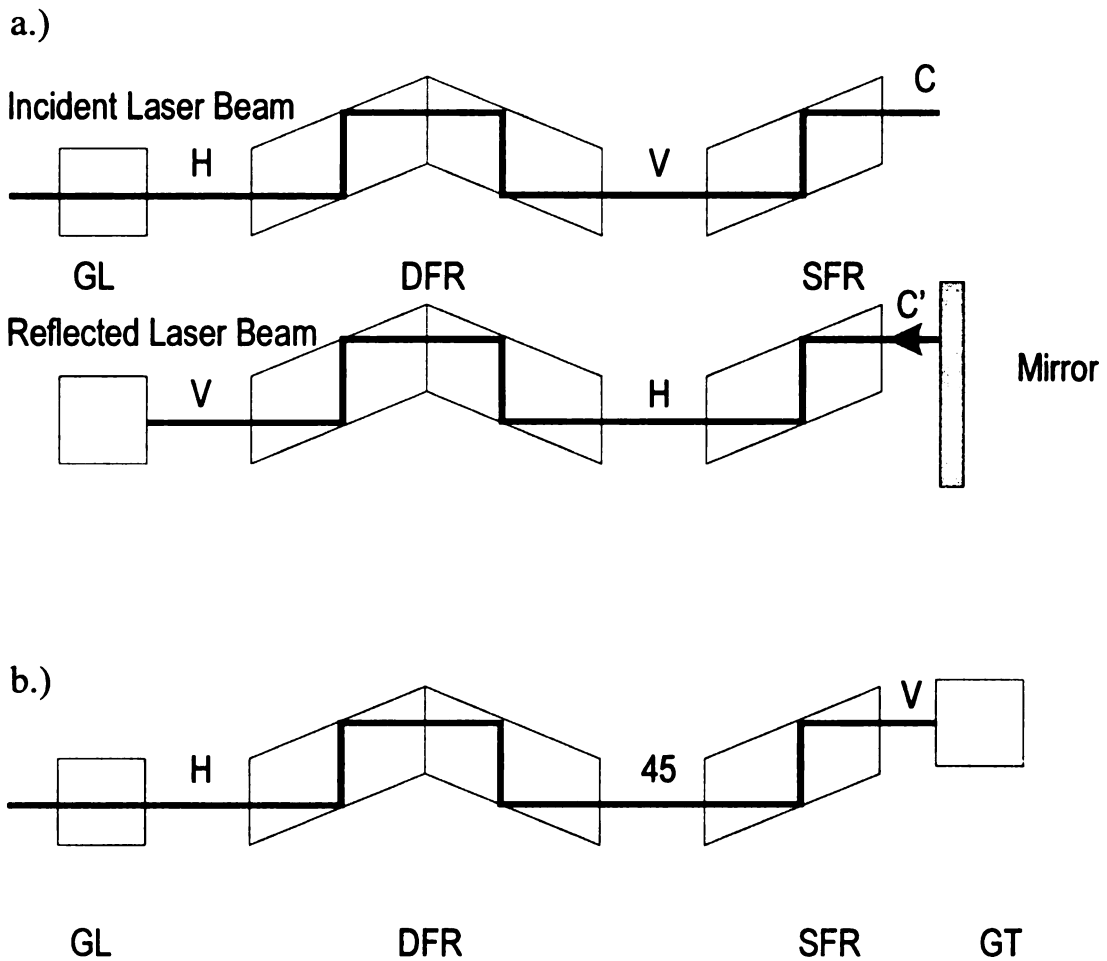

Figure II.5. The polarization state of the laser beam is experimentally determined as shown here. Determination of circularly polarized light is shown in a.). The horizontally polarized laser beam (H) passes through the Glan-laser polarizer (GL) and its polarization is rotated by 90° to be vertically polarized (V) by the double Fresnel rhomb (DFR). The vertically polarized light is converted to be circularly polarized (C) by the single Fresnel rhomb (SFR). The laser beam is reflected by a mirror (M), where the handedness of the circular polarization is changed (C'). The polarization is ultimately changed to vertical after passing through the SFR and DFR a second time. The vertically polarized light does not pass through the GL. Vertically polarized light is determined by b.). The mirror is replaced by a Glan-Thompson polarizer (GT) arranged to block vertically polarized light and the DFR is rotated until no laser light is seen to pass through the GT.

averager method.[52] The discriminator level of the photon counter was adjusted to minimize the number of spurious photons detected that were the result of thermionic emission from the various dynode stages of the PMT. The discriminator level was usually set to -40 mV. The gate width was determined by measuring the fluorescence lifetime (τ) of the sample. Usually the gate width was set to 5τ.

For the twisted compounds, $Mo_2Cl_4(\overset{\frown}{P\,P})_2$, with the exception of $Mo_2Cl_4(dmpm)_2$, the emission was too far in the near infrared to be detected by the R943-02 PMT. Therefore, a CCD detector was used instead. The emission was dispersed by a SPEX 270M spectrograph and a SPEX SpectrumOne CCD detector measured the fluorescence. This arrangement was not used for all of the compounds for several reasons. Since a CCD can not be gated and maintain its near infra-red sensitivity, there was no way to time resolve the emission. Thus, the CCD was collecting light for a continuous period of several minutes (even though the samples were emitting for only about 1 millisecond total when the laser was operated at 100 Hz) whereas the photon counter can operate only when the sample was emitting light. This gave rise to a substantial CCD background spectrum even when the sample was enclosed in a light tight compartment and the room lights were off. Also, a benefit of the lack of sensitivity in the near infrared by the PMT was advantageous in terms of reducing the amount of scattered laser light detected by the PMT. Due to the CCD's sensitivity in the near infrared, even a small amount of scattered laser light in the 800-1100 nm range could saturate the detector. With the twisted compounds, the laser excitation was much further into the NIR (1150-1600 nm) where the CCD is not sensitive to scattered laser light.

II.B.1.a. TPE Measurment

Regardless of the detection method that was used, the laser and detector were interfaced using LabView. For both detection schemes, the Molectron detector that was fed into the Stanford Research Systems SR250 Boxcar Averager was used to measure the

relative laser intensity. LabView then communicated with the boxcar via the SR245 computer interface module with GPIB commands. When the PMT/photon counter detection scheme was used, the communication was also performed using GPIB commands between LabView and the SR400. For the CCD detection scheme, LabView virtual instrument drivers provided by SPEX were used to gain low-level access to the CCD detector. LabView communicated with the XPO using dynamic data exchange (DDE) to facilitate tuning the laser.

The data collection was routine. The maximum of the $\delta^2 \rightarrow \delta^{*2}$ transition was estimated based on the maximum of the $^1(\delta \rightarrow \delta^*)$ transition. The laser was tuned to this wavelength and the fluorescence was detected accordingly. When the PMT/photon counter was used to detect the fluorescence it was desirable to attain approximately 400 counts/100 laser shots; too high a count rate oftentimes resulted in saturation of the PMT for the first several nanoseconds after the laser pulse. Since the photon counter literally counts pulses, it would only count once for the saturation, despite the fact that the saturation was actually due to several photons striking the photocathode at nearly the same time. The slits on the monochromator were adjusted to yield the desired signal level. When the CCD detected the fluorescence, the CCD integration time was adjusted such that the signal after the background spectrum was subtracted had at its maximum 600 counts. Once the detection parameters were determined, LabView was launched and it took over data acquisition. The laser was tuned to its starting frequency and if the CCD was being used, LabView would prompt for a beam stop to be placed in the beam for acquisition of a background spectrum. If the PMT/photon counter was being used, it was not necessary to take a background due to the phase-sensitive nature of the gated detection and low dark current of the PMT used. The next step involved determining the fluorescence intensity and laser intensity. Once this was done LabView would determine the signal by dividing the fluorescence intensity by the square of the laser intensity and

then advance to the next wavelength. This would be repeated until the full spectral region of interest was covered.

II.B.1.b. Power Dependence Measurement

As indicated in Section I.B.2.b, the signal intensity of a two-photon transition is proportional to the square of the incident laser intensity. Measurement of this dependence provides a useful check to be certain that the data being gathered are in fact due to a two-photon process.

The power dependence measurements were also straightforward. LabView was again utilized to gather the data. The laser was tuned to the desired wavelength and the fluorescence intensity and relative laser intensity were measured. LabView would then prompt to adjust the laser energy using the attenuator while the laser energy was being constantly updated on the computer monitor. The laser energy would be decreased in approximately 10% steps until the fluorescence intensity was too low to be accurately measured. If smaller step sizes were used, the error in the energy measurement (~±2%) would be almost as large as the step size.

For the $M_2X_4L_4$ compounds and $Mo_2Cl_4(dmpm)_2$ the signal intensity was high enough that meaningful power dependence measurements (those comprised of more than 5 different energies) could be made at many different wavelengths across the spectrum. For the other $Mo_2Cl_4(\overset{\frown}{P\,P})_2$ compounds this was not the case and consequently the power dependence was measured only at one or two wavelengths.

II.B.2.c. Polarization Dependence Measurement

The polarization dependence was measured in a manner very similar to the process described for the TPE measurement, the only differences being that the signal was measured once with vertical polarization and once with circular polarization. Also, for the polarization dependence the step size between points was usually larger and the

number of times the signal intensity was measured was increased with respect to the TPE measurement. The signal intensity observed when circularly polarized light was used was divided by the intensity when linearly polarized light was used to yield Ω, the polarization ratio.

Chapter III

Two-Photon Spectroscopy of $Mo_2Cl_4(\overset{\frown}{P\,P})_2$ Complexes

III.A. Experimental Background of $M_2X_4(\overset{\frown}{P\,P})_2$

The opportunity to study a bond as it is systematically broken is provided by this class of compounds. The breaking of the δ-component of the metal-metal quadruple bond is accomplished by twisting one half of the molecule with respect to the other. The twist is introduced by the bridging diphosphine ($\overset{\frown}{P\,P}$) ligands. The effect of the twist (χ) on the electronic states of the δ-manifold is shown in Figure III.1. This figure also shows the dependence on the coupling (S)of the parent d_{xy} orbitals. Cotton and coworkers have demonstrated that the strength of the δ-bond follows a cos2χ dependence.[15] Ultimately, the energy gap that separates the diradical states gets small enough that the triplet state can be thermally populated.

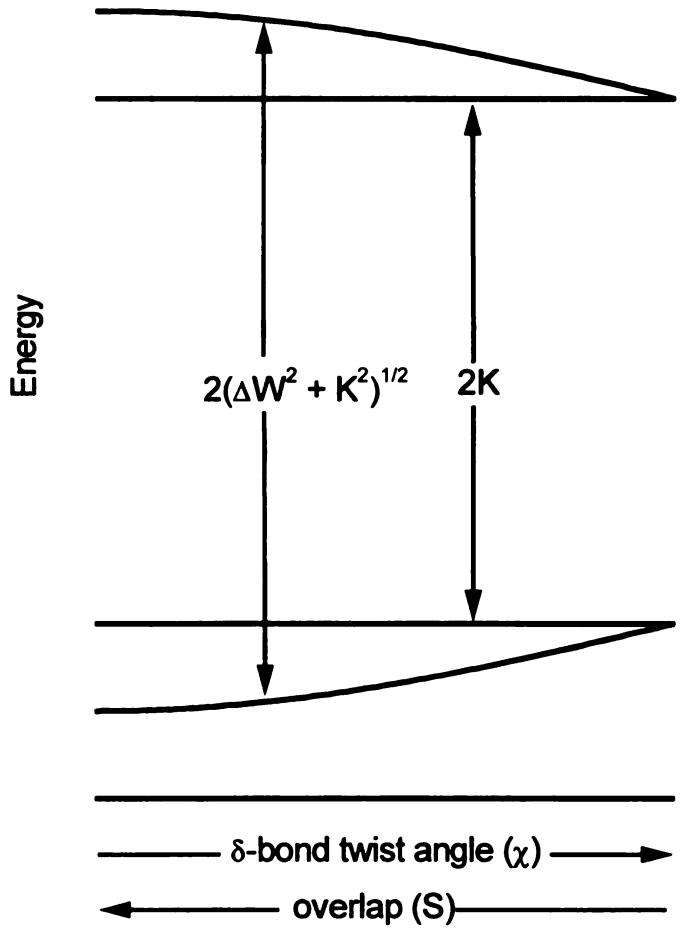

Figure III.1. The effect of the twist angle (χ) and overlap (S) on the electronic states of the δ-manifold.

As mentioned in chapter I, both Gray and Cotton have taken advantage of this feature of the δ-bond. Gray *et. al.* used a SQUID to measure the magnetic susceptibility of β-$Mo_2Cl_4(dmpe)_2$ where dmpe is bis(dimethylphosphino)ethane, which has a twist angle of approximately 40°[25] (50° as measured by Cotton *et al*[26]). The $^3\delta\delta^*$ state energy was measured to be in the 400 – 500 cm^{-1} range. From this single point, the separation was extrapolated based on the $\cos 2\chi$ dependence, to a 90° (and therefore 0°) twist angle. It was determined that the triplet state energy for a fully formed δ-bond was approximately 5200 cm^{-1}.

The magnetic susceptibility measurements required a great deal of high purity compound to be available. Cotton *et al* performed similar measurements using temperature dependent $^{31}P\{^1H\}$ NMR spectroscopy.[26] With this technique, as the temperature is raised there is more triplet character present, which leads to an upfield chemical shift and paramagnetically broadened peaks in the NMR spectra. From the measured shifts and peak widths, the triplet state energy of a number of $Mo_2Cl_4(\overset{\frown}{P\,P})_2$ compounds with twist angles that ranged from 24.7° to 64.9° was determined. Compounds with twist angles outside of this range could not be studied with this technique since the $^3\delta\delta^*$ states are too high in energy to be thermally populated without sample decomposition. However, when the data were extrapolated based on the $\cos 2\chi$ dependence the $^3\delta\delta^*$ state energy at 0° and 90° was estimated to be 4840 cm^{-1}. At 45°, where the δ-bond is formally annihilated, the $^3\delta\delta^*$ state was estimated to be 1230 cm^{-1} above the ground state. Derivatives where iodide and bromide replaced chloride were also studied. The $^3\delta\delta^*$ state energy for these compounds was also estimated to be 4840 cm^{-1}. Since there was only one sample studied for each of the different halides, as compared to seven for chloride, the conclusion is more speculative. Two W_2 derivatives were also studied, and their estimated $^3\delta\delta^*$ state energy at 0° (and 90°) was less than 4500 cm^{-1}.

In addition to the aforementioned studies on the $^3\delta\delta^*$ state, the $^1\delta\delta^*$ state of these compounds has also been studied. The $^1(\delta \rightarrow \delta^*)$ transition energy and extinction coefficients (ε) for those molecules investigated by NMR are reported in Table III.1, along with their respective triplet state energies and twist angles (χ).

The model developed in Chapter I is strictly adhered to by this class of compounds. As can be seen in Figure III.2a, which is a graphical representation of the data in Table III.1, both ($\delta \rightarrow \delta^*$) transitions red shift as the δ-bond is broken and blue shift as it is reformed. Furthermore, as shown in Figure III.2b, the intensity of the $^1(\delta \rightarrow \delta^*)$ optical transition is observed to decrease as the δ-bond is broken and increase as it is reformed. This is expected since the parent d_{xy} orbitals are becoming less coupled as the bond is broken. Mulliken demonstrated the linear dependence of oscillator strength on the square of the coupling (Equation I.1). A last point to be considered is that the energy difference between the $\delta\delta^*$ states (Figure III.2b) remains essentially constant as the δ-bond is twisted, which is also predicted by the model. The energy difference is 2K, where K is the two-electron exchange energy.

Only the δ^{*2} state remains to be observed in this class of compounds. If this state can be identified, all of the electronic states available to a two-center, two-electron bond will be spectroscopically determined.

III.B. Two-Photon Spectroscopic Results for $Mo_2Cl_4(\overset{\frown}{P\,P})_2$ Compounds.

The molecules investigated are listed in Table II.1 and represent only a subset of the molecules studied by Cotton. Sadly, only β-Mo_2Cl_4(S,S-dppb)$_2$ was able to provide interpretable spectra. The other complexes, $Mo_2Cl_4(dmpm)_2$, $Mo_2Cl_4(depe)_2$, and $Mo_2Cl_4(dppe)_2$, either did not display sufficiently strong emission, or the two-photon excitation spectrum was obscured by strong solvent absorption bands in the near infrared

Table III.1. Spectroscopic and structural data for $Mo_2Cl_4(\overset{\frown}{P\,P})_2$ compounds. $^1(\delta \rightarrow \delta^*)$ is the transition energy in cm^{-1}, ε is the extinction coefficient for the $^1(\delta \rightarrow \delta^*)$ transition at the maximum in $M^{-1}cm^{-1}$, $^3(\delta \rightarrow \delta^*)$ is the transition energy in cm^{-1} and χ is the twist angle in degrees. NM not measurable. Except as noted, the data was taken from Reference 26.

Compound	$^1(\delta \rightarrow \delta^*)$	ε	$^3(\delta \rightarrow \delta^*)$	χ
$Mo_2Cl_4(dmpm)_2$	15556	1730	NM	0
$Mo_2Cl_4(S,S\text{-}dppb)_2$	12513	1500	2240	24.7
$Mo_2Cl_4(depe)_2$	11690	NR	1320	41.4
$Mo_2Cl_4(dmpe)_2$	11484	210[25]	1290	50
$Mo_2Cl_4(dppe)_2$	12123	1030	1650	59.5
$Mo_2Cl_4(dppee)_2$	12812	2500	2250	64.5
$Mo_2Cl_4(dppp)_2$	13706	2680	2980	69.4
$Mo_2Cl_4(PMe_3)_4$	17150	3110	NM	90

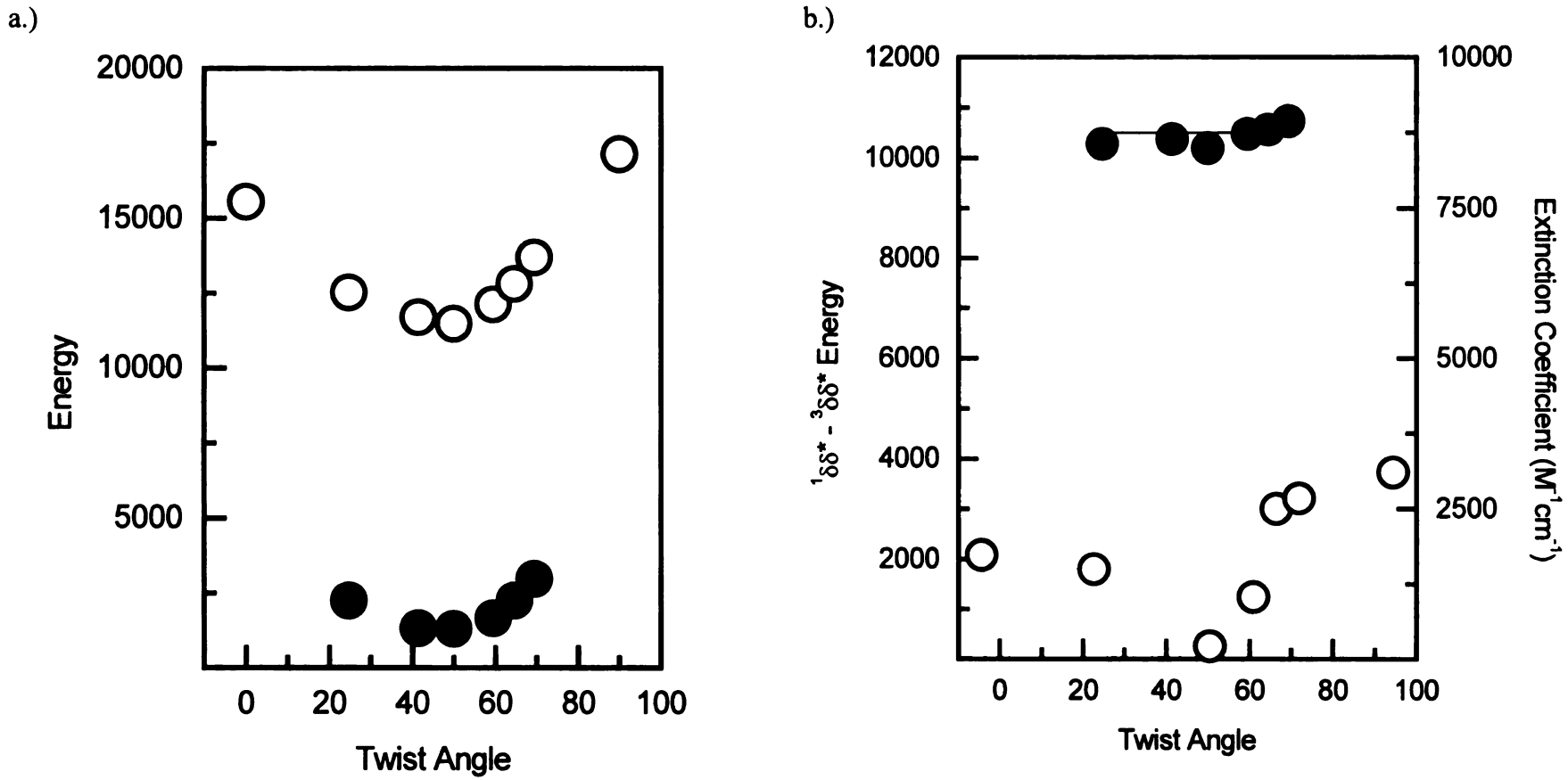

Figure III.2. a.) The energy of the $^1\delta\delta^*$ (hollow) and $^3\delta\delta^*$ (filled) states for $Mo_2Cl_4(\overset{\frown}{P\,P})_2$ compounds. b.) The energy difference between the $^1\delta\delta^*$ and $^3\delta\delta^*$ states (solid) is essentially constant at 10500 cm^{-1}. This corresponds to 2K, where K is the two-electron exchange energy. The extinction coefficient (hollow) for the $^1(\delta \rightarrow \delta^*)$ transition is also shown. The data was taken from Reference 26.

region. All of the complexes did display some emission when excited in the predicted region (based on Cotton's observations).

III.B.1. $Mo_2Cl_4(S,S,\text{-dppb})_2$

The absorption spectrum and low temperature emission spectrum of $Mo_2Cl_4(S,S\text{-dppb})_2$ are shown in Figure III.3. The lowest energy band in the absorption spectrum has been assigned as the $^1(\delta \rightarrow \delta^*)$ transition. The emission spectrum has not been previously reported for this compound, but since it is nearly a mirror image of the absorption spectrum and reasonable Stokes shifted it will be assigned to $^1(\delta^* \rightarrow \delta)$. The emission is observed only at reduced temperature (here at 77K) and is difficult to detect with a PMT since it lies in the near infrared region of the spectrum.

The two-photon fluorescence excitation spectrum and the solvent (3-methylpentane) absorption spectrum are shown in Figure III.4. The wavelength on the x-axis is the actual excitation wavelength and has not been divided by two to reflect the energy of the two-photon transition. The sharp band at 1180 nm and the series of bands from 1380 – 1500 nm are present in both the two-photon fluorescence excitation and absorption spectra. The sharp bands in the two-photon excitation spectrum are artifacts of solvent absorption and are the primary reason why the spectra of $Mo_2Cl_4(depe)_2$ and $Mo_2Cl_4(dppe)_2$ could not be readily interpreted.

The appearance of the bands in the two-photon excitation spectrum can be justified by considering the instrumental layout depicted in Figure II.1. The laser energy is measured by the photodetector after the laser beam has passed through the sample; therefore, if the solvent (or the sample for that matter) absorbs a significant amount of the laser light, the energy measured is lower than the actual energy in the sample. The appearance of the bands can be explained by considering the most extreme example. When the laser beam first enters the sample, fluorescence is excited that is detected by the CCD. As the excitation beam passes through the sample the energy is reduced by

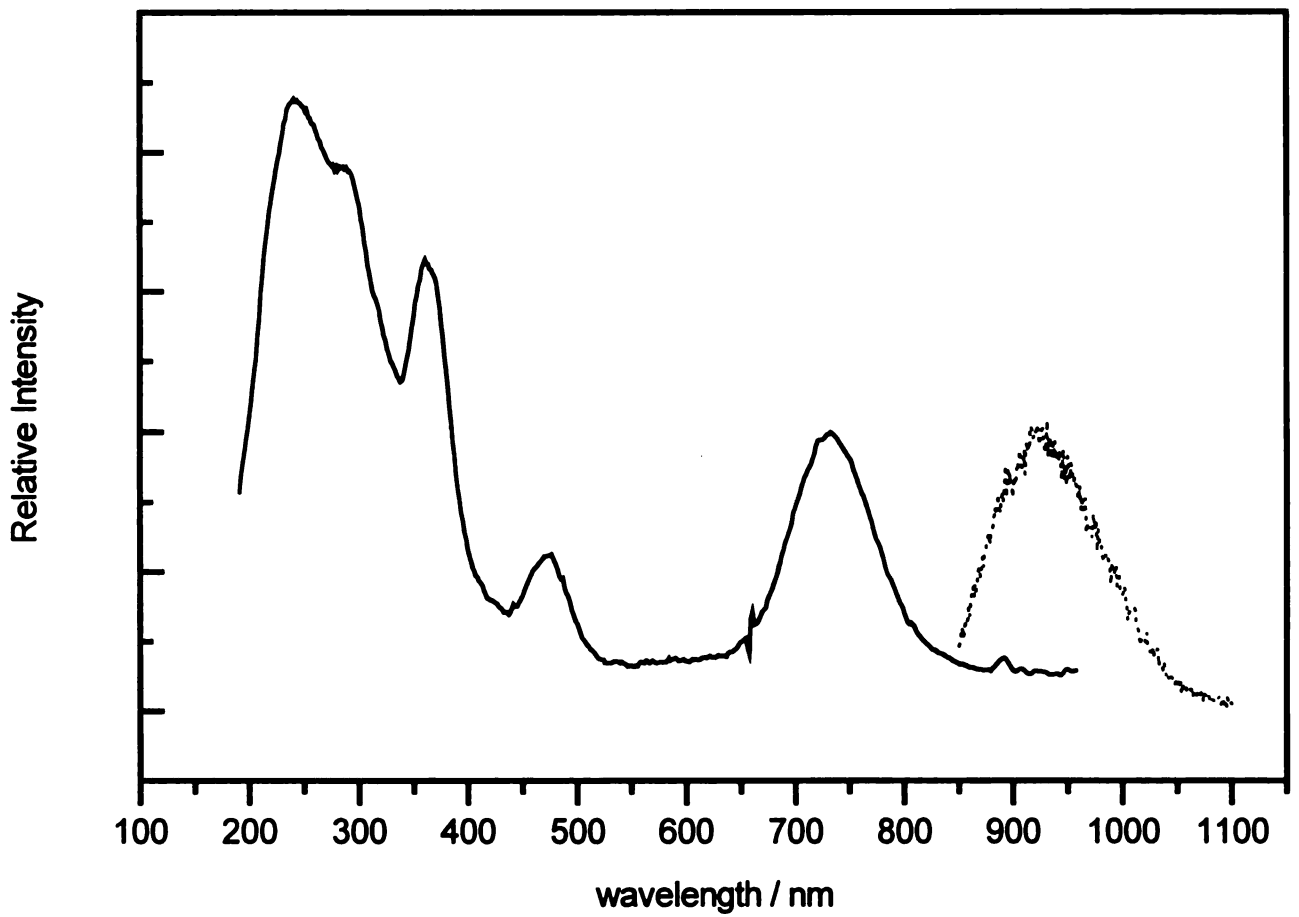

Figure III.3. Absorption (—) and low temperature emission (•••) spectra of Mo_2Cl_4(S,S-dppb)$_2$ in 3-methylpentane. The band in the absorption spectrum at 734 nm has been assigned as the $^1(\delta \rightarrow \delta^*)$ transition and the emission (925 nm) is assigned as $^1(\delta^* \rightarrow \delta)$. The emission spectrum was not corrected for the instrument response.

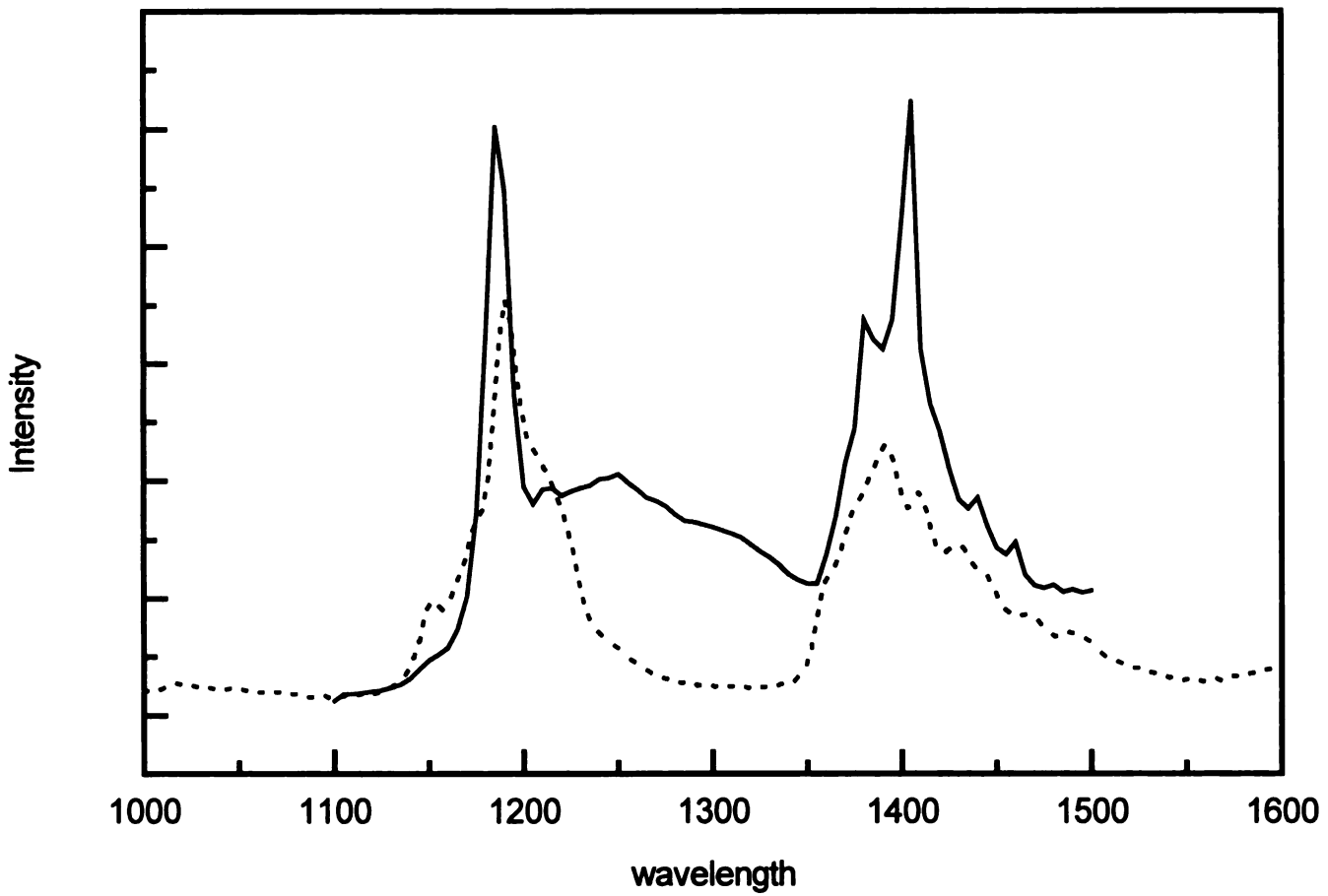

Figure III.4. The absorption spectrum of 3-methylpentane (•••) and two-photon fluorescence excitation spectrum of Mo_2Cl_4(S,S-dppb)$_2$ (—). The bands in the solvent absorption spectrum at 1180 nm and 1380 – 1500 nm are manifested in the two-photon excitation spectrum.

solvent absorption to a level that cannot be measured by the photodetector. This scenario would lead to an infinite two-photon fluorescence excitation signal, since the signal is determined by dividing the fluorescence intensity by the square of the laser energy. An experiment was attempted where the laser beam was split before the sample, with a small portion (~ 10%) sent to the photodetector and the rest passing through the sample. This experiment failed because it was not possible to pick off enough of the laser beam for the energy measurement and still have enough left to provide adequate excitation of the fluorescence. Also, with this arrangement, sharp dips in the spectrum would be predicted since the measured energy would be greater than the energy in the sample.

Figure III.5 shows the absorption and two-photon excitation spectra of $Mo_2Cl_4(S,S\text{-dppb})_2$ where the two-photon spectrum has been plotted versus the wavelength that represents the energy of the transition (i.e. excitation wavelength/2). If one ignores the bands due to solvent absorption (590 nm and 690 – 750 nm) another broad band is seen with a maximum at 625 nm (16000 cm^{-1}). The polarization ratio across this band and power dependence of the emission intensity excited at 1250 nm are shown in Figure III.6 a and b respectively. The polarization ratio is less than 1 across the entire band (including the artifact peaks) and the power dependence displays a slope of 2.02. The polarization ratio below 1 indicates that the symmetry of the excited state is the same as the ground state, which is A for this molecule of nominally D_2 symmetry (Table I.2). The power dependence indicates that two photons are involved in the fluorescence excitation.

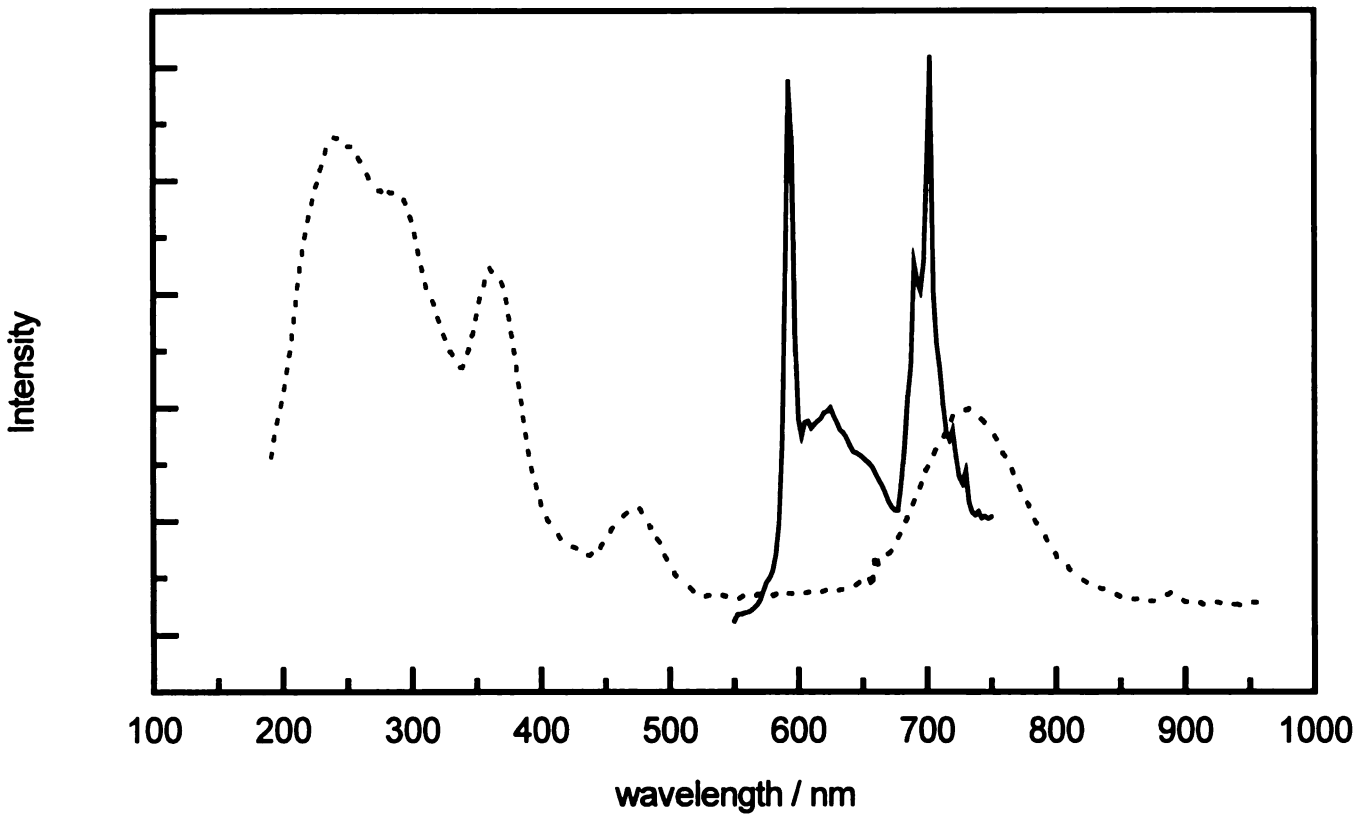

Figure III.5. The absorption (•••) and two-photon fluorescence excitation (—) spectra of $Mo_2Cl_4(S,S\text{-dppb})_2$. When the artifacts due to solvent absorption are ignored, the two-photon fluorescence excitation spectrum displays a maximum at 625 nm.

a.)

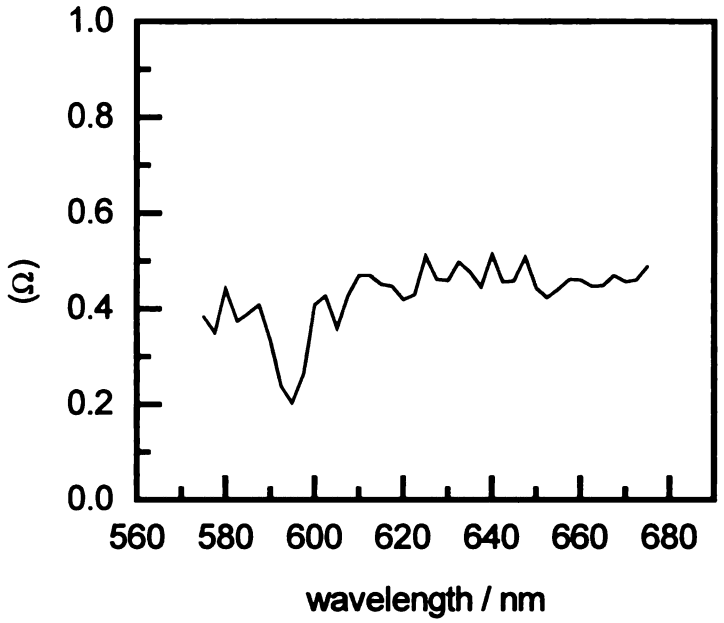

b.)

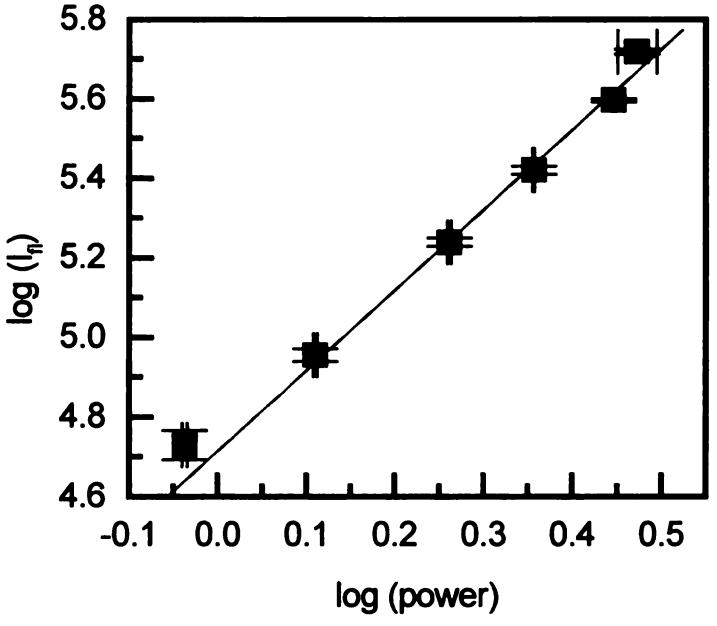

Figure III.6. a.) The polarization ratio (Ω) is plotted versus the wavelength and has a value less than 1 across the entire band. b.) The power dependence, which is a plot of the observed fluorescence intensity (I_{fl}) versus relative laser intensity (power) has a slope of 2.02. The line represents the best fit following a linear least squares analysis.

III.B.2. $Mo_2Cl_4(depe)_2$

The absorption and emission spectra for $Mo_2Cl_4(depe)_2$ are shown in Figure III.7. The extinction coefficient for this compound has not been measured, but since its twist angle (41.4°) is close to a broken δ-bond, it may be assumed that its extinction coefficient is very similar to $Mo_2Cl_4(dppe)_2$ (50°) which is 210 $M^{-1}cm^{-1}$. Because of the low absorptivity the molecule does not display a strong luminescence relative $Mo_2Cl_4(S,S\text{-}dppb)_2$. The weak emission, coupled with strong solvent absorption, made it impossible for the two-photon spectrum to be unambiguously interpreted. This compound was studied in two solvent systems. The first was 3-methylpentane, which worked well for $Mo_2Cl_4(S,S\text{-}dppb)$; in this solvent, it was impossible to obtain a two-photon fluorescence excitation spectrum since the emission was very weak due to limited solubility. A one-to-one mixture of CH_2Cl_2 and toluene was then used with hopes of increasing the solubility and therefore the emission. With this solvent combination a spectrum was obtained that is shown along with the absorption spectrum of a CH_2Cl_2/toluene solution in Figure III.8. Again, the solvent has strong absorbances that are manifested in the two-photon spectrum. If the obvious artifacts are ignored, a maximum can be seen at 1495 nm (747.5 nm when the energy of the transition is considered). It cannot be determined whether this is a true maximum or another artifact. Despite the increased solubility in the mixed solvent relative to 3-methylpentane, the fluorescence detected from this compound is significantly less than that for $Mo_2Cl_4(S,S\text{-}dppb)_2$. When $Mo_2Cl_4(S,S\text{-}dppb)_2$ was excited at its λ_{max} (1250nm) it yielded a fluorescence intensity of approximately 1000 counts at its observed emission maximum when the CCD was exposed to the fluorescence for 30 seconds (3000 laser shots). For $Mo_2Cl_4(depe)_2$, the CCD detector was exposed for 100 seconds (10000 laser shots) and only approximately 100 counts were registered at its emission maximum. This extremely low signal, coupled with the fact that the observed maximum in the two-photon spectrum is quite different from that

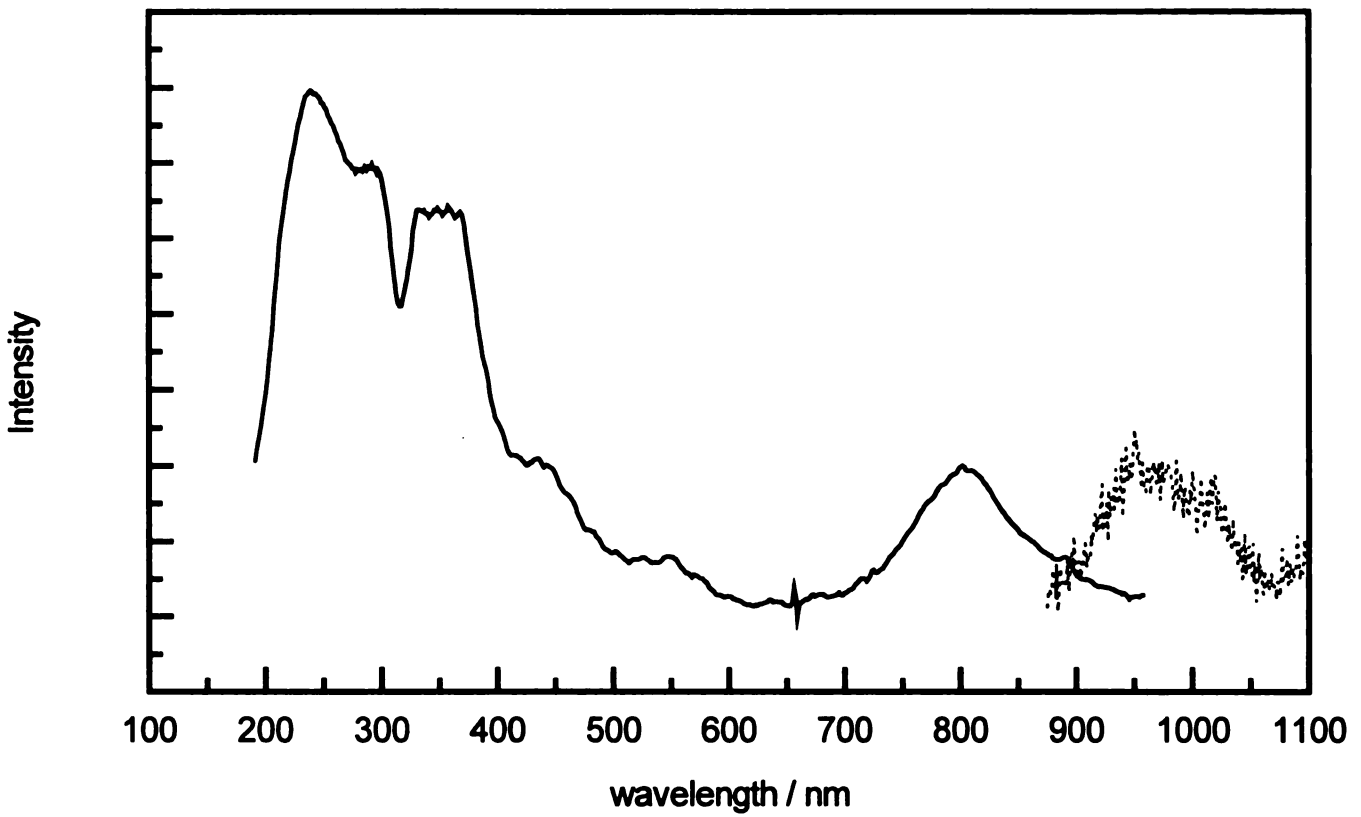

Figure III.7. Absorption (—) and low temperature emission (•••) spectra of $Mo_2Cl_4(depe)_2$. The spectra were collected in 3-methylpentane solution. The emission spectrum was collected at 77K.

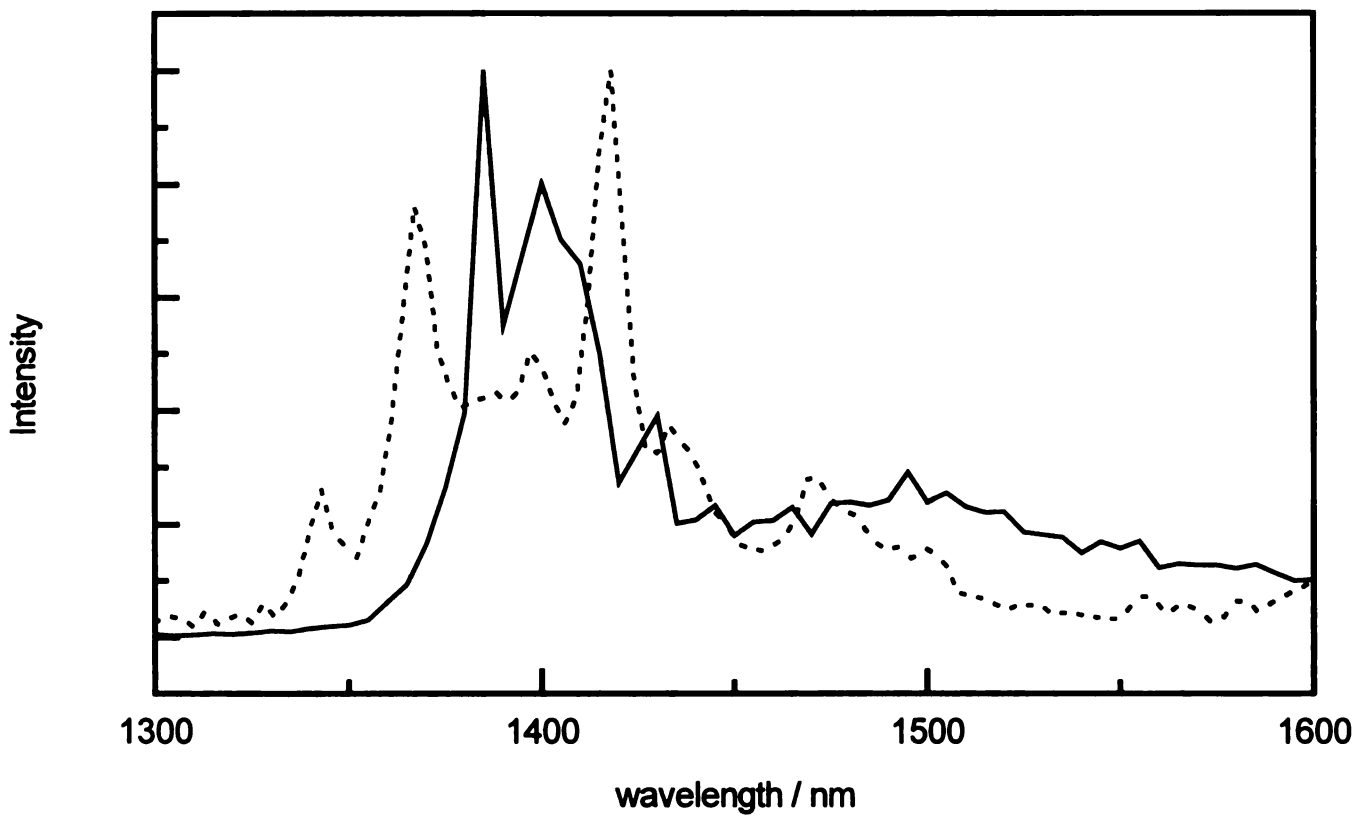

Figure III.8. The absorption spectrum of 1:1 CH_2Cl_2/toluene (•••) and two-photon fluorescence excitation spectrum (—) of $Mo_2Cl_4(depe)_2$ in this solvent. As with $Mo_2Cl_4(S,S\text{-}dppb)_2$, the most prominent bands can be attributed to artifacts due to strong solvent absorption. If the artifacts are ignored, a band may be observed at ~1495 nm.

predicted from Cotton's data (~1450 nm) leads to guarded interpretation. Furthermore, the low emission intensity precluded the measurement of either the power dependence or the polarization ratio. It should be noted that when the polarization of the laser beam was circular, there was no emission observed from the sample whereas when the laser beam is linearly polarized there is some emission This observation indicates that the polarization ratio might be less than 1.

III.B.3. $Mo_2Cl_4(dppe)_2$.

This compound was the most difficult to study. Its absorption spectrum is shown in Figure III.9. It did not display an detectable emission when excited with the Xe lamp in the emission instrument. However, when excited with the pulsed laser at 770 nm $Mo_2Cl_4(dppe)_2$ did emit (Figure III.9). Also, when the compound was excited in the near infrared at 1450 nm (as predicted from Cotton's data) emission was detected with the CCD detector. However, the emission was extremely weak, only 20 counts when the fluorescence was integrated for 100 seconds (10000 laser shots). A two-photon excitation spectrum was attempted (several times) and the results are shown in Figure III.10. The features that are displayed in the spectrum can be attributed solely to artifacts due to solvent (CH_2Cl_2/toluene) absorption.

III.B.4. $Mo_2Cl_4(dmpm)_2$.

For this compound, it was not possible to use the CCD detector since the CCD is very sensitive to the two-photon excitation wavelengths (800 – 1000 nm) that were used. A small amount of scattered laser light would inevitably reach the CCD and cause it to saturate. Therefore, the double monochromator and PMT configuration depicted in Figure II.1 was used. The absorption spectrum of $Mo_2Cl_4(dmpm)_2$ is shown in Figure III.11. Like $Mo_2Cl_4(dppe)_2$, this compound did not display detectable fluorescence when excited with the Xe lamp. The sample did display sufficient fluorescence when excited

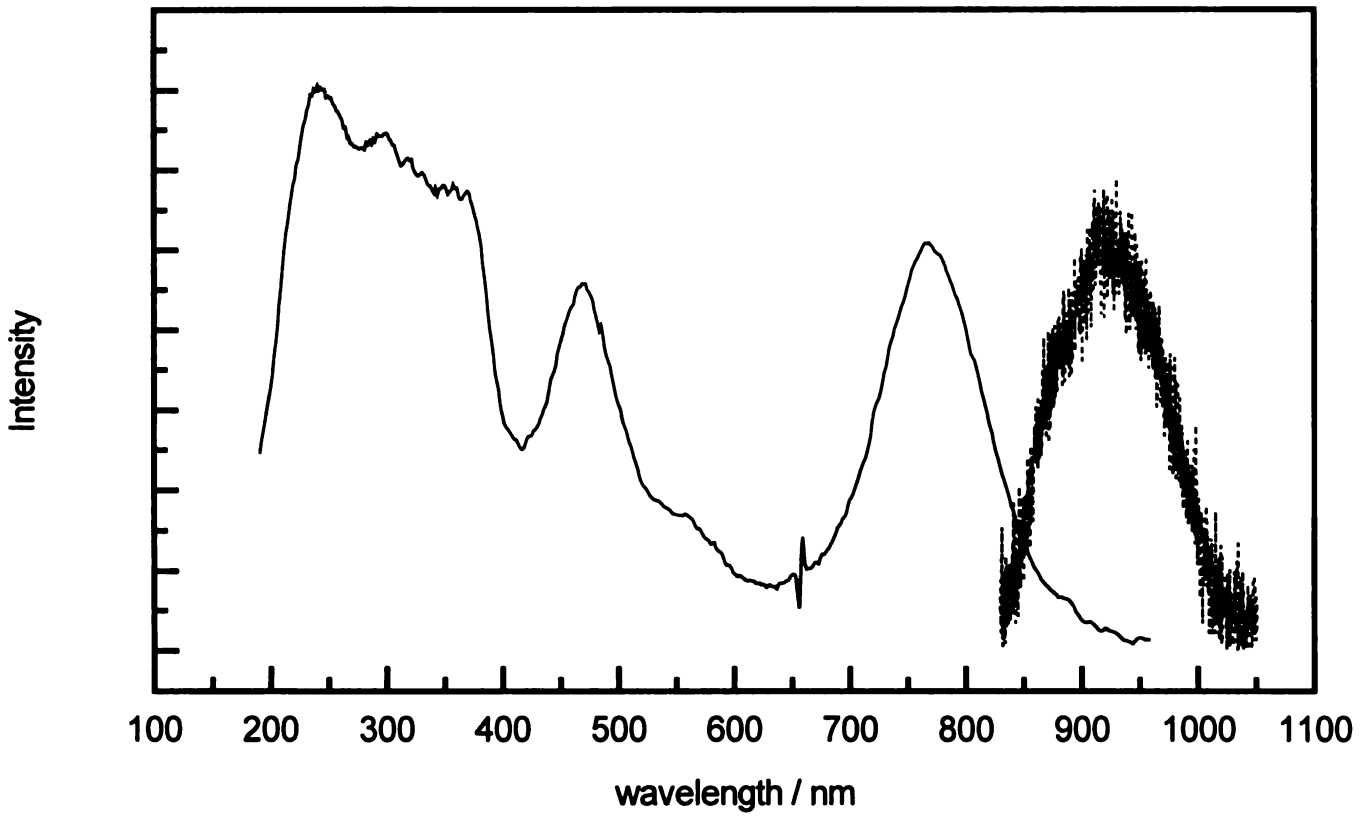

Figure III.9. The absorption spectrum (—) and the low temperature (120K) laser induced fluorescence spectrum (•••) of $Mo_2Cl_4(dppe)_2$ in 3-methylpentane.

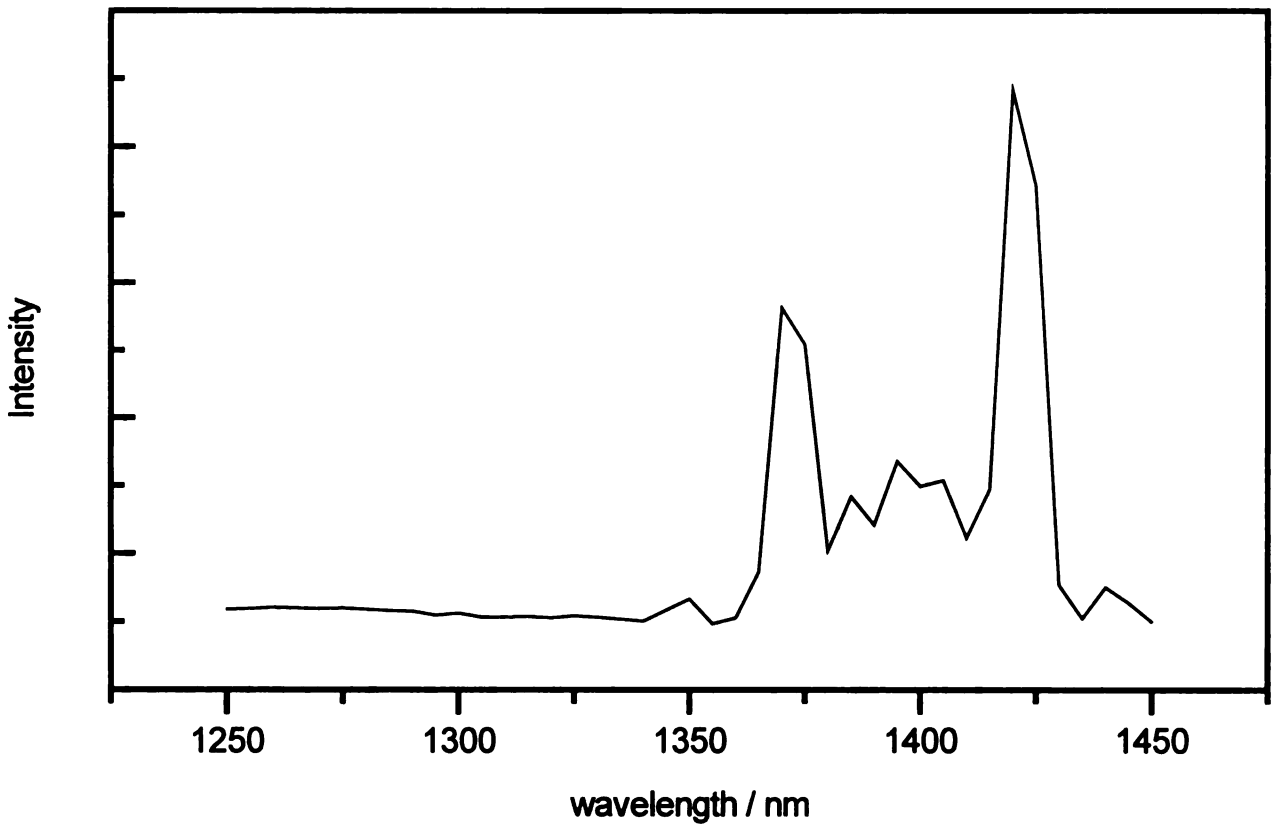

Figure III.10. Two-photon fluorescence excitation spectrum of $Mo_2Cl_4(dppe)_2$ in 1:1 CH_2Cl_2/toluene at 120 K. The only bands seen can be attributed to artifacts due to solvent absorption.

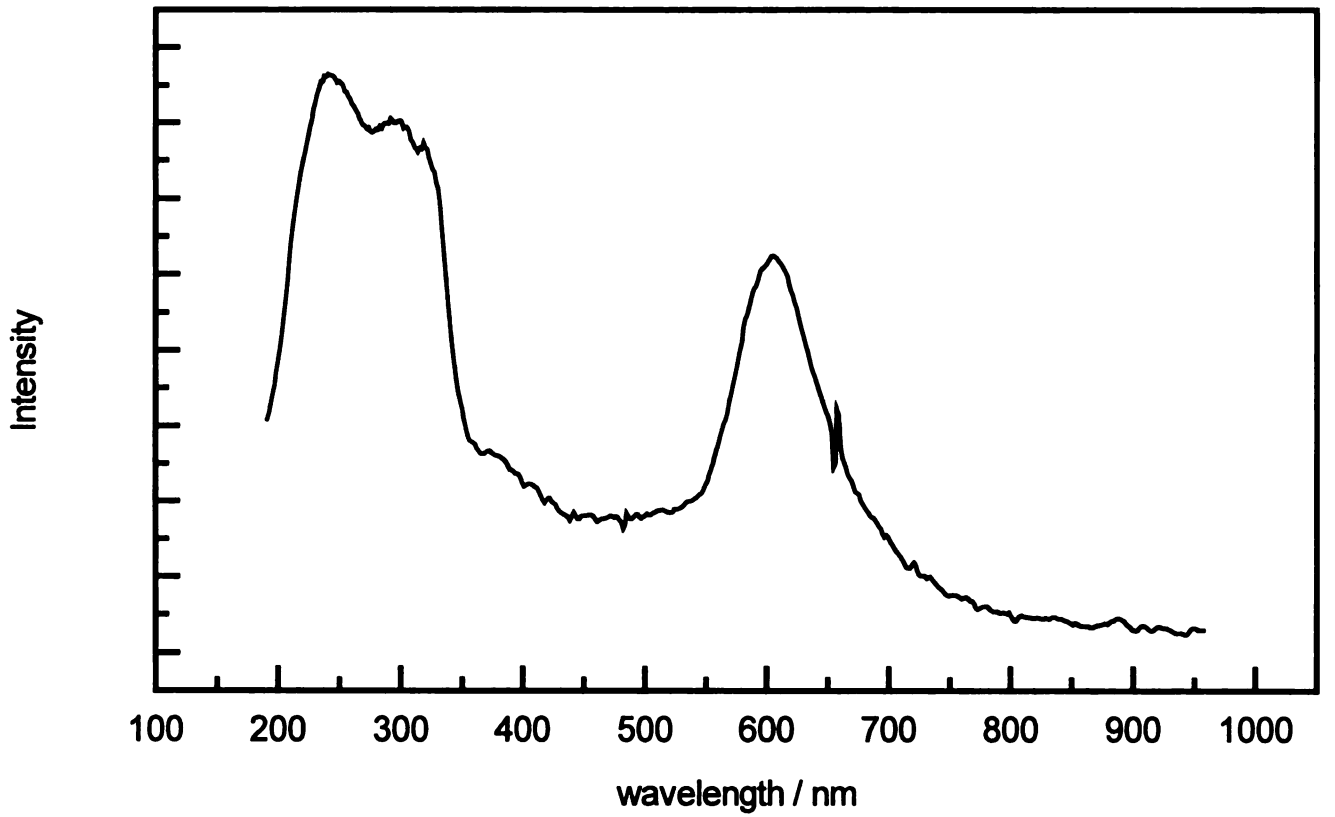

Figure III.11. The absorption spectrum of $Mo_2Cl_4(dmpm)_2$ in 3-methylpentane.

in the near infrared (950 nm, as predicted) that the lifetime of the emission could be measured as shown in Figure III.12. However, when the laser was scanned from 800 – 1100 nm, it was not possible to obtain a spectrum due to very low (4 counts/100 laser shots) fluorescence intensity.

III.C. Discussion

The only compound in this series to yield a two-photon fluorescence excitation spectrum that can be readily observed and quantitated is $Mo_2Cl_4(S,S\text{-dppb})_2$. The energy difference between the $^1(\delta \rightarrow \delta^*)$ λ_{max} (734 nm) and the $^1(\delta^2 \rightarrow \delta^{*2})$ λ_{max} (625 nm) is 2375 cm^{-1}, which corresponds to the energy gap between the zwitterionic states. Cotton measured the triplet state energy, which can be equated to the energy gap between the diradical states, to be 2240 cm^{-1} for this compound. The similarity of the energy gaps in consistent with the model developed in Chapter I and displayed in Figure III.1. This demonstrates that the δ-bond can be quite accurately described by the age-old model developed originally for the hydrogen molecule. Most importantly, the δ-bond provides the first opportunity to spectroscopically investigate all of the electronic states available to weakly coupled electrons in a two-center, two-electron bond.

Although the spectra of the other compounds in the series could not be readily interpreted, the fact that they all emit when excited at the predicted wavelengths provides hope that they can in the future, be studied by two-photon fluorescence excitation. For this to be accomplished, two different avenues could be pursued. The first would involve modifications to the instrument. If a longer path length cell was used, more molecules could be exposed to the laser beam and higher fluorescence should result. To properly image a longer path length cell on the entrance slits of the monochromator it would be necessary to either use cylindrical lenses to effectively rotate the fluorescence image by 90° or to literally rotate the monochromator by 90°. This option would be most effective

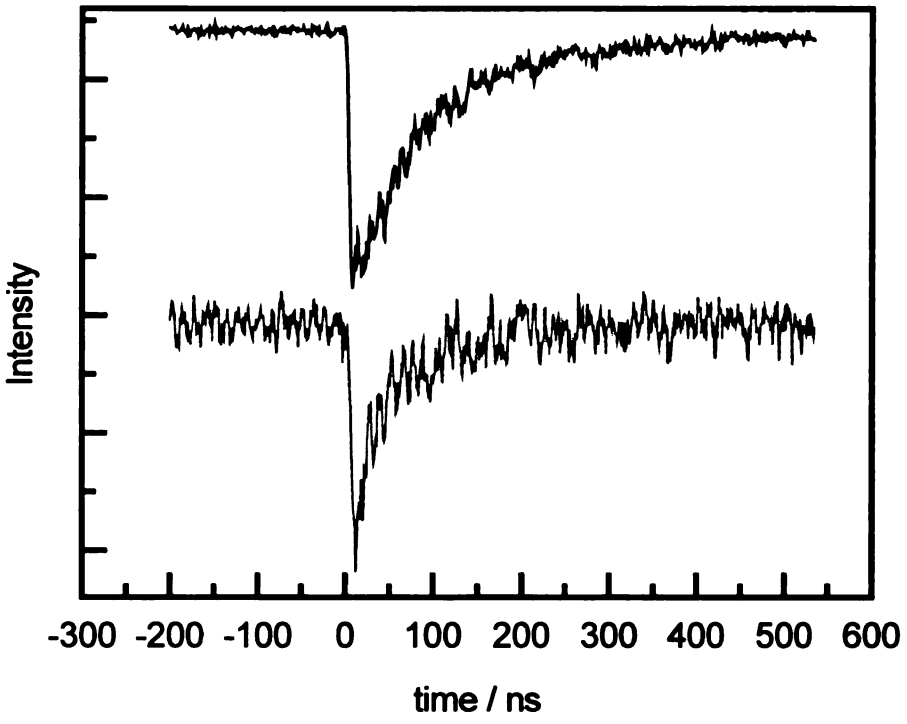

Figure III.12. The time dependent fluorescence of $Mo_2Cl_4(dmpm)_2$ in 3-methylpentane at 120 K when excited at 600 nm (top) and 950 nm (bottom). The one-photon induced fluorescence has a lifetime of 83 ns. The two-photon induced fluorescence was difficult to fit due to the low fluorescence but yielded a biexponential decay values of ~10 ns and ~80 ns. The short component may be due to scattered laser light. The fluorescence was detected at 675 nm. The one-photon induced fluorescence signal represents the average of 50 laser shots, while the two-photon induced fluorescence signal was collected with 5000 laser shots. Also, the slits on the monochromator were much wider (8 mm) for the two-photon induced fluorescence than for the one-photon induced fluorescence the slits were 0.1 mm.

for $Mo_2Cl_4(dmpm)_2$ since its two-photon fluorescence excitation spectrum is not expected to be strongly affected by solvent absorption. The solvent bands that conceal the spectra of $Mo_2Cl_4(depe)_2$ and $Mo_2Cl_4(dppe)_2$ are likely due to overtones of C-H stretches. By dissolving these compounds in perfluorinated solvents it should be possible to move the C-H stretches around, or possibly avoid them all together. Another possibility is to avoid solvent altogether, either by isolating the molecules in a rare gas matrix or placing a concentrated solution on a sapphire window and allowing the solvent to evaporate. These last two possibilities must be approached with caution since high laser energies (~5 mJ/pulse) are used to excite the fluorescence, which is very likely to damage the sample.

Chapter IV

Two-Photon Spectroscopy of $M_2X_4L_4$ Complexes

IV.A. Spectroscopic Background for $M_2X_4L_4$ Compounds[40,54]

The $M_2X_4L_4$ class of compounds is the most heavily studied class of quadruply bonded complexes. This stems from the systematic perturbations that can be performed due to the variety of ligands that are available. Also, most of the complexes are readily crystallized and thus provide important structural information to help interpret spectroscopic observations.

A great deal of the spectroscopy of these compounds was performed under the direction of Harry Gray. Measurements were made under a variety of conditions that included alkane solutions at room temperature and 77K, single crystal studies at room temperature and 10K, emission from samples under all conditions and also fluorescence excitation. A numbering scheme for the bands in the UV/visible spectra of these compounds was developed in the literature and will be adhered to here to maintain consistency with previously published work. The UV/visible spectrum of

$Mo_2Cl_4(PMe_3)_4$ is shown in Figure IV.1. This spectrum is representative of the $M_2X_4L_4$ class of compounds. The bands are labeled as indicated in the literature.

The most heavily studied transition is $\delta\delta^* \leftarrow \delta^2$ ($^1(\delta \rightarrow \delta^*)$) metal-to-metal charge transfer (MMCT), due to its uniqueness to quadruply bonded complexes. This transition produces the lowest energy band (Band I) observed in the UV/visible spectrum of this class of compounds. The wavelength maximum (λ_{max}) and extinction coefficient (ε) of this band is reported in Table IV.1 for each of the relevant compounds in alkane solution at room temperature. The assignment of Band I to the $^1(\delta \rightarrow \delta^*)$ transition is based on a number of spectroscopic observations. The band is polarized almost exclusively along the internuclear axis and progresses with a frequency (320 – 340 cm^{-1} for $Mo_2X_4(PMe_3)_4$ series) consistent with a metal-metal stretch. Also, excitation of this band gives rise to prompt luminescence that is a mirror image of the absorption band.

The next lowest energy band (Band III) observed in the UV/visible spectrum has been assigned as $\delta\delta^* \leftarrow \pi^4$ ($^1(\pi \rightarrow \delta^*)$) MMCT transition. This band progresses with a metal-metal stretching frequency that is somewhat lower energy than observed for the $^1(\delta \rightarrow \delta^*)$ transition. The lower energy progression is expected since this transition corresponds to moving a more strongly bonding π electron to the δ^* orbital. This transition is polarized perpendicular to the internuclear axis, also consistent with a $^1(\pi \rightarrow \delta^*)$ transition. The band is quite weak (Table IV.1) since it corresponds to a symmetry forbidden transition in the D_{4h} point group.

Band II is the next that is clearly observable in the spectra of these compounds. This is the most intense band seen in near-UV/visible region of the spectra and has been assigned as the ligand-to-metal charge-transfer (LMCT) transition $\delta\delta^* \leftarrow \sigma(MP)$ ($^1(\sigma(MP) \rightarrow \delta^*)$, where MP indicates that the origin lies in the metal-phosphine bond. The assignment is based on the fact that the band is more intense than the MMCT transitions. LMCT transitions are expected to be more intense due to the higher absorption cross-sections of their chromophores. MMCT transitions, on the other hand,

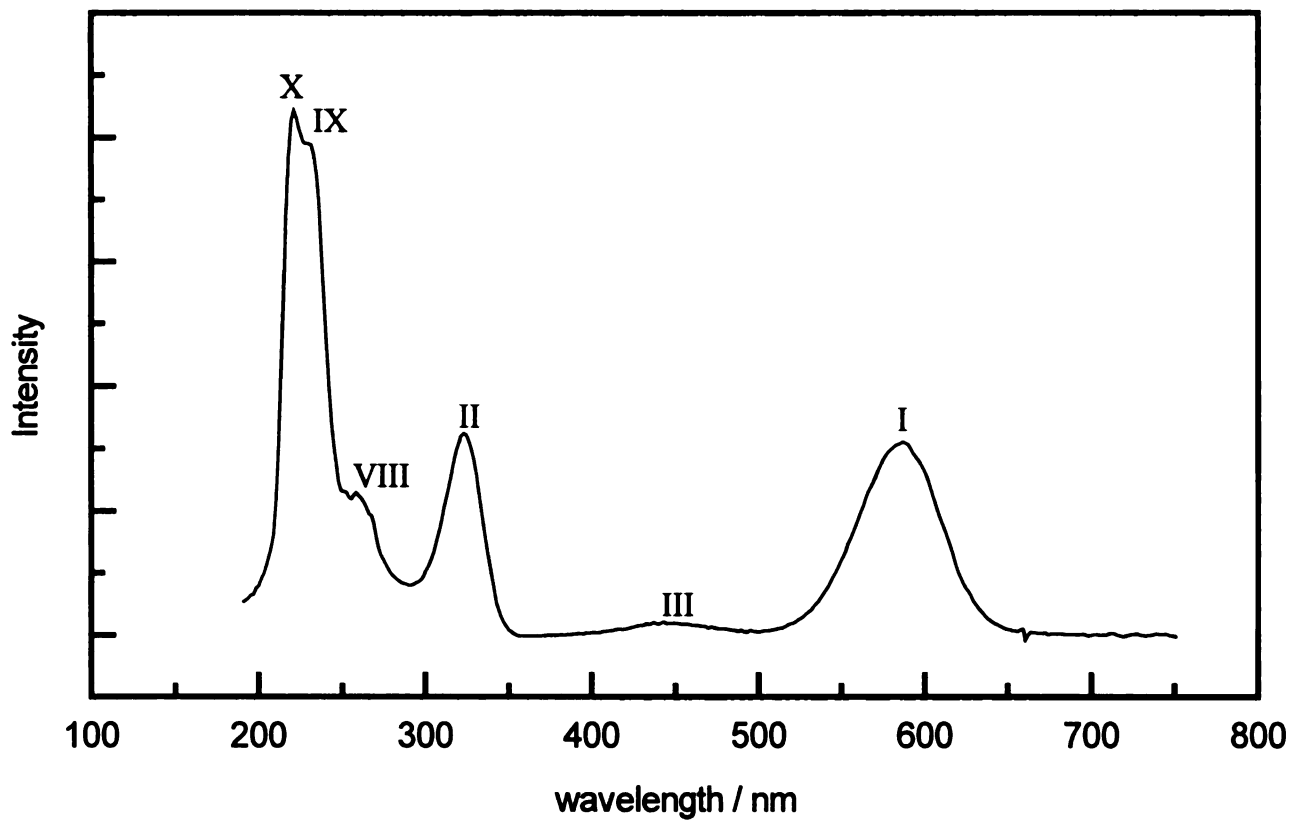

Figure IV.1. The absorption spectrum of $Mo_2Cl_4(PMe_3)_4$ in 3-methylpentane at room temperature. The numbering scheme for the bands was developed in the literature. As many as eleven bands can be seen in the spectra of $M_2X_4L_4$ compounds, depending on the sample conditions.

Table IV.1. The entries are in the form of nm ($M^{-1}cm^{-1}$). [a] reference 54a, [b] reference 40, and [c] reference 54b [d] reference 54c. [†]This band was only reported in the fluorescence spectrum and the extinction coefficient was not measured.

Compound	Band I	Band II	Band III
$Mo_2Cl_4(PMe_3)_4$	585 (3110)[a,b]	324 (3720)[b]	441 (210)[c]
$Mo_2Br_4(PMe_3)_4$	598 (4060)[a,b]	345 (6650)[b]	457 (310)[c]
$Mo_2I_4(PMe_3)_4$	636 (5250)[a,b]	395 (11850)[b]	495 (460)[c]
$Mo_2Cl_4(AsMe_3)_4$	574 (2970)[b]	323 (3630)[b]	423[d] (NR)[†]
$Mo_2Cl_4(PEt_3)_4$			
$W_2Cl_4(PMe_3)_4$	660 (4170)[b]	293 (9090)[b]	493 (460)[c]
$MoWCl_4(PMe_3)_4$			

are based on metal d-d transitions that have notoriously low cross-sections. Furthermore, the transition exhibits a strong blue-shift when W is substituted for Mo. Bands I and III both exhibit a red-shift with this substitution. The blue-shift is consistent with the decreased electronegativity of W, which leads to a larger energetic splitting of the σ and δ^* orbitals. Due to the significant red-shift that is observed as X is changed from Cl < Br < I, it is speculated that there is also a significant amount of halide character present in Band II.

To the blue of Band II there are two to five intense bands, plus some weaker bands that reveal themselves depending on the sample conditions labeled Band VII to Band XI. Since these bands are all energetically close to one another, a great deal of mixing occurs; thus, the assignments are more speculative than those for Bands I, II, and III. All of these bands show a strong dependence on the nature of the halide and have been assigned as halide-to-metal type LMCT transitions.

Fluorescence excitation spectra of these compounds show that all of the observed transitions lead to $^1\delta\delta^*$ luminescence. With the exception of the deep-ultraviolet bands of some compounds, the relative intensities of the bands in the fluorescence excitation spectra are the same as the relative intensities observed in the absorption spectra.

IV.B. Theoretical Observations on $M_2X_4L_4$ Compounds.

While no calculations performed on quadruply bonded dimers match the work done by Hay on $Re_2Cl_8^{2-}$[23] there have been a number of studies that provide useful albeit qualitative information on the $M_2X_4L_4$ class of compounds. One important observation made by Hay and supported by *ab inito* calculations on $M_2X_4(PH_3)_4$ complexes is that the δ and δ^* orbitals have a significant amount of halide character mixed into them.[55]. Cotton and Feng have also performed *ab initio* calculations on $Mo_2Cl_4(PH_3)_4$.[56] They

determined the $^3\delta\delta^*$ state to lie 5890 cm^{-1} above the ground state; in excellent agreement with experiment.[26]

Perhaps the most useful calculation, with respect to this dissertation, reported to date deals in particular with the halide dependence of the molecular orbitals of $M_2X_4(PH_3)_4$ compounds.[57] The results of these calculations are summarized pictorially in Figure IV.2. It was demonstrated that as the halogen is made less electronegative, the lone-pair electrons move into the metal-based orbitals involved in metal-metal bonding in general and the δ/δ^* orbitals in particular. When Cl is the halide, its 3p electrons are energetically below even the orbitals involved in metal-metal σ bonding. Because of this, there is little mixing of halide character into the metal-metal orbitals. The Br 4p electrons are energetically located between the metal orbitals involved in σ and π bonding and those of I fall between π and δ bonding metal-metal orbitals. Due to the increased mixing of the halogen orbitals, the $\delta\delta^*$ transition is seen to red shift upon substitution by a less electronegative halogen atom (Figure IV.3).

Further evidence for mixing of halide character into the δ-bond comes from resonance Raman data.[40] When polycrystalline samples of $Mo_2X_4(PMe_3)_4$ were excited with a laser line corresponding to their respective $^1(\delta \rightarrow \delta^*)$ transitions a band was observed that was attributed to the Mo-X stretch. While the intensities of the observed bands were not quantitated past the observation of "m" (moderate intensity), their presence in the resonance Raman spectra indicated that some metal-halide character is present in the δ manifold.

IV.C. Two-Photon Spectroscopic Results of $M_2X_4L_4$ complexes.

IV.C.1. $Mo_2Cl_4(PMe_3)_4$

$Mo_2Cl_4(PMe_3)_4$ was the first compound to be studied and reported in the literature.[52] The traces shown in Figure IV.4 show the conventional absorption spectrum,

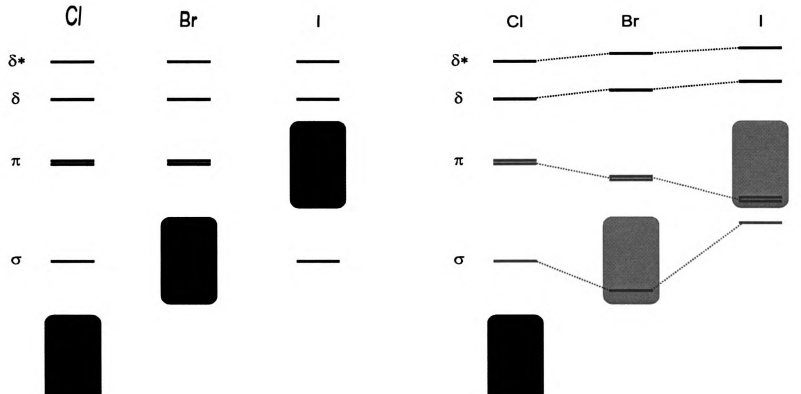

Figure IV.2. The effect of halogen atom substitution on the metal-based orbitals of $M_2X_4(PH_3)_4$ compounds. The left side of the figure is before the effect is "turned on" and the metal-based orbitals are independent of the halogen. The right side of the figure shows how the metal-based orbitals are affected by the halogen p orbitals.

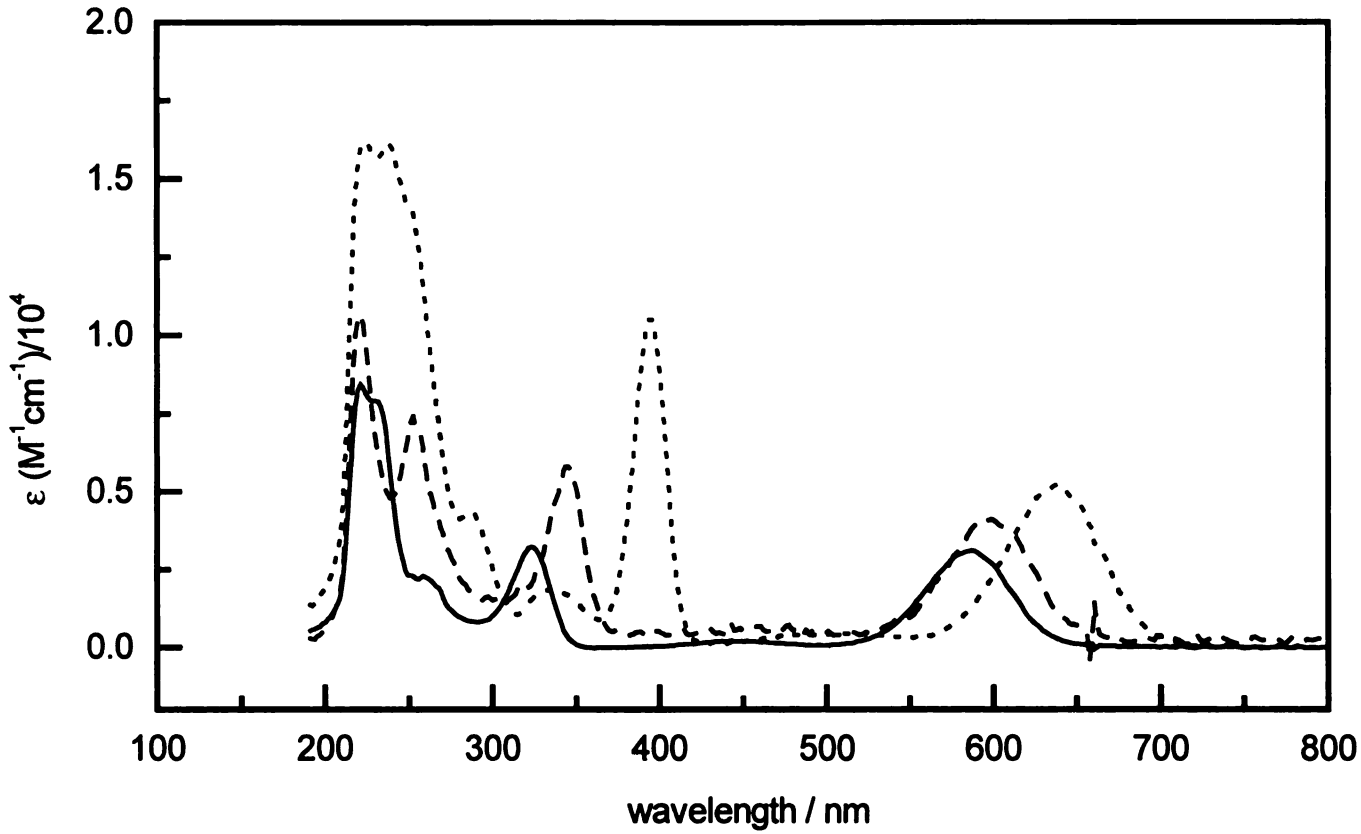

Figure IV.3. Absorption spectra (in 3-methylpentane) of the $Mo_2X_4(PMe_3)_4$ series; X = Cl (—), X = Br (- - -), X = I (•••). As the halide becomes less electronegative, the $^1(\delta \rightarrow \delta^*)$ transition red-shifts due to halide p electrons encroaching into the metal-metal bonding orbitals.

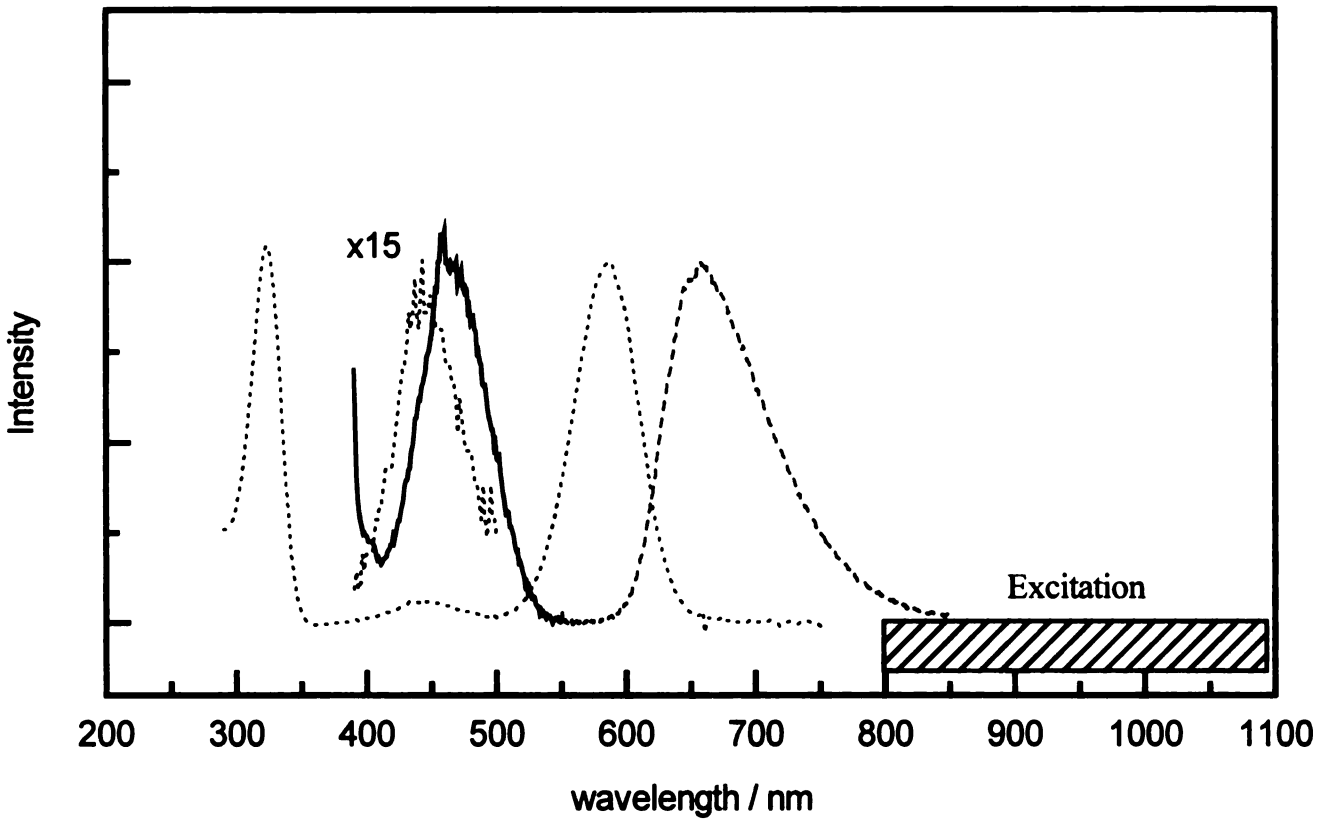

Figure IV.4. The absorption spectrum (•••) of $Mo_2Cl_4(PMe_3)_4$ in 3-methylpentane, where the $^1(\pi \rightarrow \delta^*)$ transition has been expanded by a factor of 15 to show that it is not coincident with the $^1(\delta^2 \rightarrow \delta^{*2})$ (—) transition. The emission spectrum (- - -) is generated when the compound is excited with either one or two photons. The two-photon excitation spectrum was generated by exciting in the near-infrared (/////).

the emission induced by one- and two-photon excitation, and the two-photon fluorescence excitation spectrum (that is represented as excitation wavelength/2). The hashed box in the near-infrared represents the wavelength of light that was used for two-photon excitation. The two-photon fluorescence excitation spectrum was collected using vertically polarized light and displays a maximum at 467 nm (21415 cm^{-1}). The rise on the blue edge of the spectrum is due to one-photon excitation of the red edge of the $^1(\delta \rightarrow \delta^*)$ transition. Band III in the absorption spectrum has been expanded by a factor of fifteen to show that it is not coincident with the two-photon band.

The power dependence and polarization ratio of the two-photon fluorescence excitation are shown in Figure IV.5a and b respectively. The power dependence shown in the figure was collected at 860 nm using vertically polarized light and is just one of many measurements taken at approximately 5 nm increments in both circularly and linearly polarized light. The power dependence at this particular wavelength was chosen because it demonstrates that the quadratic dependence is maintained for more than an order of magnitude change in fluorescence intensity. While this broad dynamic range was not observed for each of the power dependence measurements made, all of them displayed slopes of 2.00 ± 0.05. The polarization ratio (Ω) is less than 1 across the observed band. As indicated in section I.B.2.c, this implies that the excited state has the same symmetry as the ground state, namely A_1.

The aforementioned observations led to the assignment of the band as the $\delta^{*2} \leftarrow \delta^2$ ($^1(\delta^2 \rightarrow \delta^{*2})$) transition.[52] Gray's and Cotton's values for the diradical energy gap of 5200 cm^{-1} and 4840 cm^{-1} respectively, are in good agreement with the zwitterionic energy gap (as determined from the observed maxima of the transitions) of 4325 cm^{-1} measured from the two-photon spectrum.

a.)

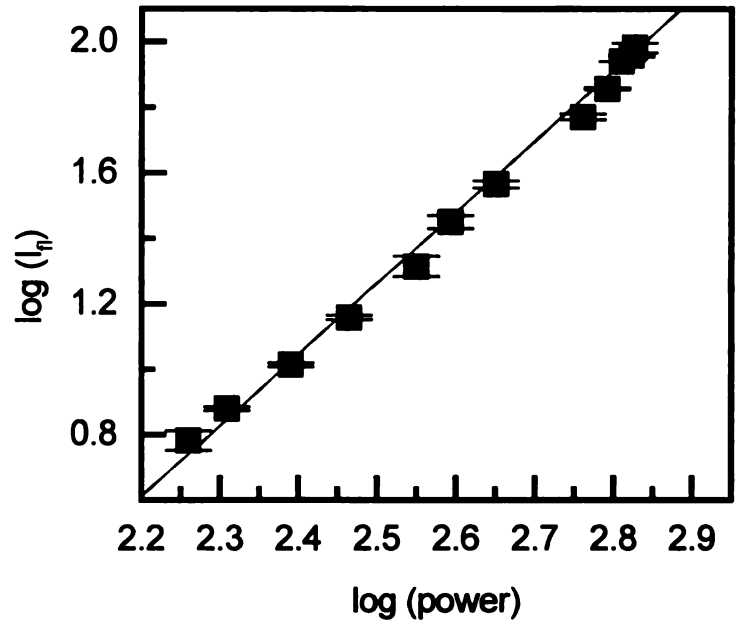

b.)

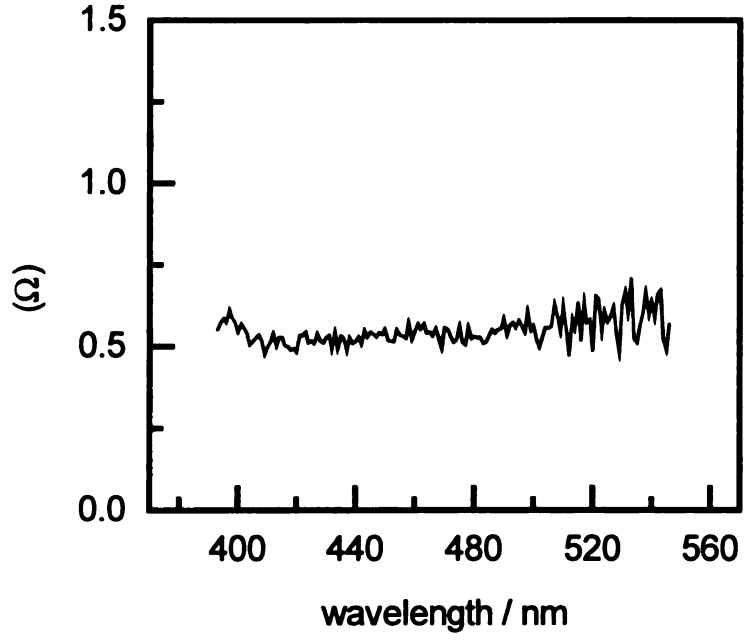

Figure IV.5. Measurements from the two-photon fluorescence excitation spectrum of $Mo_2Cl_4(PMe_3)_4$ in 3-methylpentane. a.) The power dependence when excited with 860 nm vertically polarized light. The line represents a best fit to a slope of 2.00. b.) The polarization ratio is less than one across the $^1(\delta^2 \rightarrow \delta^{*2})$ transition.

IV.C.2. $Mo_2Br_4(PMe_3)_4$

The absorption and two-photon fluorescence excitation spectra of $Mo_2Br_4(PMe_3)_4$ are shown in Figure IV.6. The $^1(\delta \rightarrow \delta^*)$ transition in the absorption spectrum displays a maximum at 598 nm (16720 cm^{-1}) and the $^1(\delta^2 \rightarrow \delta^{*2})$ spectrum has a maximum at 470 nm (21275 cm^{-1}). The power dependence and polarization ratio are displayed in Figure IV.7 a and b respectively. The power dependence (collected at 950 nm with vertical polarization) has a slope of 1.93. The power dependence was measured at several different wavelengths in both polarizations and yielded slopes that were similar (1.95 ± 0.05). This particular wavelength was chosen since it was measured near the maximum of the two-photon transition and displays a very broad range of fluorescence intensities. The polarization ratio is less than one across the $^1(\delta^2 \rightarrow \delta^{*2})$ band, which indicates that the excited state symmetry is the same as the ground state symmetry. It is seen to rise on the blue edge. This is likely due to excitation of the red edge of the $^1(\delta \rightarrow \delta^*)$ transition.

IV.C.3. $Mo_2I_4(PMe_3)_4$

The absorption and two-photon fluorescence excitation spectra of $Mo_2I_4(PMe_3)_4$ are shown in Figure IV.8. The $^1(\delta \rightarrow \delta^*)$ transition in the absorption spectrum displays a maximum at 636 nm (15723 cm^{-1}) and the $^1(\delta^2 \rightarrow \delta^{*2})$ spectrum has a maximum at 505 nm (19800 cm^{-1}). The power dependence and polarization ratio are displayed in Figure IV.9 a and b respectively. The power dependence (collected at 990 nm with vertical polarization) has a slope of 1.92. Power dependence was measured at several different wavelengths in both polarizations with slopes that were 1.94 ± 0.07. This depicted example was chosen since it was measured near the maximum of the two-photon transition and displays a very broad range of fluorescence intensities. The polarization ratio is less than one across the $^1(\delta^2 \rightarrow \delta^{*2})$ band, which indicates that the excited state

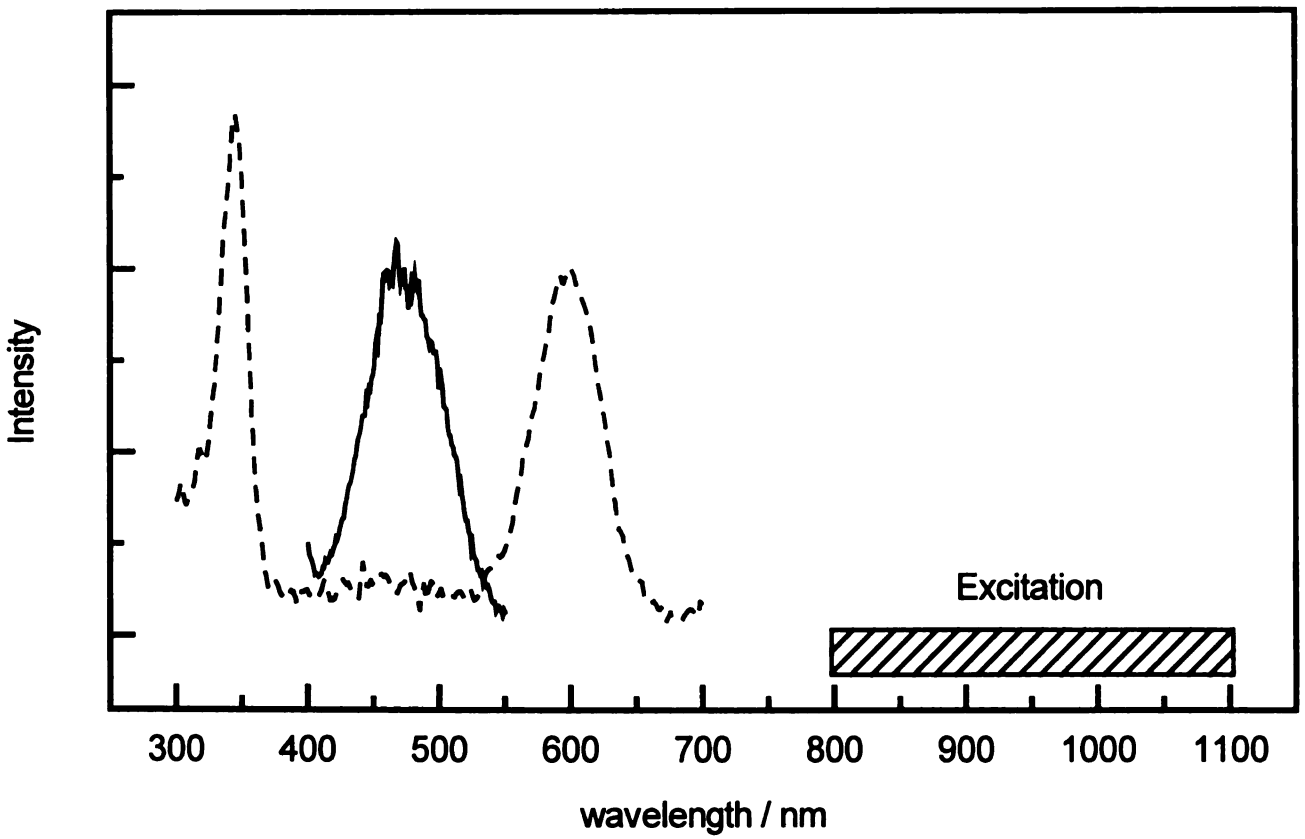

Figure IV.6. The absorption (- - -) and two-photon fluorescence excitation (—) spectra of Mo2Br4(PMe3)4 in 3-methylpentane at room temperature. The $^1(\delta \rightarrow \delta^*)$ transition has a maximum at 598 nm and the $^1(\delta^2 \rightarrow \delta^{*2})$ transition has a maximum at 470 nm. The region in the near-infrared (/////) corresponds to the excitation wavelength of the two-photon spectrum.

a.)

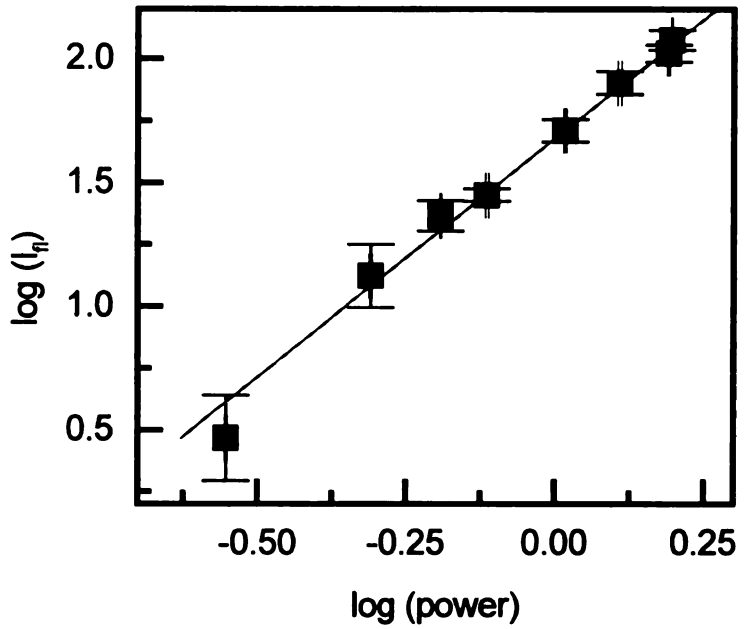

b.)

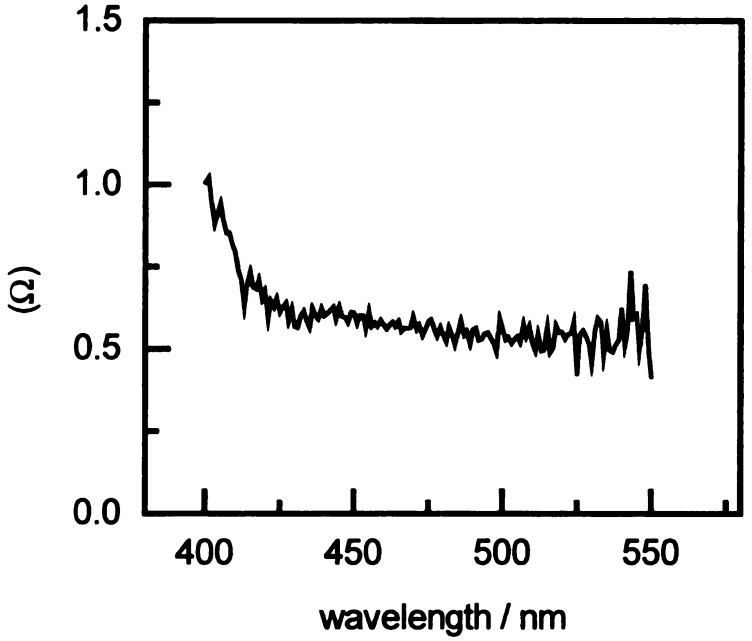

Figure IV.7. Measurements from the two-photon fluorescence excitation spectrum of $Mo_2Br_4(PMe_3)_4$ in 3-methylpentane. a.) The power dependence when excited with 950 nm vertically polarized light. The line represents a best fit to a slope of 1.93. b.) The polarization ratio is less than one across the $^1(\delta^2 \rightarrow \delta^{*2})$ transition. The rise on the blue edge can be attributed to one-photon excitation of the red edge of the $^1(\delta \rightarrow \delta^*)$ transition.

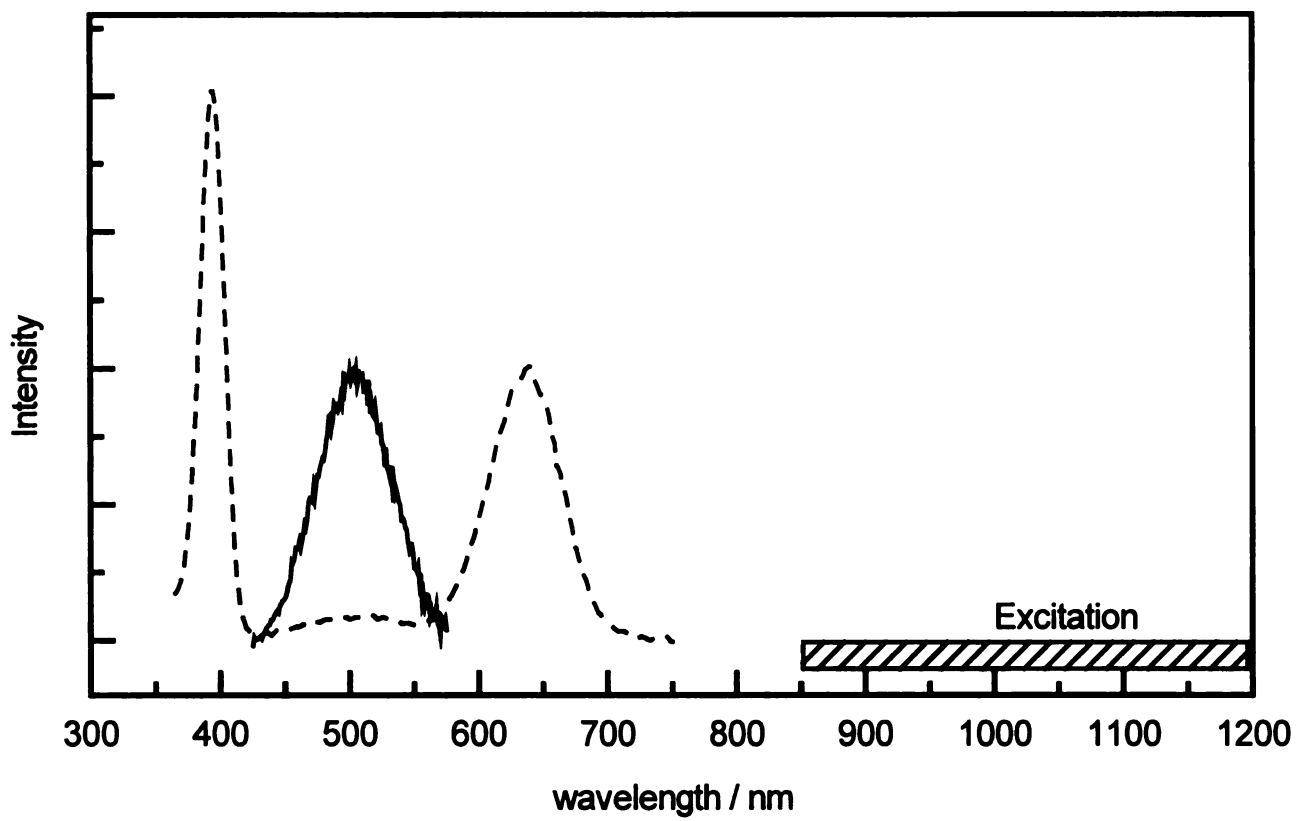

Figure IV.8. The absorption (- - -) and two-photon fluorescence excitation (—) spectra of $Mo_2I_4(PMe_3)_4$ in 3-methylpentane at room temperature. The $^1(\delta \rightarrow \delta^*)$ transition has a maximum at 636 nm and the $^1(\delta^2 \rightarrow \delta^{*2})$ transition has a maximum at 505 nm. The region in the near-infrared (/////) corresponds to the excitation wavelength for the two-photon spectrum.

a.)

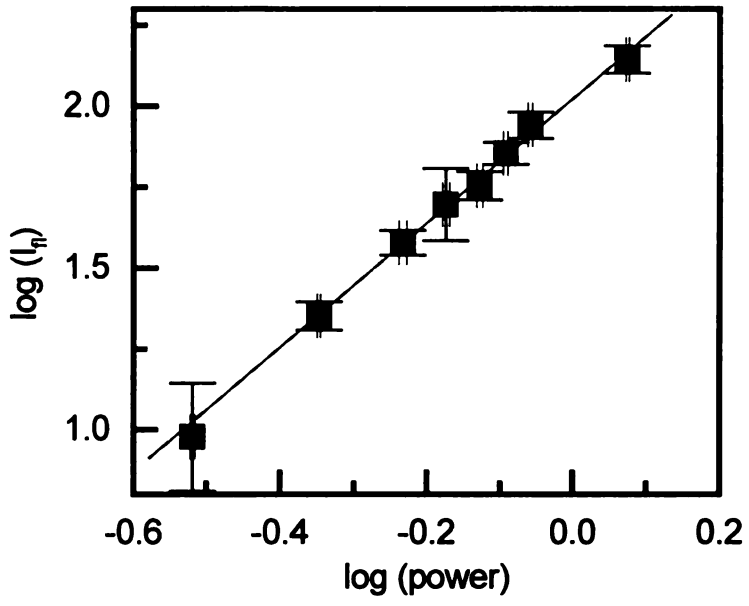

b.)

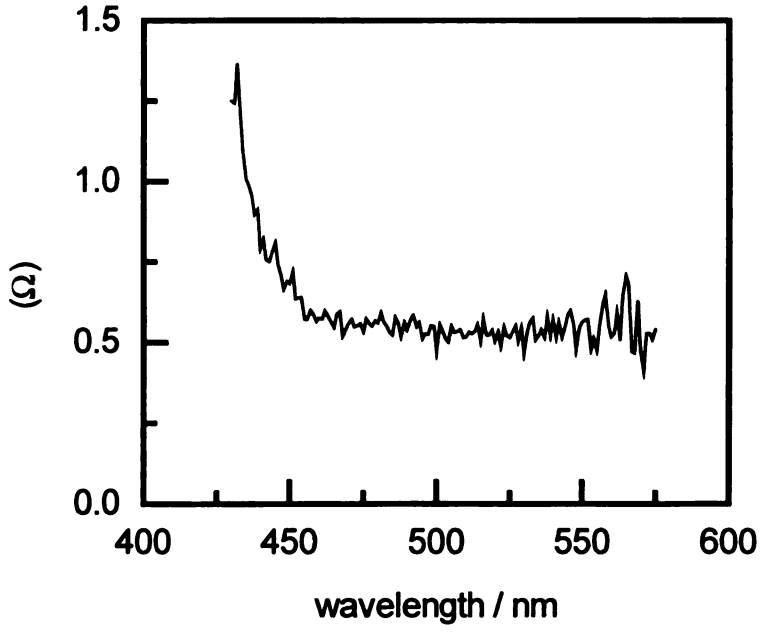

Figure IV.9. Measurements from the two-photon excitation spectra of $Mo_2I_4(PMe_3)_4$ in 3-methylpentane. a.) The power dependence when excited with 990 nm vertically polarized light. The line represents a best fit to a slope of 1.92. b.) The polarization ratio is less than one across the $^1(\delta^2 \rightarrow \delta^{*2})$ transition. The rise on the blue edge can be attributed to one-photon excitation of the red edge of the $^1(\delta \rightarrow \delta^*)$ transition.

symmetry is the same as the ground state symmetry. It is seen to rise on the blue edge. This is likely due to excitation of the red edge of the $^1(\delta \rightarrow \delta^*)$ transition.

IV.C.4. $Mo_2Cl_4(PEt_3)_4$

The spectra obtained for $Mo_2Cl_4(PEt_3)_4$ in 3-methylpentane are shown in Figure IV.10. The $^1(\delta \rightarrow \delta^*)$ transition in the absorption spectrum displays a maximum at 591 nm (16920 cm^{-1}) and the $^1(\delta^2 \rightarrow \delta^{*2})$ spectrum has a maximum at 474 nm (21100 cm^{-1}). The power dependence and polarization ratio are displayed in Figure IV.11 a and b respectively. The power dependence (collected at 950 nm with vertical polarization) has a slope of 1.99. The various power dependence measurements for this compound displayed slopes of 2.00 ± 0.05. The polarization ratio is less than one across the $^1(\delta^2 \rightarrow \delta^{*2})$ band, which indicates that the excited state symmetry is the same as the ground state symmetry. Like the $Mo_2X_4(PMe_3)_4$ compounds, the rise on the blue edge is likely attributable to one-photon excitation of the $^1(\delta \rightarrow \delta^*)$ transition. The polarization ratio also rises on the red edge; however, due to the noise it is difficult to tell if this is an artifact.

IV.C.5. $Mo_2Cl_4(AsMe_3)_4$

The two-photon fluorescence excitation, power dependence and polarization ratio measurements of $Mo_2Cl_4(AsMe_3)_4$ in 3-methylpentane were made with the first version of the instrumentation.[52] The absorption, emission and two-photon fluorescence excitation spectra are shown in Figure IV.12. The $^1(\delta \rightarrow \delta^*)$ transition exhibits a maximum at 573 nm (17450 cm^{-1}), the $^1(\delta^* \rightarrow \delta)$ at 638 nm and $^1(\delta^2 \rightarrow \delta^{*2})$ at 455 nm (21980 cm^{-1}). The power dependence and polarization ratio are shown in Figure IV.13a and b respectively. The power dependence was collected at 910 nm using vertically polarized light. The polarization ratio was collected point-by-point across the observed $^1(\delta^2 \rightarrow \delta^{*2})$ band in 5 nm increments. The power dependence has a slope of 2.09. The

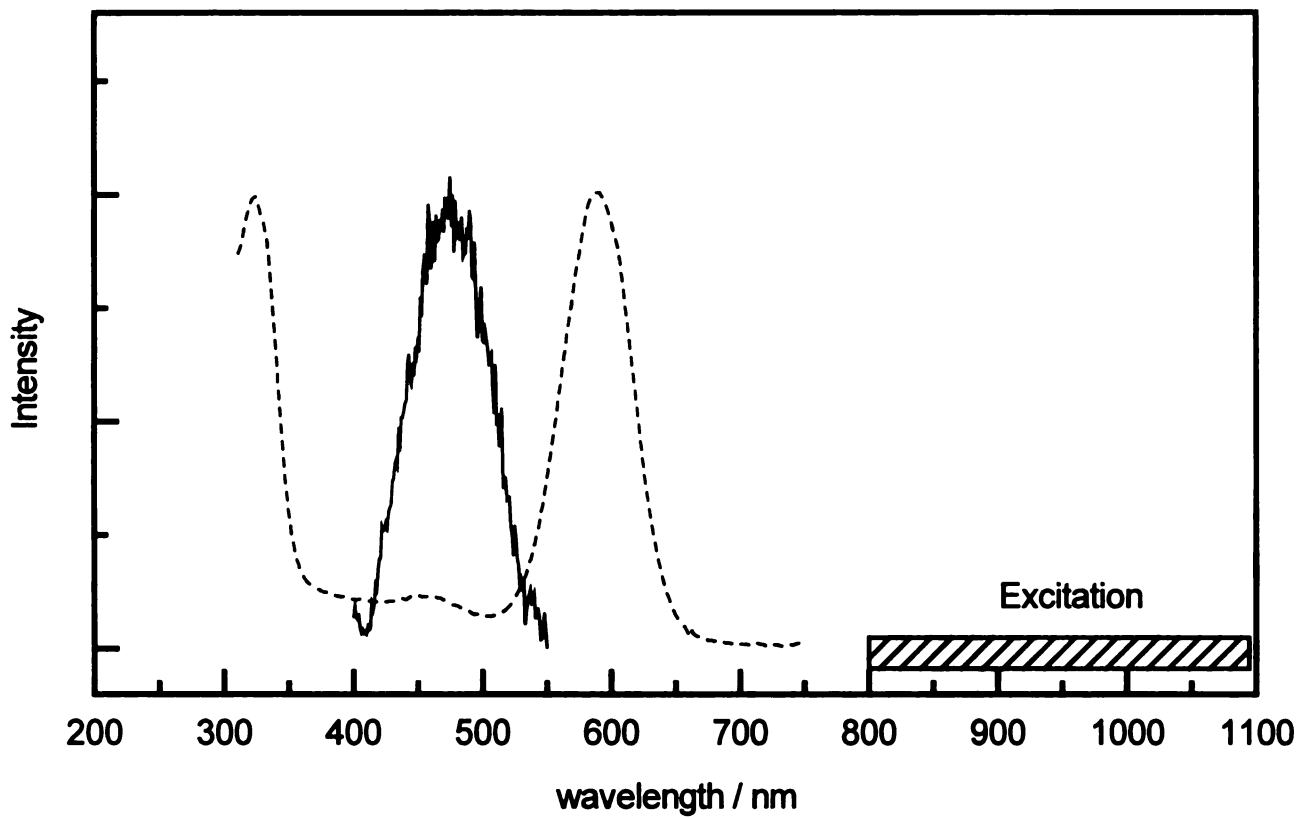

Figure IV.10. The absorption (- - -) and two-photon fluorescence excitation (—) spectra of $Mo_2Cl_4(PEt_3)_4$ in 3-methylpentane at room temperature. The $^1(\delta \rightarrow \delta^*)$ transition has a maximum at 591 nm and the $^1(\delta^2 \rightarrow \delta^{*2})$ transition has a maximum at 474 nm. The region in the near-infrared (/////) corresponds to the excitation wavelength for the two-photon spectrum.

a.)

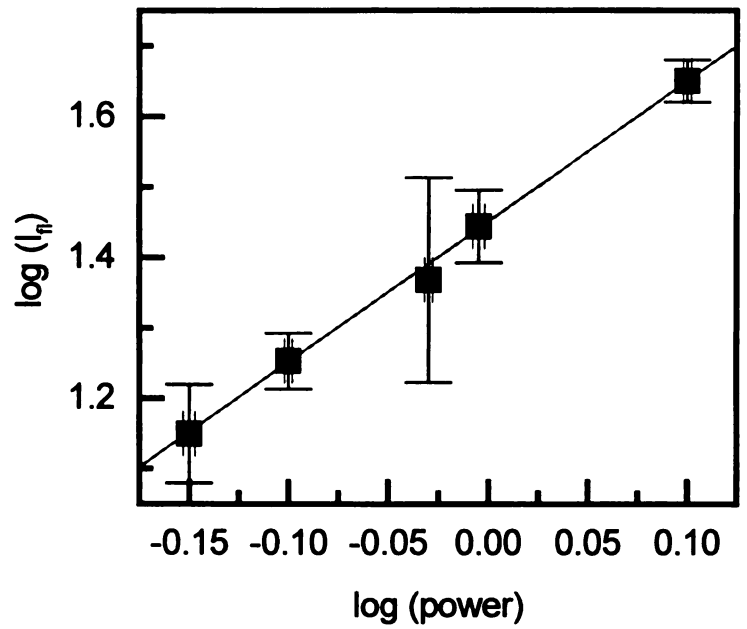

b.)

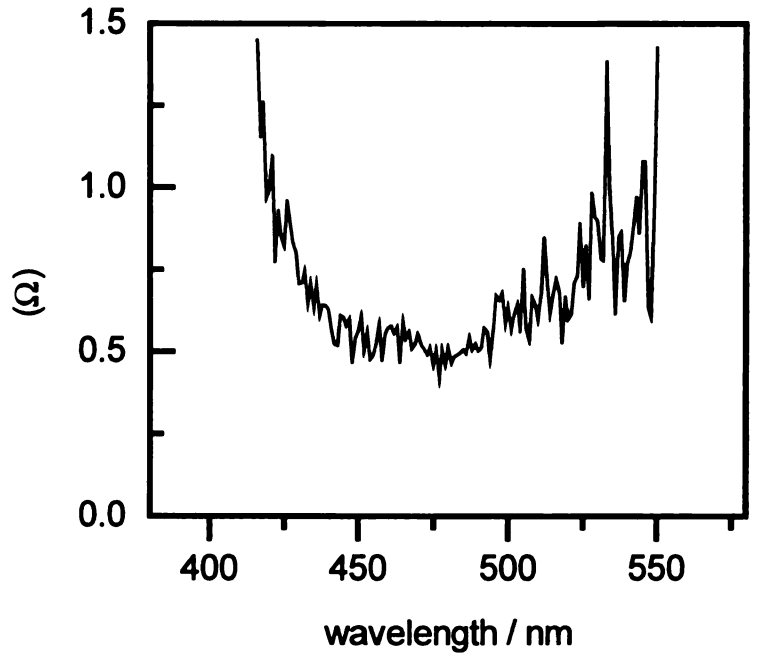

Figure IV.11. Measurements from the two-photon excitation spectra of $Mo_2Cl_4(PEt_3)_4$ in 3-methylpentane. a.) The power dependence when excited with 950 nm vertically polarized light. The line represents a best fit to a slope of 1.99. b.) The polarization ratio is less than one across the $^1(\delta^2 \rightarrow \delta^{*2})$ transition. The rise on the blue edge can be attributed to one-photon excitation of the red edge of the $^1(\delta \rightarrow \delta^*)$ transition. The rise on the red edge is likely due to noise.

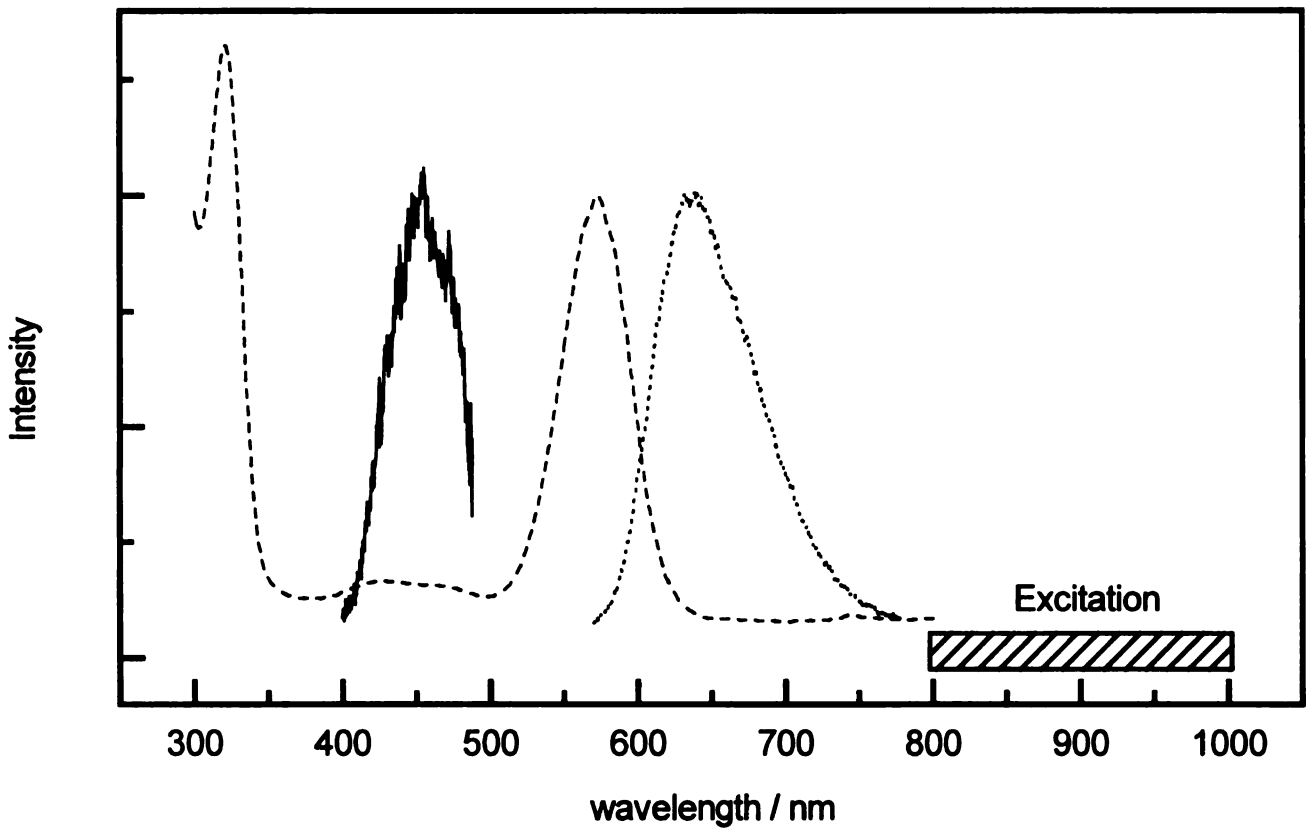

Figure IV.12. The absorption (- - -), fluorescence (···), and two-photon fluorescence excitation (—)spectra of $Mo_2Cl_4(AsMe_3)_4$ in 3-methylpentane. The $^1(\delta \rightarrow \delta^*)$ transition has a maximum at 573 nm, the $^1(\delta^* \rightarrow \delta)$ has a maximum emission at 638 nm and the $^1(\delta^2 \rightarrow \delta^{*2})$ has a maximum at 455 nm. The region in the near infrared (/////) corresponds to the two-photon excitation wavelength.

a.)

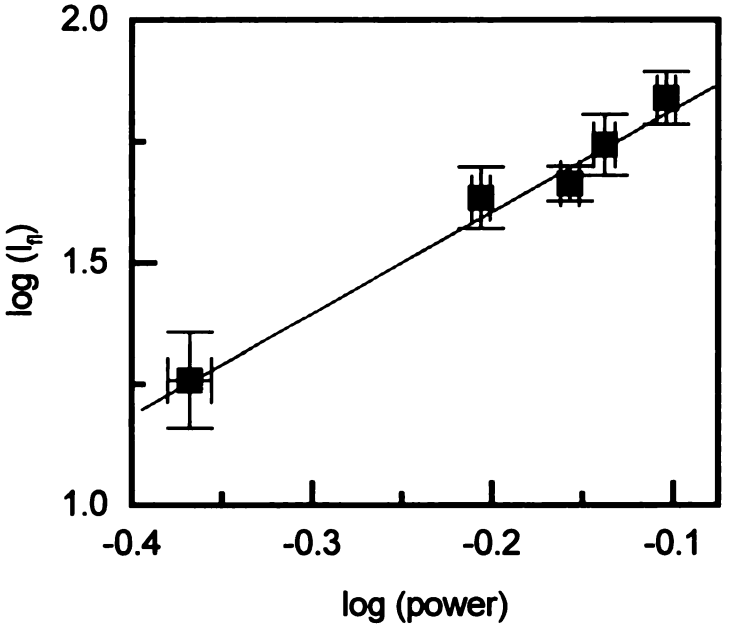

b.)

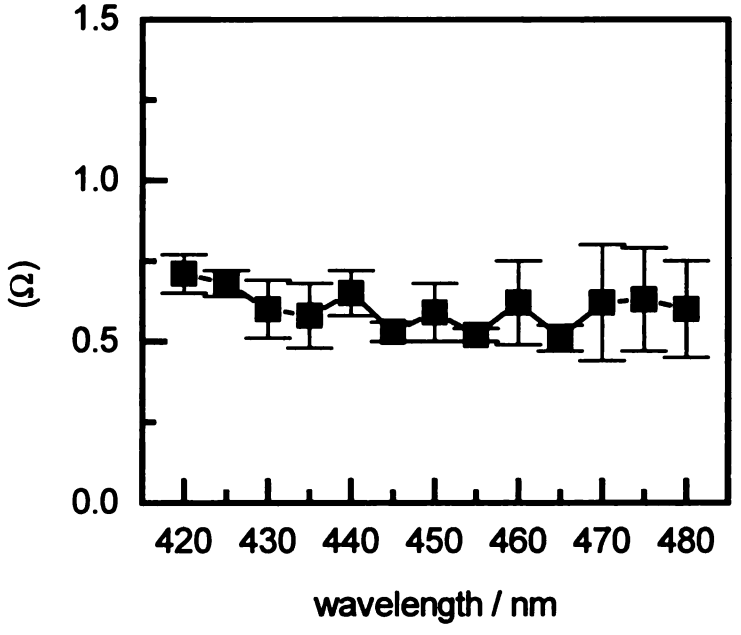

Figure IV.13. Measurements from the two-photon excitation spectra of $Mo_2Cl_4(AsMe_3)_4$ in 3-methylpentane. a.) The power dependence when excited at 910 nm with vertically polarized light. The line represents a best fit to a slope of 2.09. b.) The polarization ratio is less than one across the $^1(\delta^2 \rightarrow \delta^{*2})$ band.polarization ratio is less than 1 across the observed band, again indicating that the initial and final states have the same symmetry.

IV.C.6. $W_2Cl_4(PMe_3)_4$

The absorption and two-photon fluorescence excitation spectra of $W_2Cl_4(PMe_3)_4$ in 3-methylpentane are shown in Figure IV.14. The $^1(\delta \rightarrow \delta^*)$ transition in the absorption spectrum displays a maximum at 660 nm (15150 cm^{-1}) and the $^1(\delta^2 \rightarrow \delta^{*2})$ spectrum has a maximum at 520 nm (19230 cm^{-1}). The power dependence and polarization ratio are displayed in Figure IV.15a and b respectively. The power dependence (collected at 1050 nm with vertical polarization) has a slope of 1.93. The other power dependence measurements had slopes of 1.94 ± 0.08. The polarization ratio is less than one across the $^1(\delta^2 \rightarrow \delta^{*2})$ band, which indicates that the excited state symmetry is the same as the ground state symmetry; it too displays a rise on the blue edge.

IV.C.7. $MoWCl_4(PMe_3)_4$

The absorption and two-photon fluorescence excitation spectra of $MoWCl_4(PMe_3)_4$ in 3-methylpentane are shown in Figure IV.16. The $^1(\delta \rightarrow \delta^*)$ transition exhibits a maximum at 635 nm (15750 cm^{-1}) and the $^1(\delta^2 \rightarrow \delta^{*2})$ transition has its maximum at 481 nm (20790 cm^{-1}). The $^1(\delta^2 \rightarrow \delta^{*2})$ transition does not return to the base-line on the blue edge of the spectrum; rather it rises quickly just to the blue of the maximum. The polarization ratio (Figure IV.17a) also rises quite sharply on the blue edge of the spectrum. This is likely due to the $^1(\delta \rightarrow \delta^*)$ transition being broader (full-width-half-maximum (FWHM) = 74 nm) than that of $Mo_2Cl_4(PMe_3)_4$ (FWHM = 59 nm). Presumably, the FWHM of the $^1(\delta^2 \rightarrow \delta^{*2})$ transition is also broader thus creating a more substantial overlap of the red edge of the $^1(\delta \rightarrow \delta^*)$ transition and the blue edge of the $^1(\delta^2 \rightarrow \delta^{*2})$ transition. The red edge of the polarization ratio also appears to rise; however, owing to the very low fluorescence intensity (5-10 counts/100 laser shots) this is best attributed to noise. The power dependence (950 nm, vertical polarization) shown in Figure IV.17b has a slope of 1.82. The power dependence measurements had a

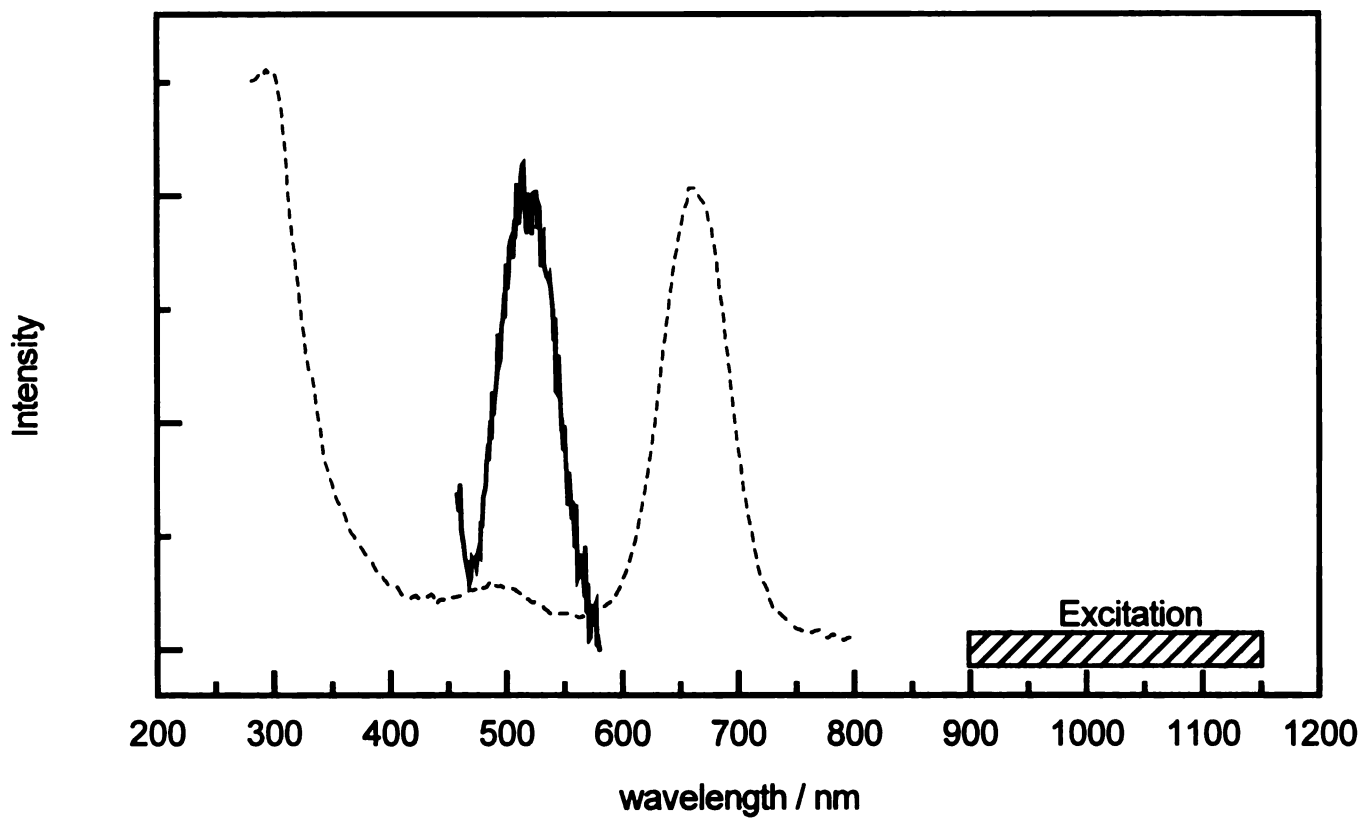

Figure IV.14. The absorption (- - -) and two-photon fluorescence excitation (—) spectra of $W_2Cl_4(PMe_3)_4$ in 3-methylpentane. The $^1(\delta \rightarrow \delta^*)$ transition has a maximum at 660 nm and the $^1(\delta^2 \rightarrow \delta^{*2})$ transition maximizes at 520 nm. The hashed (/////) box in the near infrared corresponds to the two-photon excitation wavelength region.

a.)

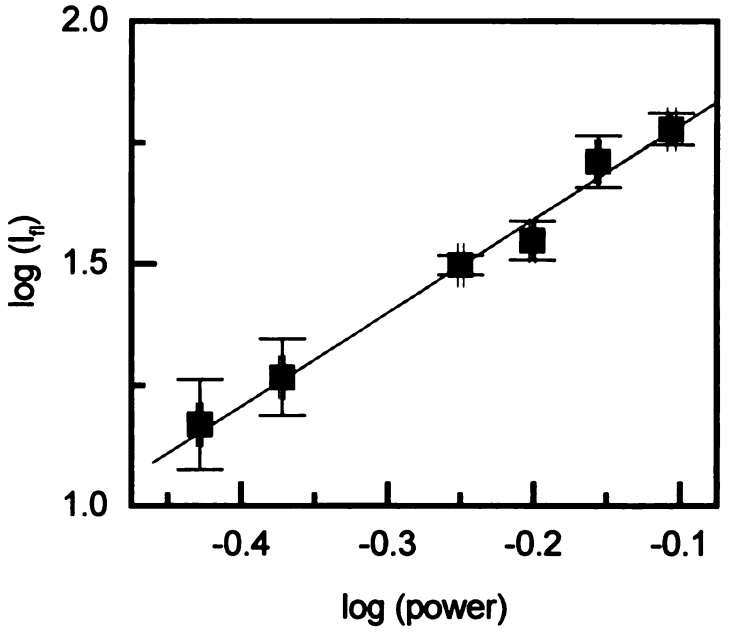

b.)

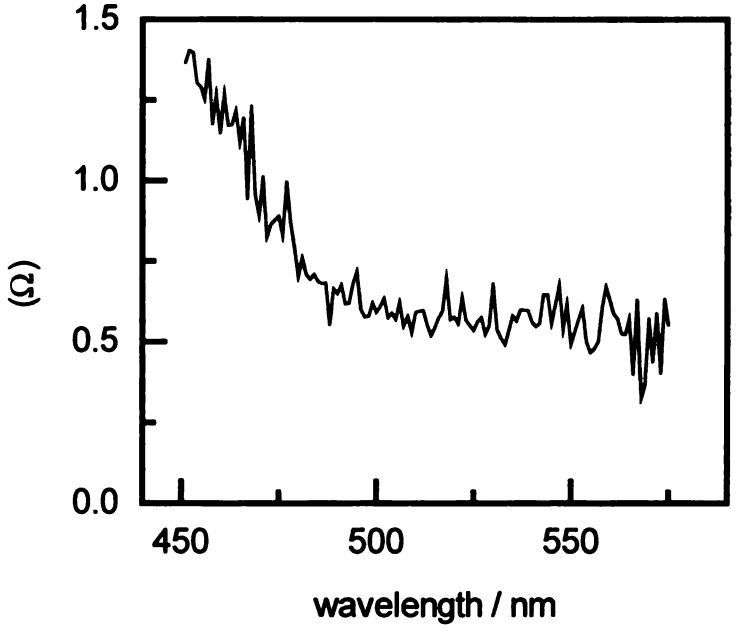

Figure IV.15. Measurements from the two-photon excitation spectra of $W_2Cl_4(PMe_3)_4$ in 3-methylpentane. a.) The power dependence of the fluorescence when excited at 1050 nm. The line represents a best fit with a slope of 1.93. b.) The polarization ratio is less than across the $^1(\delta^2 \rightarrow \delta^{*2})$ transition. The rise on the blue edge can be attributed to excitation of the $^1(\delta \rightarrow \delta^*)$ transition.

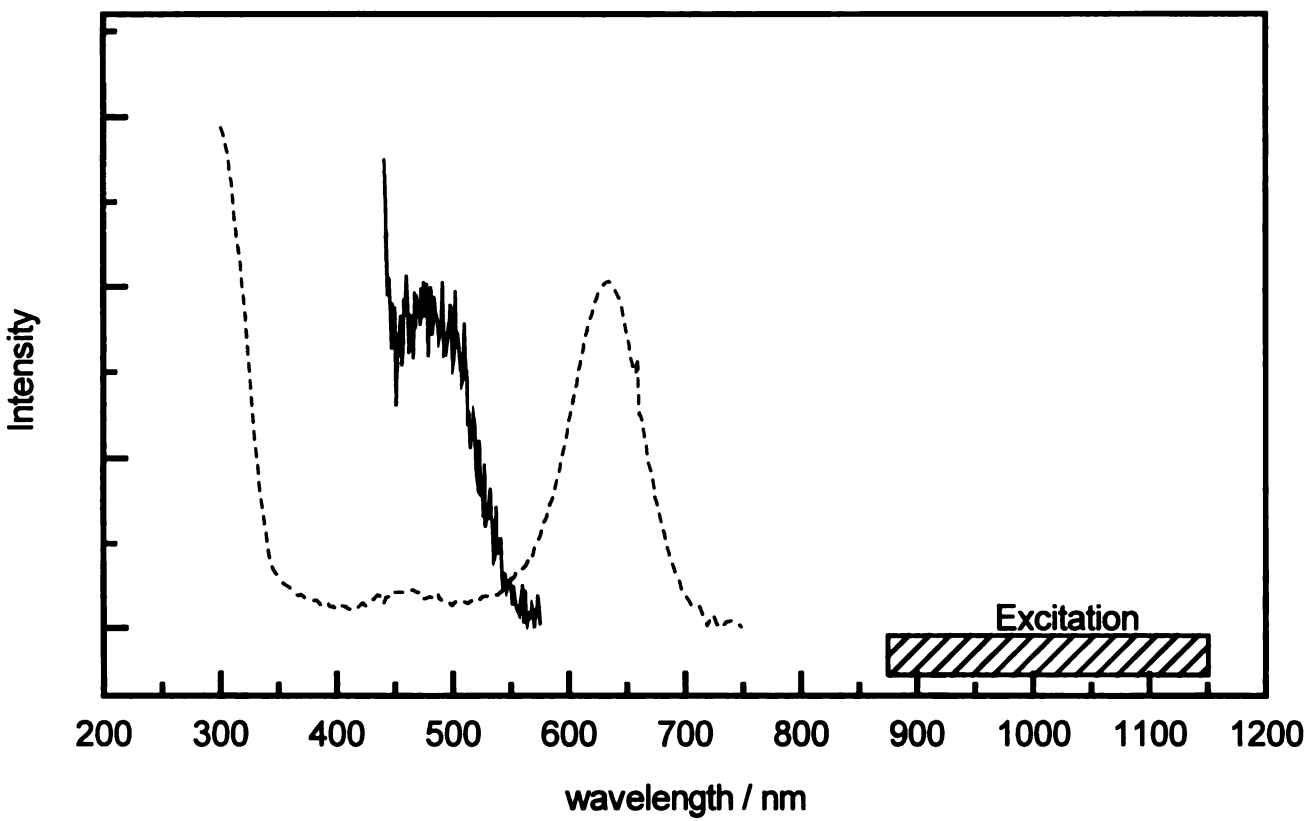

Figure IV.16. The absorption (- - -) and two-photon fluorescence excitation (—) spectra of $MoWCl_4(PMe_3)_4$ in 3-methylpentane. The $^1(\delta \rightarrow \delta^*)$ transition has a maximum at 635 nm and the $^1(\delta^2 \rightarrow \delta^{*2})$ transition maximizes at 481 nm. The hashed (/////) box in the near infrared corresponds to the two-photon excitation wavelength region.

a.)

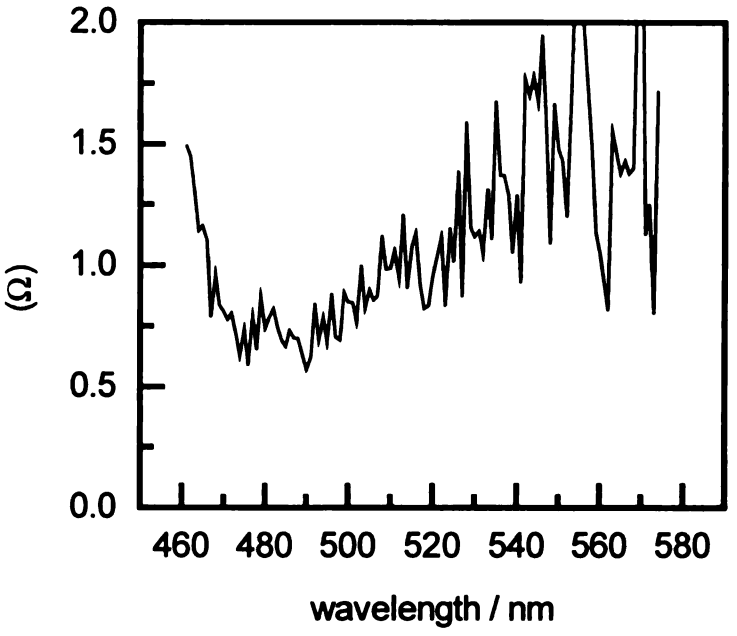

b.)

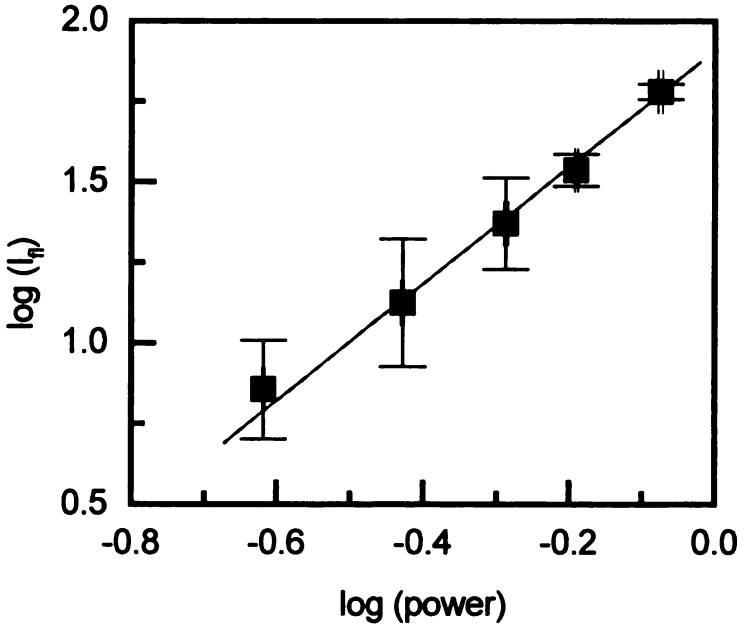

Figure IV.17. Measurements from the two-photon excitation spectra of $MoWCl_4(PMe_3)_4$ in 3-methylpentane. a.) The polarization ratio is less than across the $^1(\delta^2 \rightarrow \delta^{*2})$ transition. The rise on the blue edge can be attributed to excitation of the $^1(\delta \rightarrow \delta^*)$ transition, while the rise on the red edge is due to noise. b.) The power dependence of the fluorescence when excited at 950 nm. The line represents a best fit with a slope of 1.82.

broader distribution (1.85 ± 0.1) than those for the other compounds, due to the generally lower fluorescence intensity observed.

IV.C.8. *cis*-$Mo_2Cl_2(mhp)_2(PMe_2Ph)_2$

The absorption spectrum for this compound is shown in Figure IV.18 and is largely uninformative. Most of the bands observed in the absorption spectrum do not result in a charge transfer to the δ* orbital and therefore do not produce $^1(\delta^* \rightarrow \delta)$ fluorescence. To better see the transitions that do result in a charge transfer to the d* orbital, the one-photon fluorescence excitation spectrum is shown along with the fluorescence spectrum and the two-photon fluorescence excitation spectrum in Figure IV.19. Although *cis*-$Mo_2Cl_2(mhp)_2(PMe_2Ph)_2$ is listed as the last in the series, it was actually the second studied. This compound is the only one to yield a multi-band two-photon spectrum. The $^1(\delta \rightarrow \delta^*)$ transition in the one-photon excitation spectrum has a maximum at 555 nm (18020 cm^{-1}) and the two-photon fluorescence excitation spectrum has two bands with maxima at 390 (25640 cm^{-1}) and 424 nm (23585 cm^{-1}). The valley between the two bands is at approximately 410 nm. The polarization ratio measurements (Figure IV.20a) reveal their utility in the assignment of the low energy band as $^1(\delta^2 \rightarrow \delta^{*2})$. The polarization ratio has a value of approximately one from 360 – 410 nm and falls to less than one for 410 – 460 nm. The power dependence (860 nm, vertical polarization) is shown in Figure IV.20b and has a slope 0f 2.02. The high energy band (390 nm) in the two-photon fluorescence excitation spectrum is difficult to assign due to the low symmetry (C_2) of the molecule. It obviously involves a charge transfer to the δ* orbital since it produces $^1(\delta^* \rightarrow \delta)$ emission, but it is impossible to whether it originates from a ligand based orbital or a metal based orbital.

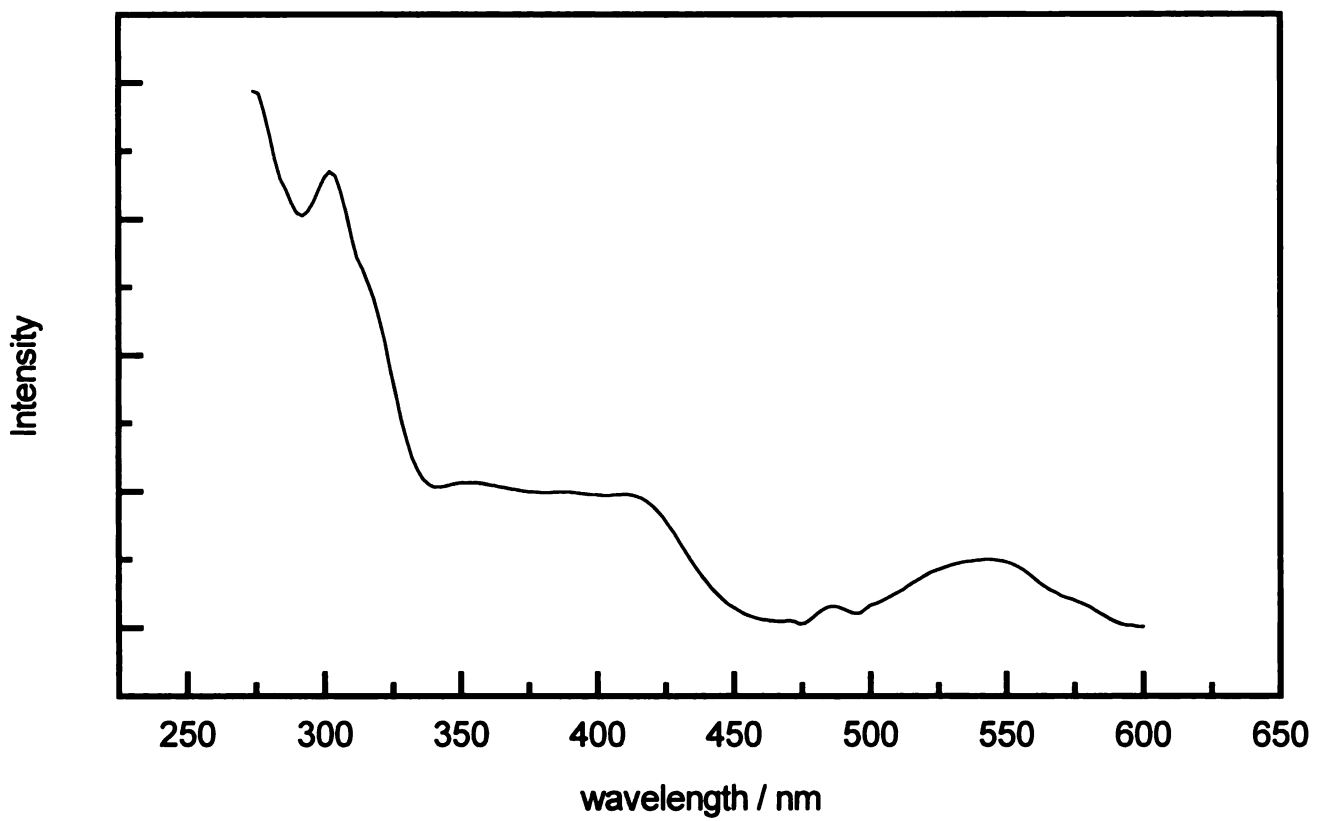

Figure IV.18. The absorption spectrum of *cis*-$Mo_2Cl_2(mhp)_2(PMe_2Ph)_2$ in benzene at room temperature. The spectrum is rather featureless and most of the bands do not result in population of the emissive $^1\delta\delta^*$ state.

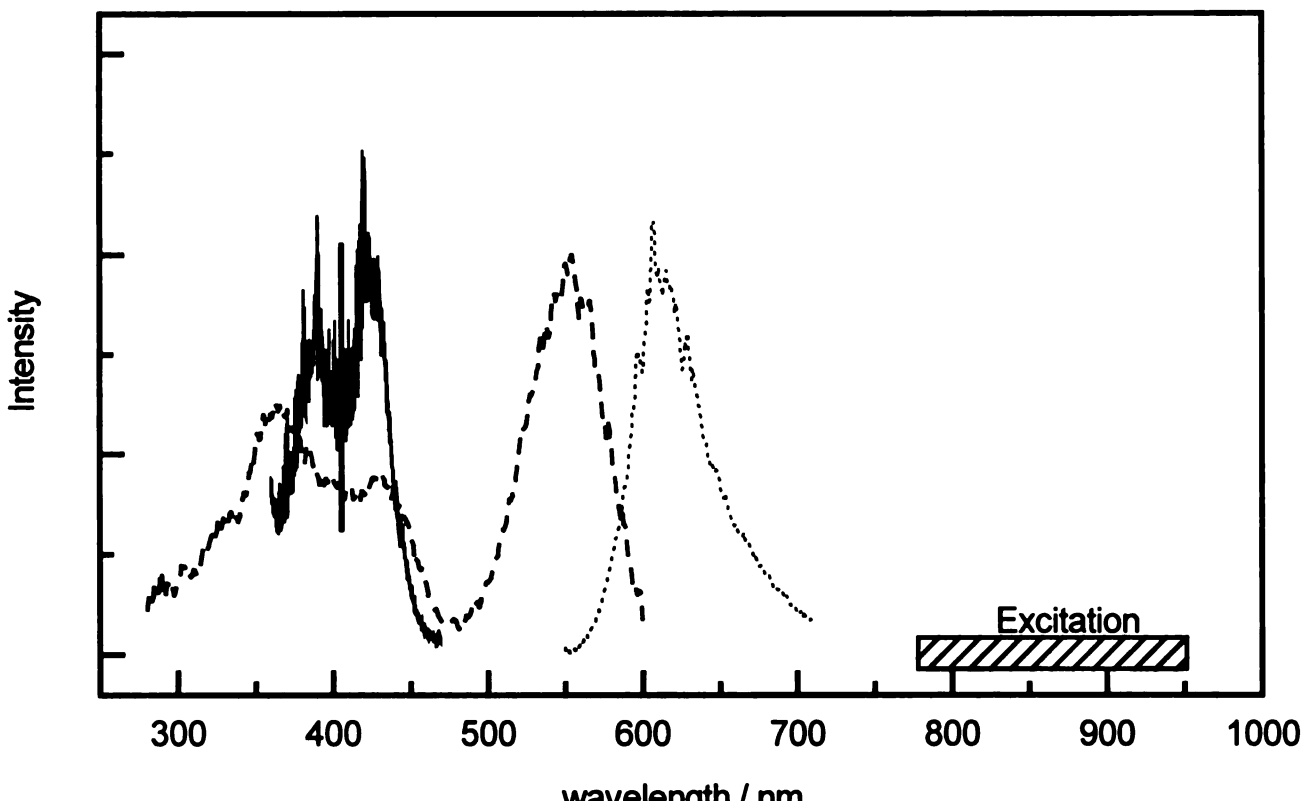

Figure IV.19. The absorption (- - -), fluorescence (···) and two-photon fluorescence excitation (—) spectra of *cis*-$Mo_2Cl_2(mhp)_2(PMe_2Ph)_2$ in benzene. The $^1(\delta \rightarrow \delta^*)$ transition has a maximum at 555 nm, the $^1(\delta^* \rightarrow \delta)$ has a maximum at 615 nm and the two-photon spectrum exhibits two maxima, one at 390 nm and the other at 424 nm. The vertical black line is at 410 nm at represents the valley between the two bands. The hashed box (/////) represents the two-photon excitation region.

a.)

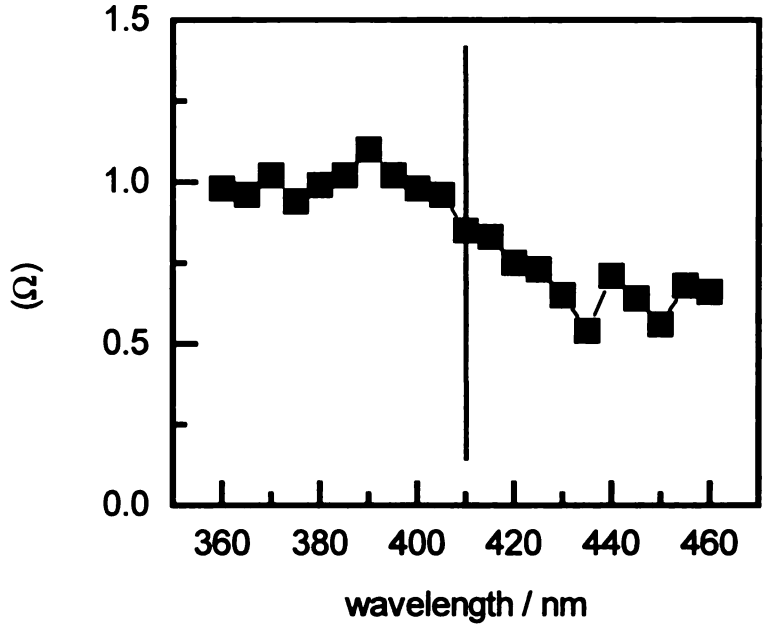

b.)

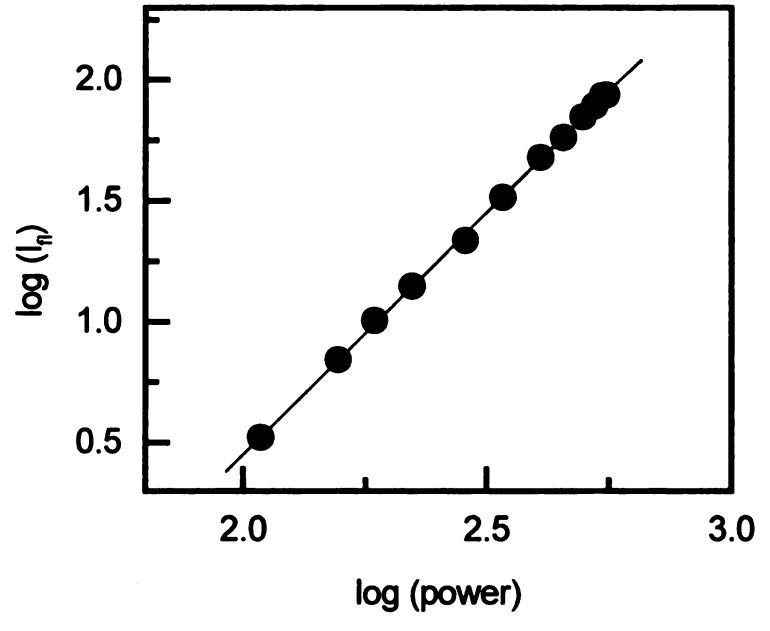

Figure IV.20. Measurements from the two-photon excitation spectra of *cis*-$Mo_2Cl_2(mhp)_2(PMe_2Ph)_2$ in benzene. a.) The polarization ratio has a value of 1 from 360 – 410 nm and falls to be less than one from 410-460 nm. The vertical line is at 410 nm where Ω changes. b.) The power dependence of the fluorescence when excited at 860 nm. The line represents a best fit with a slope of 2.02.

IV.D. Discussion

The data for the $^1(\delta^2 \rightarrow \delta^{*2})$ transition energies, along with the $^1(\delta \rightarrow \delta^*)$ transition energies and the energy gap (ΔE) (as determined from the band maxima) between the $\delta\delta^*$ and δ^{*2} states are collected in Table IV.2. From the values of these two transition energies, the values of the one- (ΔW) and two-electron (K) energies that were defined in Chapter I (and Appendix I) can be determined. The energy of the $^1\delta\delta^*$ state is $K + \sqrt{K^2 + \Delta W^2}$ and the energy of the $^1\delta^{*2}$ state is $2\sqrt{K^2 + \Delta W^2}$. The values calculated for ΔW and K, along with the overlap (S) (as determined from the oscillator strength) of the parent d_{xy} orbitals and metal-metal bond length (where known) are shown in Table IV.3.

IV.D.1. Effect of Halogen Substitution on the δ-manifold.

With respect to the $Mo_2X_4(PMe_3)_4$ series of compounds, the data presented in the preceding tables reveal some startling inconsistencies. The data in Table IV.2 indicate that both the $^1(\delta \rightarrow \delta^*)$ and $^1(\delta^2 \rightarrow \delta^{*2})$ transitions red-shift as the halogen is changed from Cl to Br to I. In the context of the model that was developed in Chapter I, and affirmed by the data in Chapter III, the observed red-shift would correspond to a weakening of the δ-bond by reducing the overlap of the parent d_{xy} orbitals. However, the metal-metal bond length (Table IV.3), remains essentially constant across the entire halogen series. This constant bond length suggests that the d_{xy} orbitals are remaining the same distance apart and therefore maintaining a constant overlap. A second point of consternation arises when the intensity of the $^1(\delta \rightarrow \delta^*)$ transition is considered. The band gets more intense as the halogen is changed from Cl to Br to I. As was shown in Chapter III, as the δ-bond is broken the red-shift observed is coupled with a decreased intensity of the $^1(\delta \rightarrow \delta^*)$ transition.

Table IV.2. Summary of data for the $^1(\delta \rightarrow \delta^*)$ and $^1(\delta^2 \rightarrow \delta^{*2})$ transition energies and the energy gap (ΔE) separating the $\delta\delta^*$ and δ^{*2} states as determined from the band maxima. The energies are in cm^{-1}.

Compound	$^1(\delta \rightarrow \delta^*)$	$^1(\delta^2 \rightarrow \delta^{*2})$	ΔE
$Mo_2Cl_4(PMe_3)_4$	17090	21415	4325
$Mo_2Br_4(PMe_3)_4$	16720	21275	4555
$Mo_2I_4(PMe_3)_4$	15723	19800	4077
$Mo_2Cl_4(AsMe_3)_4$	17450	21980	4530
$Mo_2Cl_4(PEt_3)_4$	16920	21100	4180
$W_2Cl_4(PMe_3)_4$	15150	19230	4080
$MoWCl_4(PMe_3)_4$	15750	20790	5040
cis-$Mo_2Cl_2(mhp)_2(PMe_2Ph)_2$	18020	23585	5565

Table IV.3. The metal-metal bond distance (in Å), overlap (S) of parent d_{xy} orbitals and one- (ΔW) and two-electron (K) energies in cm^{-1}. * S was determined from the oscillator strengths using Mulliken's relationship (Equation I.1), the references are for the oscillator strengths. NM not measured. ** This value is for *cis*-$Mo_2Cl_2(mhp)_2(PEt_3)_2$

Compound	M-M	S[40]*	ΔW	K
$Mo_2Cl_4(PMe_3)_4$	2.130[58]	.16	8597.3	6382.5
$Mo_2Br_4(PMe_3)_4$	2.125[40]	.19	8726.9	6082.5
$Mo_2I_4(PMe_3)_4$	2.129[40]	.22	8006.4	5823
$Mo_2Cl_4(AsMe_3)_4$	NM	.16	8890.9	6460
$Mo_2Cl_4(PEt_3)_4$	2.141[59]		8409.9	6370
$W_2Cl_4(PMe_3)_4$	2.262	.18	7862.1	5535
$MoWCl_4(PMe_3)_4$	2.209[42a]		8909.5	5355
cis-$Mo_2Cl_2(mhp)_2(PMe_2Ph)_2$	2.103[60]**		10014.1	6227.5

The reason for these inconsistencies is the over-simplified nature of the model that has been used. While the model is appealing because of its simplicity, it is applied as if the δ-bond is isolated from the remainder of the molecule, and this is obviously incorrect. As was demonstrated by the calculations reported by Milletti, there is a substantial interaction between the nonbonding halogen p-orbitals and the δ and δ* orbitals.[57] This was further supported by the Mo-X stretches that were observed in the resonance Raman spectra by Gray *et. al.*[40] Furthermore, Cotton demonstrated a strong correlation between the LMCT (Band II) transition and the $^1(\delta \rightarrow \delta^*)$ transition for the $Mo_2X_4(PMe_3)_4$ series of compounds.[43] Also, both Gray[14,40] and Cotton[43] have proposed that the $^1(\delta \rightarrow \delta^*)$ transition steals a great deal of its intensity from Band II. With this wealth of evidence that the halide has a profound effect on the $^1(\delta \rightarrow \delta^*)$ transition it is reasonable to assume a similar halide effect on the $^1(\delta^2 \rightarrow \delta^{*2})$ transition. The red shift that is observed in both transitions is consistent with π-backbonding from the δ* molecular orbital to the nonbonding p orbitals of the halogen. In this scenario, electron density is removed from the d_{xy} orbitals to facilitate the p-backbonding, this in turn weakens the δ-bond. This is manifested as a general reduction in ΔW. The red shift observed in K can also be justified in the context of this picture. Due to the mixing of halogen nonbonding p orbitals into the δ* molecular orbital, the volume of the δ* orbital is increased. This increased volume translates into a reduced K because K is solely dependent on the distance between the electrons ($1/r_{12}$) as shown in Appendix I.

It is interesting to note that while the $^1(\delta \rightarrow \delta^*)$ and $^1(\delta^2 \rightarrow \delta^{*2})$ transitions are red shifting on the order of 1500 cm^{-1} as Cl is replaced by I, the energy gap (ΔE) is only moving ~ 300 cm^{-1}. This is appealing in the context of the model. Recall that it is the energy gap and not the transition energies that determines where on the potential energy curve a molecule lies. Since the energy gap is very similar for this series they all are equally weak bonds. What this implies, in the context of the model, is that perpendicular

to the axis describing the coupling of the orbitals, there is another axis that describes the mixing of halogen character into the δ-manifold.

Some recent work reported by Hopkins demonstrates conclusively that both ΔW and K red shift as the halogen is changed from Cl to Br to I.[61] His experiments involved isolating both the cations (one-electron oxidized) and anions (one-electron reduced) of the parent $Mo_2X_4(PMe_3)_4$ compounds. When an electron is either removed or added to the δ-bond, the two-electron term vanishes. The $^2(\delta \rightarrow \delta^*)$ transition then is a direct measure of the energy that separates the δ and δ* molecular orbitals. Hopkins measured the $^2(\delta \rightarrow \delta^*)$ transition for each of the oxidized and reduced species. The results of these measurements, along with his values calculated for K are recorded in Table IV.4.

Table IV.4. The $^2(\delta \rightarrow \delta^*)$ transition energies for the $Mo_2X_4(PMe_3)_4^{+/-}$ series of compounds. From Reference 61.

$^2(\delta \rightarrow \delta^*)$	$Mo_2Cl_4(PMe_3)_4$	$Mo_2Br_4(PMe_3)_4$	$Mo_2I_4(PMe_3)_4$
Cation (oxidized) (ΔW)	6350	6200	5850
Anion (reduced) (ΔW)	7850	7850	7750
K	6200	6050	5600

The data for the cations displays a definite red shift, whereas the shifts for the anions are not as pronounced. This is likely due to the expansion of the orbitals when an extra electron is placed in them, leading to better overlap. Better orbital overlap is also consistent with the one-electron energies being higher for the anions as compared to the cations. Hopkins' values of ΔW are consistently lower than those determined from this study; however, the δ-bond typically stretches by 0.05 A when an electron is added or removed.[62] This lengthening of the δ-bond would be accompanied by a decrease in overlap of the parent orbitals and therefore a general decrease in the energy.

IV.D.2. Effect of σ-donating ligand on the δ-manifold.

The spectra of $Mo_2Cl_4(PMe_3)_4$ and $Mo_2Cl_4(PEt_3)_4$ are very similar. Both the $^1(\delta \rightarrow \delta^*)$ and $^1(\delta^2 \rightarrow \delta^{*2})$ transitions red shift by ~ 6 nm ($^1(\delta \rightarrow \delta^*)$ 170 cm^{-1}; $^1(\delta^2 \rightarrow \delta^{*2})$ 315 cm^{-1}) when PEt_3 is substituted for PMe_3. Other PR_3 compounds have $^1(\delta \rightarrow \delta^*)$ transitions that can be superimposed with PMe_3. This behavior is largely expected since it is the phosphorous atom that is directly bound to the metal-metal core. Furthermore, the metal-metal bond (Table IV.3) is slightly longer for the PEt_3 derivative which would lead to red shift of the transitions. A blue shift of both transitions by 12 nm ($^1(\delta \rightarrow \delta^*)$ 360 cm^{-1}; ($^1(\delta^2 \rightarrow \delta^{*2})$ 565 cm^{-1}) is observed when $AsMe_3$ is substituted for PMe_3. The crystal structure for $Mo_2Cl_4(AsMe_3)_4$ has not been determined. It is suggested by the similarity of the metal-metal stretching frequencies ($AsMe_3$ = 356 cm^{-1}; PMe_3 = 355 cm^{-1}) that metal-metal bond length is similar. One possible explanation for the observed blue shift is based on a synergism between σ-donating and π-accepting done by the L ligands. The L ligands are bound to the metal through the $d_{x^2-y^2}$ orbital. PMe_3 is a stronger σ-donating ligand than AsMe3; as it pushes electron density into the electron-rich metal-metal core, it also removes electron density through a π-backbonding arrangement with the d_{xy} orbital. This would result in a smaller "effective" overlap of the d_{xy} orbitals and therefore a smaller ΔW as observed. This argument is also supported by data from resonance Raman measurements. Mo-L stretches are observed in the resonance Raman scattering which indicates that there is some mixing of the MoL orbitals with the δ and δ* orbitals. Furthermore, the Mo-As stretch (217 cm^{-1}) is lower in energy than the Mo-P stretch (235 cm^{-1} for X = Cl and Br; 248 cm^{-1} for X = I).[40] $AsMe_3$, which is a better π-acceptor than PMe_3 is not as good a σ-donor. This coupled with the weaker Mo-As bond makes the argument of synergism between σ-donating and π-accepting more valid.

IV.D.3. Effect of Metal Substitution on the δ-manifold.

When W is compared to Mo two important factors must be considered; the size of the d_{xy} orbitals and the metal-metal distance. While W's orbitals are larger than Mo's the metal-metal bond in the resultant quadruply bonded species is also longer. Because the $^1(\delta \rightarrow \delta^*)$ (and the $^1(\delta^2 \rightarrow \delta^{*2})$) transition for $W_2Cl_4(PMe_3)_4$ is red shifted relative to $Mo_2Cl_4(PMe_3)_4$ it is apparent that the increased bond length is not sufficiently compensated by the increased orbital size and a net decrease in the coupling of the d_{xy} orbitals is observed. A weakened W_2 quadruple bond is also manifested in the general reactivity of W_2 and Mo_2 analogs.[63] The red shift observed in ΔW is due to the weaker coupling of the d_{xy} orbitals and the red shift in K can be attributed to the increased volume of W's orbitals relative to Mo's. When the metal-metal core is heterobimetallic (MoW) both $^1(\delta \rightarrow \delta^*)$ and $^1(\delta^2 \rightarrow \delta^{*2})$ transitions are seen to fall in between the Mo_2 and W_2 transitions. The values of ΔW and K for this species appear to be out of line with those observed for Mo and W. This is due to the model used to determine ΔW and K. In the model, the energy of the d_{xy} orbitals is set to zero and ΔW represents the energy difference of the δ and δ* molecular orbitals ($\Delta W = \delta^* - \delta$). For the MoW species the two d_{xy} orbitals are not at the same energy and therefore ΔW (and K) have little meaning for this species.

IV.D.4. *cis*-$Mo_2Cl_2(mhp)_2(PMe_2Ph)_2$

Due to the substantially different ligand set and reduced symmetry of this molecule relative to $Mo_2Cl_4(PMe_3)_4$, perhaps the only meaningful comparison that can be made is between metal-metal distance and ΔW. For *cis*-$Mo_2Cl_2(mhp)_2(PMe_2Ph)_2$ the metal-metal distance is shorter which implies a better overlap of the d_{xy} orbitals as compared to $Mo_2Cl_4(PMe_3)_4$. This is manifested in the blue shift of ΔW.

IV.E. Zwitterionic Character of the $\delta\delta^*$ and δ^{*2} States.

From the values for ΔW and K derived from the transition energies, it is possible to determine the extent of mixing of the δ^2 (pure diradical) and δ^{*2} (pure zwitterionic) states of the δ-manifold (see Figure I.4 in Chapter I). The details of this calculation, performed only on the $M_2X_4(PMe_3)_4$ series of compounds, are presented in Appendix II. The extent of mixing is highly dependent on the overlap (S) of the parent d_{xy} orbitals. The overlap was determined using Mulliken's relationship (Equation I.1) and is related to the intensity of the $^1(\delta \rightarrow \delta^*)$ transition. Because the intensity of the $^1(\delta \rightarrow \delta^*)$ transition is strongly influenced by the halogen the calculation was performed twice. The first calculation represents a very naïve approach, where S was determined from the $^1(\delta \rightarrow \delta^*)$ transition. In the second calculation, S was held constant at the value for $Mo_2Cl_4(PMe_3)_4$ (S = 0.16) for the $Mo_2X_4(PMe_3)_4$ series. The results of both calculations are shown in Table IV.5. The same value of S was used for both calculations performed on $W_2Cl_4(PMe_3)_4$.

Table IV.5. Results of calculation to determine the percentage of zwitterionic character of the excited state.

Compound	%Z (varying S)	%Z (constant S)
$Mo_2Cl_4(PMe_3)_4$	81.33	81.33
$Mo_2Br_4(PMe_3)_4$	80.69	80.09
$Mo_2I_4(PMe_3)_4$	82.43	80.97
$W_2Cl_4(PMe_3)_4$	80.70	80.70

The calculations demonstrate that the δ^{*2} state is very ionic. Since the $^1\delta\delta^*$ and δ^{*2} states are the antisymmetric and symmetric linear combinations of having two-electrons "trapped" on one side of the molecule ($^+M\overset{4}{—}M^-$: ± $:^-M\overset{4}{—}M^+$), $^1\delta\delta^*$ is equally zwitterionic. The same conclusion was drawn from ultrafast-time-resolved-

emission experiments performed by Winkler and co-workers.[64] Using a streak-camera, they were able to monitor the fluorescence of $Mo_2Cl_4(PMe_3)_4$ on the time-scale of solvent motion. When a polar solvent was used, the emission was observed to red shift as the solvent moved to accommodate the newly introduced dipolar excited state. Based on these data, it was calculated that the $^1\delta\delta^*$ excited state possessed a dipole moment of 4.0 Debye.

In terms of the original goal of this dissertation – to locate and characterize a discrete excited state capable of multielectron of multielectron chemistry this research is a resounding success. Moreover, multielectron chemistry has been observed from quadruply bonded dimers by other students that have been involved in this project.

Appendix I

The σ and σ^* molecular orbitals will be defined as the symmetric and antisymmetric linear combination of s type atomic orbitals of hydrogen on nuclei A and B:

$$\sigma = \frac{s(A) + s(B)}{\sqrt{2 + 2S}} \tag{AI.1a}$$

$$\sigma^* = \frac{s(A) - s(B)}{\sqrt{2 - 2S}} \tag{AI.1b}$$

where S is the overlap of the atomic orbitals ($S = \langle s(A) | s(B) \rangle$). The terms in the denominators serve to normalize the wavefunction.

When two electrons (labeled (1) and (2)) are placed in the two orbitals four non-degenerate states may be formed. The lowest energy state is when both electrons occupy the σ orbital (σ^2):

$$\sigma^2 = \sigma(1)\sigma(2) \tag{AI.2a}$$

$$= \frac{1}{2 + 2S}\big(s(A)(1)s(A)(2) + s(A)(1)s(B)(2) + s(B)(1)s(A)(2) + s(B)(1)s(B)(2)\big) \tag{AI.2b}$$

$$= \frac{1}{2 + 2S}\big(A(1)A(2) + A(1)B(2) + B(1)A(2) + B(1)B(2)\big) \tag{AI.2c}$$

$$= \frac{1}{2 + 2S}\big(A(1)A(2) + B(1)B(2)\big) + \frac{1}{2 + 2S}\big(A(1)B(2) + B(1)A(2)\big) \tag{AI.2d}$$

An important point of the linear combination of atomic orbitals is that it neglects the affect of correlated electron motion. This is exemplified in the last equation (AI.2d) where the term on the left describes a purely ionic situation where both electrons are associated with either nuclei A or B. The term on the right has one electron associated with nuclei A and the other with nuclei B and this term can be regarded as being a diradical.

The highest energy state occurs when both electrons occupy the highest energy molecular orbital σ^* (σ^{*2}):

$$\sigma^{*2} = \frac{1}{2-2S}(A(1)A(2) + B(1)B(2)) - \frac{1}{2-2S}(A(1)B(2) + B(1)A(2)) \quad \text{(AI.3)}$$

At intermediate energy there are two states where one electron occupies each of the σ and σ^* molecular orbitals. Following Hund's rule, the triplet state ($^3\sigma\sigma^*$) is the lowest energy of the $\sigma\sigma^*$ states. Since its spin function is symmetric ($\alpha_1\beta_2 + \beta_1\alpha_2$), the spatial component of the wavefunction must be the antisymmetric combination of one electron in each of the σ and σ^* molecular orbitals:

$$^3\sigma\sigma^* = \frac{1}{\sqrt{2}}(\sigma(1)\sigma^*(2) - \sigma^*(1)\sigma(2)) \quad \text{(AI.4a)}$$

$$= \frac{2}{\sqrt{2}}(A(1)B(2) - B(2)A(1)) \quad \text{(AI.4b)}$$

The $^3\sigma\sigma^*$ state is a purely diradical state with one electron on nuclei A and the other on nuclei B. This is the basis of the Pauli Principle that states that two electrons with identical quantum numbers cannot occupy the same region of space.

The $^1\sigma\sigma^*$ is then the symmetric linear combination of having one electron in each of the σ and σ^* orbitals:

$$^1\sigma\sigma^* = \frac{1}{\sqrt{2}}(\sigma(1)\sigma^*(2) + \sigma^*(1)\sigma(2)) \quad \text{(AI.5a)}$$

$$= \frac{2}{\sqrt{2}}(A(1)A(2) - B(1)B(2)) \quad \text{(AI.5b)}$$

The $^1\sigma\sigma^*$ state is a purely ionic state, with both electrons associated with either nuclei A or nuclei B.

The Hamoltinian for the total energy of the system (**H**) consists of a Hamiltonian for each of the electrons ($\mathbf{h}^{(1)}$ and $\mathbf{h}^{(2)}$) and a $1/r_{12}$ operator that describes the interaction (electron correlation) between the two electrons:

$$\mathbf{H} = \mathbf{h}^{(1)} + \mathbf{h}^{(2)} + \frac{1}{\mathbf{r}_{12}} \qquad \text{(AI.6a)}$$

where $\mathbf{h}^{(i)}$ take the form of a typical one electron Hamiltonian:

$$\mathbf{h}^{(i)} = -\left(\frac{\hbar^2}{2m_e}\right)\nabla^2 + V \qquad \text{(AI.6b)}$$

The σ^2 and σ^{*2} states are of the same symmetry ($^1\Sigma_g^+$), and therefore can mix together. The energy of the states is determined by considering the two-dimensional Hamiltonian matrix:

$$H = \begin{pmatrix} \langle \sigma^2 | H | \sigma^2 \rangle & \langle \sigma^2 | H | \sigma^{*2} \rangle \\ \langle \sigma^{*2} | H | \sigma^2 \rangle & \langle \sigma^{*2} | H | \sigma^{*2} \rangle \end{pmatrix} \qquad \text{(AI.7)}$$

The matrix elements on the diagonal represent the energies of the "pure" σ^2 and σ^{*2} states, while the off-diagonal elements determine how much the energy is perturbed by mixing the two states together. This matrix will be called upon in Appendix II to determine the extent of mixing of the states.

Each of the four matrix elements will be determined as follows:

$$\langle \sigma^2 | \mathbf{H} | \sigma^2 \rangle = \langle \sigma^2 | \mathbf{h}^{(1)} | \sigma^2 \rangle + \langle \sigma^2 | \mathbf{h}^{(2)} | \sigma^2 \rangle + \langle \sigma^2 | \frac{1}{\mathbf{r}_{12}} | \sigma^2 \rangle \qquad \text{(AI.8a)}$$

$$= \langle \sigma(1)\sigma(2) | \mathbf{h}^{(1)} | \sigma(2)\sigma(1) \rangle + \langle \sigma(1)\sigma(2) | \mathbf{h}^{(2)} | \sigma(2)\sigma(1) \rangle + \langle \sigma(1)\sigma(2) | \frac{1}{\mathbf{r}_{12}} | \sigma(2)\sigma(1) \rangle \qquad \text{(AI.8b)}$$

where the first term is the energy of electron (1) in the σ molecular orbital, the second term is the energy of electron (2) in σ, and the last term accounts for the Coulomb repulsion of the two electrons in the same orbital. The energy of electrons (1) and (2) will be denoted as $W_1(1)$ and $W_1(2)$ and the Coulomb repulsion will be J_{11}. Using this notation, the energy of the pure σ^2 state is then:

$$\langle \sigma^2 | \mathbf{H} | \sigma^2 \rangle = W_1(1) + W_2(2) + J_{11}(1,2) = 2W_1 + J_{11} \qquad \text{(AI.9)}$$

where the notation has been even further reduced by assuming $W_1(1)$ is equal to $W_1(2)$ and the electron labels have been left off.

The energy of the pure σ^{*2} state is determined in an analogous fashion and the subscripts on W and J refer to the electrons being in the σ^* molecular orbital:

$$\left\langle \sigma^{*2} \middle| \mathbf{H} \middle| \sigma^{*2} \right\rangle = 2W_2 + J_{22} \qquad \text{(AI.10)}$$

The energy of the off-diagonal elements is given by:

$$\left\langle \sigma^2 \middle| \mathbf{H} \middle| \sigma^{*2} \right\rangle = \left\langle \sigma^2 \middle| \mathbf{h}^{(1)} \middle| \sigma^{*2} \right\rangle + \left\langle \sigma^2 \middle| \mathbf{h}^{(2)} \middle| \sigma^{*2} \right\rangle + \left\langle \sigma^2 \middle| \frac{1}{\mathbf{r}_{12}} \middle| \sigma^{*2} \right\rangle \text{(AI.11)}$$

The first two terms are zero, since σ^2 and σ^{*2} are orthogonal, the last term, however is nonzero. This term is similar to the Coulomb repulsion (J_{ii}), but now considers the effect of having two-electrons in the σ (or σ^*) orbital and moving them to the σ (or σ^*) orbital. Since this term involves moving the electrons between the orbitals, it has been named the "exchange" energy. The energy of the states is then given by the secular determinant:

$$E = \begin{vmatrix} 2W_1 + J_{11} - \lambda & K_{12} \\ K_{12} & 2W_2 + J_{22} - \lambda \end{vmatrix} = 0 \qquad \text{(AI.12)}$$

Some substitutions can be made that further simplify the secular determinant. The first is to effectively set the energy of a hydrogen 1s orbital to zero. This is accomplished by setting the average energy of the σ and σ^* molecular orbitals to zero ($\frac{1}{2}\{W_1 + W_2\} = 0$) and defining ΔW as the energy difference between the σ^2 and σ^{*2} molecular orbitals ($\Delta W = W_2 - W_1$). The J_{ii} terms are effectively removed by making the CNDO (complete neglect of differential overlap) approximation. This is justified in Figure A.1. Two extremes of bonding (atomic orbital overlap) are depicted in this figure. In Figure A.1a, the σ molecular orbital is formed by the extensive constructive overlap of hydrogen's 1s orbitals. The electron density is concentrated in the region between the two hydrogen nuclei. The σ^* antibonding orbital is formed by the extensive destructive overlap of the atomic orbitals. The electron density in the σ^* molecular orbital is pushed

a.)

b.)

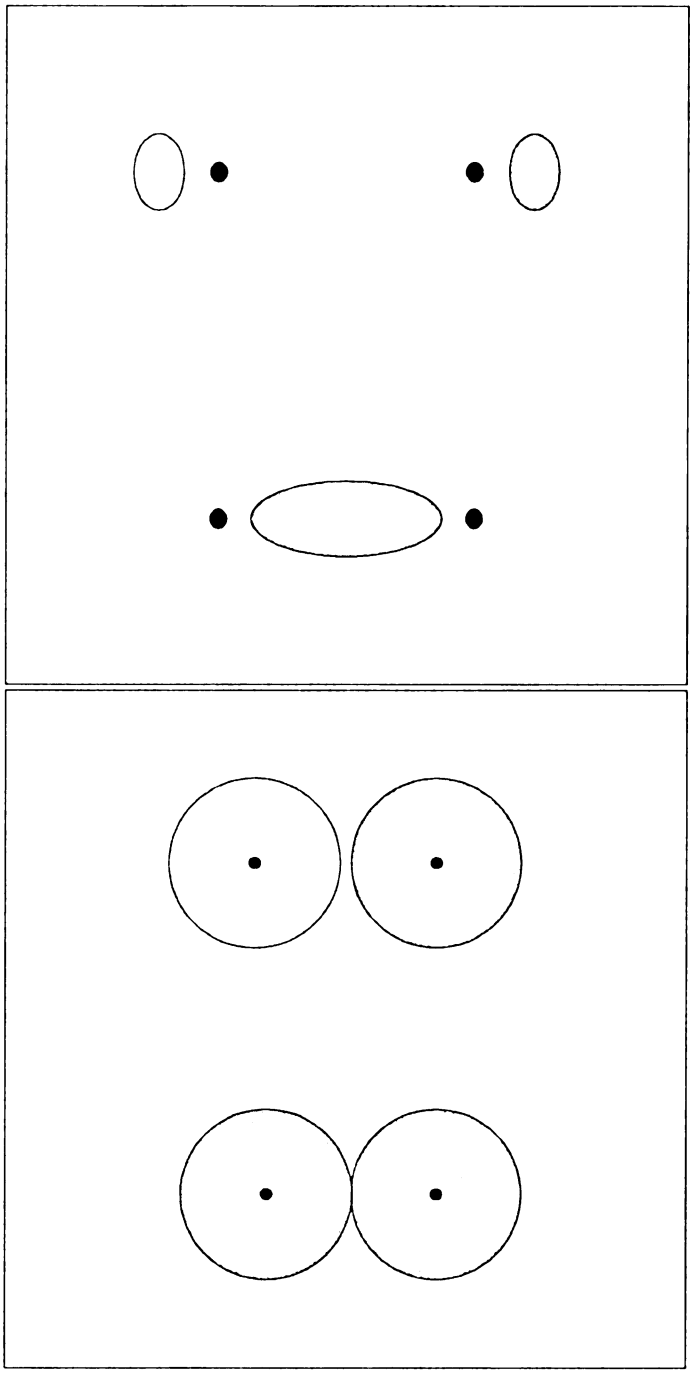

Figure AI.1. Two extremes of orbital overlap in bond formation The nuclei are represented by black dots. a.) The orbitals are overlapped very well and the CNDO approximation is not valid. b.) The orbitals are not overlapped very well and the CNDO approximation is valid.

out to the ends of the molecule. Since the Coulomb energy (J_{ii}) is solely dependent on the distance between the electrons ($1/r_{12}$), it is going to be very different for two electrons in the σ orbital as compared to two electrons in σ^* ($J_{11} \neq J_{22}$). At this extreme of bond formation then, the CNDO approximation is not applicable. However, in the other extreme where the 1s atomic orbitals are only weakly overlapped (Figure A.1b) the CNDO approximation is very valid. The σ molecular orbital is effectively just two hydrogen 1s orbitals barely touching one another and the electron density is concentrated around the nuclei. The σ^* molecular orbital's electron density is also concentrated about the nuclei. Because of this, the Coulomb repulsion energy is very similar when there are two electrons in σ as compared to σ^*. Since the Coulomb repulsions are similar, they can be neglected as a constant offset in energy ($J_{11} = J_{22} = 0$). When these simplifications and assumptions are made, the secular determinant is reduced to:

$$E = \begin{vmatrix} -\Delta W - \lambda & K_{12} \\ K_{12} & \Delta W - \lambda \end{vmatrix} = 0 \qquad \text{(AI.13)}$$

The energy of the $\sigma\sigma^*$ states can be determined in exactly the same fashion; the only new bracket that is encountered is a Coulomb repulsion between the electrons in different orbitals:

$$\left\langle \sigma(1)\sigma^*(2) \left| \frac{1}{r_{12}} \right| \sigma(2)\sigma^*(1) \right\rangle = J_{12}(1,2) \qquad \text{(AI.14)}$$

This Coulomb repulsion can also be ignored based on the CNDO approximation.

The energies of the four electronic states of the hydrogen molecule, when the bond is nearly broken, are then:

$$E_{\sigma^2} = -\sqrt{K_{12}^2 + \Delta W^2} \qquad \text{(AI.15a)}$$

$$E_{^3\sigma\sigma^*} = -K_{12} \qquad \text{(AI.15b)}$$

$$E_{^1\sigma\sigma^*} = +K_{12} \qquad \text{(AI.15c)}$$

$$E_{\sigma^{*2}} = +\sqrt{K_{12}^2 + \Delta W^2} \qquad \text{(AI.15d)}$$

where the energies of the σ^2 and σ^{*2} states were determined by solving the secular determinant (Equation A.13).

Appendix II

The σ^2 and σ^{*2} states are of the same symmetry ($^1\Sigma_g^+$), the two states can mix together:

$$1^1\Sigma_g^+ = c_1\sigma^2 + c_2\sigma^{*2} \qquad \text{(AII.1a)}$$

$$2^1\Sigma_g^+ = c_1\sigma^{*2} + c_2\sigma^2 \qquad \text{(AII.1b)}$$

$1^1\Sigma_g^+$ is the ground state of the molecule and $2^1\Sigma_g^+$ is the highest energy state. The energies and coefficients (which give the extent of mixing) of the states are obtained as the solution to the eigenvalue problem:

$$H\Psi = \varepsilon\Psi \qquad \text{(AII.2a)}$$

$$H = \begin{pmatrix} \langle\sigma^2|H|\sigma^2\rangle & \langle\sigma^2|H|\sigma^{*2}\rangle \\ \langle\sigma^{*2}|H|\sigma^2\rangle & \langle\sigma^{*2}|H|\sigma^{*2}\rangle \end{pmatrix} \qquad \text{(AII.2b)}$$

$$\Psi = \begin{pmatrix} c_1 \\ c_2 \end{pmatrix} \qquad \text{(AII.2c)}$$

The energies of the states were determined in Appendix I and Equation AII.2b is the same as Equation AI.7. The energies, with a more convenient labeling scheme are:

$$E_{\sigma^2} = -\sqrt{K_{12}^2 + \Delta W^2} = \varepsilon_- \qquad \text{(AII.3a)}$$

$$E_{\sigma^{*2}} = +\sqrt{K_{12}^2 + \Delta W^2} = \varepsilon_+ \qquad \text{(AII.3b)}$$

The coefficients are determined from:

$$(H - \varepsilon_\pm)(c) = 0 \qquad \text{(AII.4a)}$$

$$\begin{pmatrix} E_{\sigma^2} - \varepsilon_\pm & K \\ K & E_{\sigma^{*2}} - \varepsilon_\pm \end{pmatrix}\begin{pmatrix} c_1 \\ c_2 \end{pmatrix} = 0 \qquad \text{(AII.4b)}$$

$$(E_{\sigma^2} - \varepsilon_\pm) + K\left(\frac{c_2}{c_1}\right) = 0 \qquad \text{(AII.4c)}$$

$$\frac{c_2}{c_1} = \frac{(\varepsilon_\pm - E_{\sigma^2})}{K} = \lambda_\pm \qquad \text{(AII.4d)}$$

where ε_- and λ_- are associated with the ground state. The coefficient (c_1)of the "pure" σ^2 state is fixed by normalization such that the wavefunction for either state (depending on choice of ε or λ) can be written as:

$$\Psi = \frac{\sigma^2 + \lambda_\pm \sigma^{*2}}{\sqrt{1+\lambda_\pm^2}} \qquad \text{(AII.5a)}$$

$$= \alpha\sigma^2 + \beta\sigma^{*2} \qquad \text{(AII.5b)}$$

where α and β are given by:

$$\alpha = \frac{1}{\sqrt{1+\lambda_\pm^2}}; \beta = \alpha\lambda_\pm \qquad \text{(AII.6)}$$

With these relationships, the wavefunction can be written in terms of pure diradical and pure zwitterionic character (recall that σ^2 and σ^{*2} are both mixtures of diradical and zwitterionic character). This is essentially the transition from a molecular orbital picture to a valence bond picture:

$$\Psi = (A(1)A(2) + B(1)B(2))\left(\frac{\alpha}{2+2S} + \frac{\beta}{2-2S}\right)$$
$$+ (A(1)B(2) + B(1)A(2))\left(\frac{\alpha}{2+2S} - \frac{\beta}{2-2S}\right) \qquad \text{(AII.7)}$$

There are two extremes that must be considered. The first is when the nuclei are far apart, in this extreme, $\lambda = \pm 1$ and $S = 0$. The two wavefunction are then purely diradical (R) and purely zwitterionic (Z):

$$R(1,2) = \frac{A(1)B(2) + B(1)A(2)}{\sqrt{2+2S^2}} : \text{doubly occupied ground state} \qquad \text{(AII.8a)}$$

$$Z(1,2) = \frac{A(1)A(2) + B(1)B(2)}{\sqrt{2+2S^2}} : \text{double occupied excited state} \qquad \text{(AII.8b)}$$

However, as the nuclei come together, the wavefunctions mix together:

$$\langle Z|R\rangle = \frac{\langle A(1)A(2) + B(1)B(2)|A(1)B(2) + B(1)A(2)\rangle}{2+2S^2} = \frac{2S}{1+S^2} \qquad \text{(AII.9)}$$

The last step was performed using Equations AI.1 and AI.3 plus the relationship $S = \langle A | B \rangle$.

Ultimately, the wavefunction for the two states (depending on whether ε_- or ε_+ is chosen) is:

$$\Psi = c_Z Z(1,2) + c_R R(1,2) \qquad \text{(AII.10)}$$

where c_Z and c_R represent the coefficients of the zwitterionic and diradical wavefunctions respectively.

$$\int \Psi^2 dv(1,2) = c_Z^2 Z(1,2)^2 + c_R^2 R(1,2)^2 + 2c_z c_R Z(1,2)R(1,2) \qquad \text{(AII.11)}$$

Since, $\langle Z(1,2) | R(1,2) \rangle \neq 0$, the mixing of the states is not simply the square of the coefficients:

$$c_Z^2 + c_R^2 \neq 1 \qquad \text{(AII.12)}$$

The mixing of the states is instead determined by:

$$c_Z^2 + c_R^2 + 2c_z c_R \langle Z(1,2) | R(1,2) \rangle = 1 \qquad \text{(AII.13)}$$

where the fraction of zwitterionic character is given by:

$$c_Z^2 + c_Z c_R \langle Z(1,2) | R(1,2) \rangle \qquad \text{(AII.14)}$$

where c_Z and c_R, in terms of spectroscopically measured parameters are:

$$c_Z = \sqrt{2 + 2S^2} \left(\frac{\alpha}{2(1-S)} \right) (\eta + \lambda_\pm) \qquad \text{(AII.15a)}$$

$$c_R = \sqrt{2 + 2S^2} \left(\frac{\alpha}{2(1-S)} \right) (\eta - \lambda_\pm) \qquad \text{(AII.15b)}$$

where α is given in Equation AII.6 and $\eta = \frac{1-S}{1+S}$.

REFERENCES

1. Hoganson, C. W., Babcock, G. T., in *Metal Ions in Biological Systems*; Sigel, H., Sigel, A., eds, Dekker: New York, **1994**, *30*, 77-107.

2. Priestley, J., *J. Phil. Trans. Roy. Soc.* (London) **1772**, 62, 147.

3. Heitler, W. London, F., *Z. Phys.*, **1927**,*44*, 455

4. Mulliken, R. S., *Phys. Rev.*, **1934**, *46*, 549. Mulliken, R. S., *Phys. Rev.*, **1936**, *50*, 1017. Mulliken, R. S., *Phys. Rev.*, **1936**, *50*, 1028. Mulliken, R. S., *Phys. Rev.*, **1937**, *51*, 315.

5. Coulson, C. A., Fischer, I., *Philos. Mag.*, **1949**, *40*, 386.

6. See any introductory quantum mechanics text such as Atkins, P.W., *Molecular Quantum Mechanics 2nd Ed.*, **1983**, *Oxford University Press*, New York.

7. Schilling, C. L., Hilinski, E. F., *J. Am. Chem. Soc.*, 1988, 110, 2296. Morais, J., Ma, J., Zimmt, M. B., *J. Phys. Chem.*, **1991**, *95*, 3885. Ma, J. Zimmt, M. B., *J. Am. Chem. Soc.*, **1992**, *114*, 9723.

8. Piotrowiak, P., Strati, G., *J. Am. Chem. Soc.*, **1996**, *118*, 8981-8982

9. Mulliken, R. S., *Phys. Rev.*, **1932**, *41*, 751

10. Ohno, K., *Adv. Quantum Chem.*, **1967**, *3*, 239

11. Salem, L., Rowland, C., *Agnew. Chem. Int. Ed. Engl.*, **1972**,.*11*, 92. Michl, J., *J. Mol. Photochem.*, **1972**, *4*, 243. Michl, J., *J. Mol. Photochem.*, **1972**, *4*, 257. Dauben, W. G., Salem, L., Turro, N. J., *Acc. Chem. Res.*, **1975**, *8*, 41. Borden W. T., *Diradicals*, Wiley: New York, **1982**.

12. Dauben, W. G., Ritscher, *J. Am. Chem. Soc.*,**1970**, *92*, 2925. Marshall, J. A., *Science*, **1970**, *170*, 137. Wulfman, C. E., Kumei, *Science*, **1971**, *172*, 1061. Dauben, W. G., Kellog, M. S., Seeman, J. I., Vietmeyer, N. D., Wendschuh, P. H., *Pure Appl. Chem.*, **1973**, *33*, 197. Tezuka, T. et al, *J. Am. Chem. Soc.*, **1981**, *103*, 1367. Squillacote, M. E., Semple, *J. Am. Chem. Soc.*, **1987**, *109*, 892. Bonačić-Koutecký, V., Michl, *Angew. Chem. Int. Ed. Engl.*, **1987**, *26*, 170.

13. Saltiel, J., *J. Am. Chem. Soc.*, **1968**, *90*, 6394. Author's note: This was the earliest reference located that referred to these states as being "phantom states". There may, however, but even earlier references.

14. Hopkins, M. D., Gray, H. B., Miskowski, V. M., *Polyhedron*, **1987**, *6*, 705-714.

15. Campbell, F. L., Cotton, F. A., Powell, G. L., *Inorg. Chem.*, **1985**, *24*, 177-181.

16. a.) Cotton, F. A., *Science*, **1964**, *145*, 1305. b.) Cotton, F. A., *Inorg. Chem.*, **1965**, *4*, 334.

17. Cowman, C. D., Gray, H. B., *J. Am. Chem. Soc.*, **1973**, *95*, 8177

18. Bratton, W. K., Cotton, F. A., Debeau, M., Walton, R. A., *J. Coord. Chem.*, **1971**, *1*, 121

19. Trogler, W. C., Gray, H. B., *Acc. Chem. Res.*, **1978**, *11*, 232.

20. Mulliken, R. S., *J. Chem. Phys.*, **1939**, *7*, 20

21. Cotton, F. A., Curtis, N. F., Johnson, B. F. G., Robinson, W. R., *Inorg. Chem.*, **1965**, *4*, 326.

22. Benard, M., *J. Am. Chem. Soc.*, **1978**, *100*, 2354.

23. Hay, P. J., *J. Am. Chem. Soc.*, **1982**, *104*, 7007-7017.

24. Get the first reference for χ dependence of δ-manifold

25. Hopkins, M. D., Zietlow, T. C., Miskowski, V. M., Gray, H. B., *J. Am. Chem. Soc.*, **1985**, *107*, 510-512.

26. a.). Cotton, F. A., Eglin, J. L., Hong, B., James, C. A., *J. Am. Chem. Soc.*, **1992**, *114*, 4915-4917. b.). Cotton, F. A., Eglin, J. L., Hong, B., James, C. A., *Inorg. Chem.*, **1993**, *32*, 2104-2106.

27. Higgins, T. V., *Laser Focus World*, **July, 1994**, 91-98.

28. Higgins, T. V., *Laser Focus World*, **January, 1992**, 125-133.

29. See for instance, Atkins, P. W., *Molecular Quantum Mechanics 2nd Ed.*, **1983**, Oxford University Press, New York.

30. Friedrich, D. M. *J. Chem. Ed.*, **1982**, *59*, 472.

31. See for example Fowles, G.R., *Analytical Mechanics, 4th Ed.*, **1986**, *Saunders College Publishing*, New York.

32. This is the time average Poynting vector, see for example, Halliday, D., Resnick, R. *Fundamentals of Physics 3rd Ed.*, **1988**, *John Wiley & Sons*, New York.

33. Levenson, M. D., Dano, S. S., *Introduction to Nonlinear Laser Spectroscopy*, **1988**, *Academic Press Inc.*, New York.

34. McClain, W. M., Harris, R. A., *Two-Photon Molecular Spectroscopy in Liquids and Gases*, in *Excited States*, Lim, E. C., (eds.), **1977**, *Academic Press*, New York.

35. a.). Lin, S. H., Fujimara, Y., Neusser, H. J., Schlag, E. W., *Multiphoton Spectroscopy of Molecules*, **1984**, *Academic Press*, New York. b.). Birge, S. S., in *Ultrasensitive Laser Spectroscopy*, Kliger, D. S. (ed) 1983, *Academic Press*, New York.

36. a.). Monson, P. R., McClain, W. M., *J. Chem. Phys.*, **1970**, *53*, 29. B.) McClain, W. M., *J. Chem. Phys.*, **1971**, *55*, 2789.

37. Drago, R. S., *Physical Methods for Chemists, 2nd Ed.*, **1992**, *Saunders College Publishing*, New York.

38. Nasciemento, M. A. C., *Chem. Phys.*, **1983**, *74*, 51.

39. Cotton, F. A., Extine, M. W., Felthouse, T. R., Kolthammer, B. W., Lay, D. G., *J. Am. Chem. Soc.*, **1981**, *103*, 4040.

40. Hopkins, M. D., Schaefer, W. P., Bronikowski, M. J., Woodruff, W. H., Miskowski, V. M., Dallinger, R. F., Gray, H. B., *J. Am. Chem. Soc.*, 1987, 109, 408-416.

41. Schrock, R. R., Sturgeoff, L. G., Sharp, P. R., *Inorg. Chem.*, **1983**, *22*, 2801-2806.

42. a.). Luck, r. L., Morris, R. H., Sawyer, J. F., *Inorg. Chem.*, **1987**, *26*, 2422. b.). Morris, R. H., *Polyhedron*, **1987**, *6*, 793.

43. Cotton, F. A., Wiesinger, K. J., *Inorg. Chem.*, **1992**, *31*, 920-925.

44. Harwood, W. S., Kennedy, S. M., Lytle, F. E., Qi, J., Walton, R. A., *Inorg. Chem.*, **1987**, *26*, 1784-1788.

45. Cotton, F. A., Falvello, L. R., Harwood, W. S., Powell, G. L., Walton, R. A., *Inorg. Chem.*, **1986**, *25*, 3949-3953.

46. Brencic, J. V., Cotton, F. A., *Inorg. Chem.*, **1972**, *13*, 87-89.

47. Agaskar, P. A., Cotton, F. A., Fraser, I. F., Manojlovic-Muir, L, Muir, K. A., Peacock, R. D. *Inorg. Chem.*, **1986**, *25*, 2511-2519.

48. Campbell, F. L. III, Cotton, F. A., Powell, G. L., *Inorg. Chem.*, 1985, 24, 4384-4389.

49. Agaskar, P. A., Cotton, F. A., *Inorg. Chem.*, **1984**, *23*, 3383-3387.

50. Yu, J. Ph. D. Dissertation, Michigan State University, **1990.**

51. Saari, E. PhD. Dissertation, Michigan State University, **1998**.

52. Engebretson, D. S., Zaleski, J. M., Leroi, G. E., Nocera, D. G., *Science*, **1994**, *265*, 759-762.

53. Operator's Manual for Coherent Type I XPO

54. a.). Hopkins, M. D., Gray, H. B., *J. Am. Chem. Soc.*, **1984**, *106*, 2468-2469. b.). Hopkins, M. D., Miskowski, V. M., Gray, H. B., *J. Am. Chem. Soc.*, **1988**, *110*, 1787-1793. c.). Miskowski, V. M., Gray, H. B., Hopkins, M. D., *Inorg. Chem.*, **1992**, *31*, 2085-2091.

55. Cotton, F. A., Hubbard, J. L., Lichtenberger, D. L., Shim, I. *J. Am. Chem. Soc.*, **1982**, *104*, 679.

56. Cotton, F. A., Feng, X., *J. Am. Chem. Soc.*, **1993**, *115*, 1074.

57. Milletti, M. C. *Polyhedron*, **1993**, *12*, 401-405.

58. Cotton, F. A., Extine, M. W., Felthouse, T. R., Kolthammer, B. W. S., Lay, D. G., *J. Am. Chem. Soc.*, **1981**, *103*, 4040-4045.

59. Cotton, F. A., Daniels, L. M., Powell, G. L., Kahaian, T. J., Smith, Vogel, E. F., *Inorg. Chim. Acta*, **1988**, *144*, 109.

60. Fanwick, P. E., *Inorg. Chem.*, **1985**, *24*, 256-263.

61. Hopkins, M. D., data reported at the ACS meeting in Dallas TX, April, **1998**. The data and trends were confirmed *via* a personal communication.

62. Bino, A, Cotton, F. A., *Angew. Chem. Int. Ed. Engl.*, **1979**, *18*, 462.

63. Cotton, F. A., Walton, R. A., *Multiple Bonds Between Metal Atoms 2nd Ed.*, **1993**, Clarendon Press, Oxford

64. Zhang, X., Kozik, M., Sutin, N., Winkler, J. R., *in Electron Transfer in Inorganic, Organic, and Biological Systems*, Bolton, J. R., Matage, N., McLendon, G. Eds., *American Chemical Society Advances in Chemistry Series no. 228*, Washington D. C., **1991**, pp. 247-264.